Dissertation
submitted to the
Combined Faculties of the Natural Sciences and Mathematics
of the Ruperto-Carola-University of Heidelberg, Germany
for the degree of
Doctor of Natural Sciences

Put forward by
Claudia Mignone
born in: Salerno, Italy
Oral examination: 20th May, 2009

Model-Independent Reconstruction of the Expansion Rate of the Universe Through Combination of Different Cosmological Probes

Referees:	Prof. Dr. Matthias Bartelmann
	Prof. Dr. Lauro Moscardini

Zusammenfassung

In der vorliegenden Arbeit wird ein Verfahren vorgestellt, die kosmische Expansionsrate und den linearen Wachstumsfaktor, der die kosmische Strukturbildung beschreibt, aus verschiedenen kosmologischen Messungen ohne Bezug auf ein besonderes Friedmann-Modell und seine Parameter einzuschränken. Zuerst wurde eine modellunabhängige Rekonstruktionstechnik entwickelt, um die Expansionsrate aus Daten für die Leuchtkraftdistanz abzuschätzen: Sie konvertiert die Integralbeziehung zwischen der Expansionsfunktion und der Leuchtkraftdistanz in eine Volterra-Integralgleichung, welche bekanntermaßen eine eindeutige Lösung besitzt, die als Neumann-Reihe beschrieben werden kann. Indem Observable, wie die Leuchtkraftdistanzen zu Supernovae vom Typ Ia, in eine Reihe orthonormaler Funktionen entwickelt werden, kann die Integralgleichung gelöst und die kosmische Expansionsrate innerhalb der Fehlergrenzen der Daten bestimmt werden. Die Leistungsfähigkeit des Verfahrens wird durch Anwendung auf synthetische Daten mit steigender Komplexität demonstriert, die ein künstliches Modell mit einem plötzlichen Sprung in der Expansionsrate beinhalten. Unter der zusätzlichen Annahme von lokaler Newton'scher Dynamik kann die Wachstumsrate der kosmischen Strukturbildung aus der Abschätzung der Expansionsrate auf einem Rotverschiebungsintervall, in dem Supernovae zugänglich sind, berechnet und für die Analyse von Daten der kosmischen Scherung benutzt werden. Kombiniert mit einer traditionellen Analyse desselben Datensatzes, die auf dem ΛCDM-Modell basiert, erlaubt dieser Ansatz, die Bedingungen an den Parameter $\Omega_{\rm m}$, der die kosmische Materiedichte beschreibt, und an σ_8, der die Normalisierung des Leistungsspektrums parametrisiert, zu stärken. Außerdem kann das Verfahren zur Rekonstruktion der Expansionsrate aus Daten der Winkeldurchmesserdistanz von Messungen der Wellenlänge baryonischer akustischer Oszillationen angewendet werden. Eine Optimierung des Satzes orthonormaler Funktionen, die im Algorithmus zum Einsatz kommen, wurde mittels einer Hauptkomponentenanalyse durchgeführt.

Abstract

This work proposes a method to constrain the cosmic expansion rate and the linear growth factor for structure formation from different cosmological measurements, without reference to a specific Friedmann model and its parameters. First, a model-independent reconstruction technique to estimate the expansion rate from luminosity distance data has been developed: it converts the integral relation between the expansion function and the luminosity distance into a Volterra integral equation, which is known to have a unique solution in terms of a Neumann series. Expanding observables such as the luminosity distances to type-Ia supernovae into a series of orthonormal functions, the integral equation can be solved and the cosmic expansion rate recovered within the limits allowed by the accuracy of the data. The performance of the method is demonstrated through application to synthetic data sets of increasing complexity, including a toy model with a sudden transition in the expansion rate. With the additional assumption of local Newtonian dynamics, the growth rate for linear structure formation can be calculated from the estimate of the expansion rate, in the redshift interval over which supernovae are available, and employed in the analysis of cosmic shear data: combined to a traditional, ΛCDM analysis of the same data set, this approach allows to tighten the constraints on the matter density parameter, $\Omega_{\rm m}$, and the normalisation of the power spectrum, σ_8. Furthermore, the method to reconstruct the expansion rate can be applied to angular-diameter distance data from baryon acoustic oscillation experiments; an optimisation of the orthonormal function set employed in the algorithm has also been performed, by means of a principal component analysis.

“Don’t take gravity too lightly or it’ll catch up with you ...”

Contents

Introduction

The past decade witnessed an authentic revolution in the field of observational cosmology, with the collection and analysis of huge amounts of data, probing with unprecedented precision the spatial distribution and time evolution of several different astronomical objects, based on completely different physical mechanisms. The outcome of this amazing experimental effort resulted in a completely new awareness of the constituents and the dynamics of the universe.

The first hint of evidence that the cosmic expansion has recently entered a phase of acceleration was provided by measurements of the distance-redshift relation from type-Ia supernovae (Riess et al., 1998; Perlmutter et al., 1999), and possibly explained invoking the existence of a cosmological constant, i.e. a component with negative pressure, thus able to drive such an accelerated expansion. After this first claim, results from a plethora of different observations followed: outstanding measurements of temperature anisotropies in the cosmic microwave background (Spergel et al., 2003, 2007; Komatsu et al., 2009) and of the large-scale matter power spectrum from galaxy redshift surveys (Cole et al., 2005; Percival et al., 2007b), along with observations of the evolution of galaxy clusters (Allen et al., 2003, 2004), the detection of the baryonic acoustic feature in the galaxy distribution (Eisenstein et al., 2005; Percival et al., 2007a) and of the cosmic shear signal due to the gravitational lensing effect of the large scale structure on the background galaxy population (Hoekstra et al., 2006; Semboloni et al., 2006; Fu et al., 2008), all point towards what is currently referred to as the “concordance” model for cosmology.

Based on this impressive amount of observational information, the universe is described as composed by only a tiny amount of baryonic matter: a quarter of it is made up by a non-electromagnetically interacting component, the so-called dark matter, and to account for the remaining three quarters one has to resort to Einstein's cosmological constant, or to even more exotic explanations (quintessence and modified gravity, just to name a few) which go under the name of dark energy.

The challenge for the next decade is to investigate the very nature of this dark energy: several ambitious surveys are currently being realised and planned, including space-based projects, with the goal of understanding whether the dark energy is truly a cosmological constant or evolves in time, whether an exotic explanation is required to describe its dynamics and, if that is the case, which theoretical model would better suit the observations. The possible scenarios from a theoretical point of view are many, but it is still possible to say only very little to discern amongst them. Even with the high accuracy promised by future data sets, the possibility of introducing theoretical prejudice in the data analysis, thus obtaining biased results, is not at all ruled out (Maor et al., 2001; Bassett et al., 2004).

In this rather obscure context, model-independent techniques to analyse the data without assuming a particular model for the dark energy stand out as a fundamental approach to reconstruct the cosmic functions underlying the measurements without being driven by a bias coming from theory (see, e.g. Starobinsky 1998; Huterer & Turner 1999, 2000; Tegmark 2002; Wang & Tegmark 2005; Huterer & Starkman 2003; Simpson & Bridle 2006).

The two fundamental functions in cosmology are the cosmic expansion rate and the growth factor for linear density perturbations: any measurement involving distances or the distribution of matter on large scale carries information about them. The information is clearly encoded in the measurements in different ways, depending on the specific physical properties of the objects under consideration: the fact that, however, the underlying functions are the same, suggests the possibility of developing a common formalism in order to estimate them from different observational probes.

The work developed in this thesis has exactly this purpose: to parameterise the contribution of the expansion rate and the growth factor to different cosmological measurements, namely type-Ia supernovae, cosmic shear and baryon acoustic oscillations, and to reconstruct them in a model-independent way.

The central object of this work is a reconstruction technique, which provides an estimate of the cosmic expansion rate from luminosity-distance data, without any reference to Friedmann models. The only two assumptions the method relies on are the following: the universe is on average homogeneous, isotropic and topologically simply connected, and the expansion rate is reasonably smooth. The core of the method is the transformation of the integral relation between the expansion function and the luminosity distance into a Volterra integral equation of the second kind, whose solutions are known to exist and can be uniquely described in terms of a convergent Neumann series. This guarantees that the method returns *the* unique expansion rate of the universe within the accuracy limits allowed by the data. In order to be solved, the integral equation must be fed with the derivative of the data: hence, the data need to be appropriately smoothed, and this is achieved via expansion into a basis of orthonormal functions. The basis is in principle arbitrary, but it can be optimised in order to concentrate all the relevant information in a very small number of parameters (Mignone & Bartelmann, 2008).

Additionally, in the assumption of local Newtonian dynamics, the linear growth factor of density perturbation can be obtained as a solution of a second-order differential equation which essentially depends on the expansion rate and its first derivative. Empirical knowledge of the expansion rate, even based on data available in a finite redshift interval, can be thus translated into an estimate of the growth factor, valid only in the aforementioned redshift interval but independent of any parameterisation of the energy content in the universe. Hence, the method developed in this work represents a tool to extract information from purely geometric tests, such as those probing the distance-redshift relation, and to insert into the analysis of other cosmological probes, involving the large-scale distribution of matter in the universe, thus the growth of structure.

The work is organised as follows: in Chapter 1 the main features of the standard cosmological model are summarised, with particular emphasis on the two functions mentioned above, namely the cosmic expansion rate and the linear growth factor of density perturbations; Chapter 2 contains a review of the main observational tests, which represent evidence in favour of the so-called “concordance” model, namely type-Ia supernovae, baryonic acoustic oscillations, big-bang nucleosynthesis, cosmic microwave background and cosmic shear. Chapter 3 presents the framework from which this work originates: along with the main theoretical explanations to the observed accelerated trend of cosmic expansion, the current and future efforts exerted by the observational community are described. In this context, the need for a model-independent approach to cosmological data sets is highlighted.

The model-independent technique to reconstruct the cosmic expansion rate from luminosity-distance data is detailed and demonstrated with several examples in Chapter 4: applications to synthetic and real samples of supernovae of type-Ia are shown, along with its capability to recover sudden irregularities in the expansion function. The application of this empirical estimate of the expansion rate to evaluate the linear growth factor is discussed in Chapter 5: a method to analyse cosmic shear data employing both these reconstructed quantities in order to constrain the matter density parameter and the normalisation of the power spectrum is also presented. Chapter 6 contains two possible extensions of the model-independent reconstruction technique: first, an application to angular-diameter distances estimated from baryon acoustic oscillation data is illustrated; then, an optimisation of the orthonormal function set employed in the reconstruction, by means of a principal component analysis, is discussed. Finally, the conclusions of this work are outlined in Chapter 7.

Chapter 1

Unfolding the Universe: the Expansion Rate and the Growth of Structure

In this chapter, the theoretical background for what is currently acknowledged as the standard cosmological model is presented, with particular emphasis on two fundamental functions, namely the cosmic expansion rate and the growth rate of cosmic structures. These two functions are extremely important, being the mathematical objects underlying all cosmological measurements, thus they influence any constraint that can be inferred from observations. Some reference textbooks have been used throughout the first two chapters, namely Coles & Lucchin (2002), Dodelson (2003), Weinberg (2008), as well as some review papers (Bartelmann, 2009; Carroll, 1997).

1.1 The Robertson-Walker Metric

Cosmology studies the evolution of the universe on very large scales, and on these scales the universe is governed solely by gravity. In the framework of general relativity, the best current theory for gravity, the space-time is characterised as a four-dimensional manifold, with a metric, $g_{\mu\nu}$, which is a dynamical field, i.e. space-time dependent. The dynamics of the metric is governed by Einstein's field equations, which connect the metric to the energy and matter in the universe.

In order to fully specify the metric, two fundamental assumptions are usually made, which are justified on observational grounds: (1) when averaged over sufficiently large scales, the spatial properties of the universe are isotropic, i.e. no preferred direction exists; (2) our position in the universe is by no means preferred to any other, also known as Cosmological Principle. Because of the latter assumption, the first one must hold for any point in the universe, hence the universe is also homogeneous.

The metric tensor $g_{\mu\nu}$ is symmetric, thus only 10 of its 16 components are independent. The assumption that space is isotropic and homogeneous is clearly not true in the locally observed universe, but holds on large scales, and helps simplifying the specification of the metric: it allows, in fact, to find a preferred class of observers, to whom the universe appears isotropic. Isotropy requires that only its time-time and space-space components are non-zero, i.e. $g_{0i} = g_{i0} = 0$, otherwise a particular direction in space could be identifies, related to the three vector v_α with components $g_{0\alpha}$; furthermore, clock synchronisation arguments for these fundamental observers imply $g_{00} = c^2$. The invariant line element ds is reduced to

$$\mathrm{d}s^2 = c^2\mathrm{d}t^2 + g_{ij}\mathrm{d}x^i\mathrm{d}x^j \ , \tag{1.1}$$

which allows a particular foliation of the four-dimensional space-time into spatial hyper-surfaces which are homogeneous and isotropic at a given time. The spatial hyper-surfaces can be scaled by a function, $a(t)$, which depends on time only because of homogeneity, and they have to be spherically symmetric because of isotropy. Having defined polar coordinates (χ, θ, ϕ), where χ is the radial coordinate and (θ, ϕ) are the polar angles, the line element can be written in its most general form as

$$\mathrm{d}s^2 = c^2\mathrm{d}t^2 - a^2(t)\left[\mathrm{d}\chi^2 + f_K^2(\chi)\left(\mathrm{d}\phi^2 + \sin^2\theta\mathrm{d}\phi\right)\right] \ ; \tag{1.2}$$

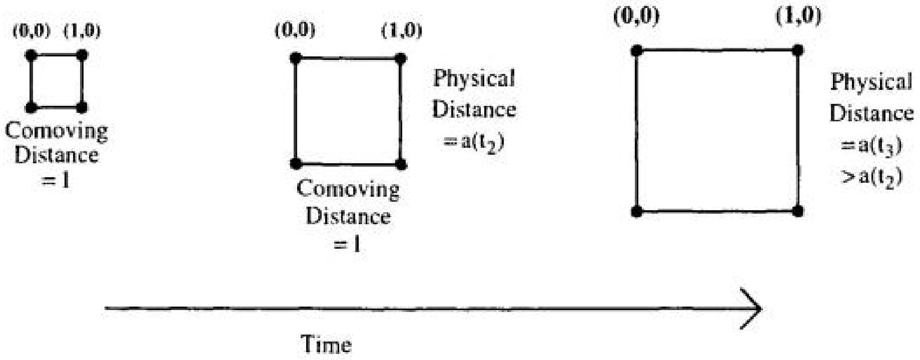

Figure 1.1: The expansion of the universe: the comoving distance between points on the grid stays constant as expansion proceeds, whereas the physical distance is proportional to the comiving distance times the scale factor, thus increasing as time evolves. From Dodelson (2003).

because of homogeneity, the function $f_K(\chi)$ must be of the form

$$f_K(\chi) = \begin{cases} \sin\chi & (K=1) \\ \chi & (K=0) \\ \sinh\chi & (K=-1)\ , \end{cases} \tag{1.3}$$

with the constant K determining the curvature of the spatial hyper-surfaces (spherical, flat or hyperbolic, respectively). The metric in Eq. (1.2), which describes a homogeneous and isotropic universe, is referred to as Robertson-Walker metric.

It is evident, from the form of Eq. (1.2), that the factor $a^2(t)$ acts as a general expansion or contraction factor. In Fig. 1.1 space is pictured as a grid, which expands (or contracts) uniformly in time: points on the grid maintain their coordinates, and the difference between coordinates, usually referred to as comoving distance, stays constant. However, the physical distance clearly evolves, and it does so proportionally to the scale factor $a(t)$.

1.2 The Friedmann Equations

The metric evolves according to Einstein's field equations, a set of differential equations which relate it to the energy and matter content of the universe:

$$G_{\mu\nu} \equiv R_{\mu\nu} - \frac{1}{2} g_{\mu\nu} R = \frac{8\pi G}{c^2} T_{\mu\nu} \; . \tag{1.4}$$

On the left-hand side of Eq. (1.4), the Einstein tensor $G_{\mu\nu}$ depends on the metric: the Ricci tensor $R_{\mu\nu}$ is a combination of first and second derivatives of $g_{\mu\nu}$, and the Ricci scalar is the trace of the Ricci tensor, $R \equiv g^{\mu\nu} R_{\mu\nu}$. On the right-hand side, instead, the matter and energy contribution described by in the energy-momentum tensor $T_{\mu\nu}$, which combines the constituents of the universe.

In the case of a Robertson-Walker metric, the dynamics of the metric reduces to the dynamics of the scale factor $a(t)$, as apparent from Eq. (1.2). The energy-momentum tensor is that of a perfect fluid, with pressure p and energy density ρ; since the left-hand side of Eq. (1.4) has to obey homogeneity and isotropy, so does the right-hand side, therefore p and ρ can be functions of time only.

Due to the symmetries of the Robertson-Walker metric, there are only two independent Einstein equations, the time-time one and the space-space one. From the first one and a combination of both, the two Friedmann equations are obtained:

$$\left(\frac{\dot{a}}{a}\right)^2 = \frac{8\pi G}{3}\rho - \frac{Kc^2}{a^2} \; , \tag{1.5}$$

$$\frac{\ddot{a}}{a} = -\frac{4\pi G}{3}\left(\rho + \frac{3p}{c^2}\right) \; . \tag{1.6}$$

The scale factor $a(t)$ can be determined by solving these two equations, once its value at a certain point in time has been fixed; usually $a = 1$ is assumed at the present time. A combination of the Friedmann equations yields the equation for energy conservation, which reads

$$\frac{\mathrm{d}}{\mathrm{d}t}\left(a^3 \rho c^2\right) + p \frac{\mathrm{d}}{\mathrm{d}t}\left(a^3\right) = 0 \; ; \tag{1.7}$$

this clearly means that any two of the three equations above are independent.

A Robertson-Walker metric whose scale factor $a(t)$ obeys Eqs. (1.5, 1.6, 1.7) is called Friedmann-Lemaître-Robertson-Walker (FLRW) metric.

1.3 Components of the Universe

The relation between the pressure and the energy density, $p = p(\rho)$, is called the equation of state. For all cosmologically relevant fluids, it takes the simple form

$$p = w\rho c^2 \, , \tag{1.8}$$

where $w = 0$ in the case of collisionless, non-relativistic matter, and $w = 1/3$ in the case of radiation (or other forms of relativistic matter, e.g. neutrinos).

The equation of state, together with the conservation of energy stated in Eq. (1.7), gives the evolution of the density as a function of the scale factor:

$$\rho \propto a^{-3(1+w)} \, , \tag{1.9}$$

which translates to $\rho_{\rm m} \propto a^{-3}$ for matter and $\rho_{\rm r} \propto a^{-4}$ for radiation, respectively.

It is useful to consider also another form of energy-momentum tensor, namely that of vacuum, for which $T^{\rm vac}_{\mu\nu} \propto g_{\mu\nu}$: in this case, $p = -\rho$, which corresponds to a fluid characterised by a rather exotic equation of state, with $w = -1$, i.e. negative pressure. This component is also referred to as cosmological constant, or Λ, since, according to Eq. (1.9), its energy density is independent of the scale factor, $\rho_\Lambda \propto$ const. With the addition of a cosmological constant, Einstein's equations read

$$G_{\mu\nu} = \frac{8\pi G}{c^2} T_{\mu\nu} + \Lambda g_{\mu\nu} \, , \tag{1.10}$$

where

$$T^{\rm vac}_{\mu\nu} = \frac{\Lambda c^2}{8\pi G} g_{\mu\nu} \, ; \tag{1.11}$$

Eq. (1.10) can also be written in a form similar to that of Eq. (1.4), with an effective energy-momentum tensor formally given by $T^{\rm eff}_{\mu\nu} = T_{\mu\nu} + T^{\rm vac}_{\mu\nu}$.

A more general class of models with negative equation-of-state parameter w, either constant or varying in time, which goes under the name of dark energy (or quintessence), can be derived in the context of scalar fields and has gained increasing importance in the last decade; a more detailed discussion about dark energy will follow in Chapter 3.

1.4 The Expansion Rate

The general arguments adduced in the previous sections did not give any indication whether the scale factor $a(t)$ is increasing, decreasing, or constant: this information has to be sought observationally. The first evidence that the universe is expanding, i.e. that $\dot{a} > 0$ in the present epoch, was presented in 1929 by Hubble.

The relative cosmic expansion rate is defined as

$$H(a) = \frac{\dot{a}}{a} \,, \tag{1.12}$$

and it evolves according to Eq. (1.12); it is also referred to as Hubble function, and its value at present time is the Hubble constant, $H_0 = H(a = 1)$.

The quest for an accurate value of H_0 has always been extremely challenging, due mainly to the basic difficulty of establishing accurate distances over cosmologically significant scales. The most recent attempt comes from the HST Key Project: based on a Cepheid calibration of several secondary distance determination methods, they found $H_0 = 72 \pm 8$ km s^{-1} Mpc^{-1} (Freedman et al., 2001). As the Hubble constant is still not known to great accuracy, it is conventional to denote the ignorance about it through the dimensionless parameter h, such that $H_0 = 100\,h\,\mathrm{km\,s^{-1}\,Mpc^{-1}}$.

The first Friedmann equation, Eq. (1.5), shows that a particular value of the energy density exists, such that the curvature vanishes, namely

$$\rho_{\mathrm{cr}} = \frac{3H^2}{8\pi G} \,. \tag{1.13}$$

The critical density evolves in time, since H does, and its value at the present epoch is $\rho_{0,\mathrm{cr}} \simeq 1.9 \times 10^{-29}\,h^2\,\mathrm{g\,cm^{-3}}$. It is useful to scale the density relative to each component of the universe in units of the critical density, thus defining the density parameter $\Omega = \rho/\rho_{\mathrm{crit}}$.

After inserting the density parameters, Eq. (1.5) reads

$$H^2 = H_0^2 \left[\frac{\Omega_{\mathrm{r0}}}{a^4} + \frac{\Omega_{\mathrm{m0}}}{a^3} + \Omega_{\Lambda 0} + \frac{\Omega_{\mathrm{k0}}}{a^2} \right] \equiv H_0^2 E^2(a) \,, \tag{1.14}$$

where Ω_{r0}, Ω_{m0}, $\Omega_{\Lambda 0}$ and Ω_{k0} are the density parameters for radiation, matter, cosmological constant and curvature, respectively, calculated at the present day. In the last step of Eq. (1.14), the normalised expansion function $E(a)$ has been defined, which carries the information about the cosmic expansion history.

The expansion rate is the central object in this work. Efforts to observationally constrain its evolution over time have been very intense in the past few years, and will surely increase dramatically in the upcoming future. After all, as will be detailed in the next sections, $E(a)$ plays a crucial role in every quantity accessible to astronomical measurements and related to cosmology. Most of the current analyses tend to infer the shape of the expansion function by constraining the density parameters Ω_0 of the different species; this work, instead, aims at reconstructing $E(a)$ from observations without having specialised it to a particular Friedmann model, thus introducing as little theoretical prejudice as possible.

1.5 Expansion Regimes

The total value of the density parameter Ω, including all contributions but curvature, is related to the spatial geometry of the universe. By means of Ω, Eq. (1.5) can be written as

$$\Omega - 1 = \frac{Kc^2}{a^2H^2} \, , \tag{1.15}$$

which shows that the sign of K is in fact determined by whether Ω is greater, equal or less than one: $\rho < \rho_{\rm cr}$, i.e. $\Omega < 1$, corresponds to $K = -1$, i.e. open geometry; $\rho = \rho_{\rm cr}$, i.e. $\Omega = 1$, corresponds to $K = 0$, i.e. flat geometry; $\rho > \rho_{\rm cr}$, i.e. $\Omega > 1$, corresponds to $K = +1$, i.e. closed geometry.

The Friedmann equations can be solved exactly in a few, simple cases. The qualitative behaviour of some, particularly interesting regimes will be outlined in this section.

A property of universes made from fluids with $-1/3 < w < 1$ is the so-called Big Bang singularity, i.e. a point in time for which $a = 0$ and ϱ diverges. In such cases, Eq. (1.6) shows that $\ddot{a} < 0$ is valid for any value of the scale factor; this condition, along with the observational confirmation of the expansion of the universe, i.e. $\dot{a} > 0$,

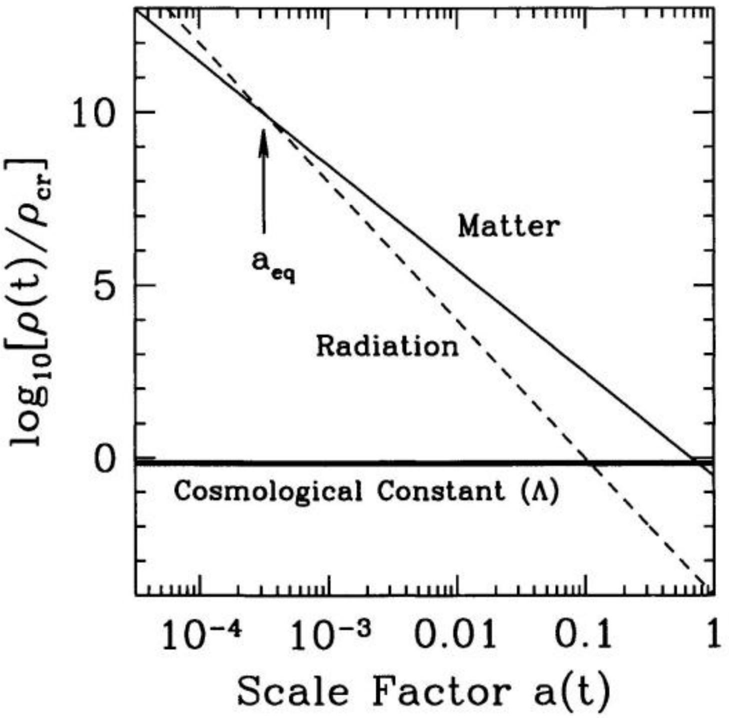

Figure 1.2: The evolution of the energy density as a function of the scale factor for the different components of the universe: non-relativistic matter, radiation and cosmological constant. The time of matter-radiation equality, a_{eq}, is indicated with an arrow, whereas the matter-Λ equivalence is visible on the rightmost part of the plot. From Dodelson (2003).

reveals the existence of such a singularity in the past (see the sketch in the left panel of Fig. 1.3). The deceleration is due to the gravitational attraction acting against the expansion. If the cosmological constant term is non-zero, some combinations of parameters exist, such that a could, theoretically, never vanish. However, these scenarios are ruled out by the observation of very distant quasars and the existence of the cosmic microwave background (Boerner & Ehlers, 1988).

Friedmann's equation also shows that fluids with $w < -1/3$, such as a cosmological constant or more exotic components, accelerate the cosmic expansion instead of decelerating it ($\ddot{a} > 0$).

The different dependence of density on the scale factor for the various components of the universe, discussed in Sect. (1.3) and summarised in Fig. 1.2, suggests

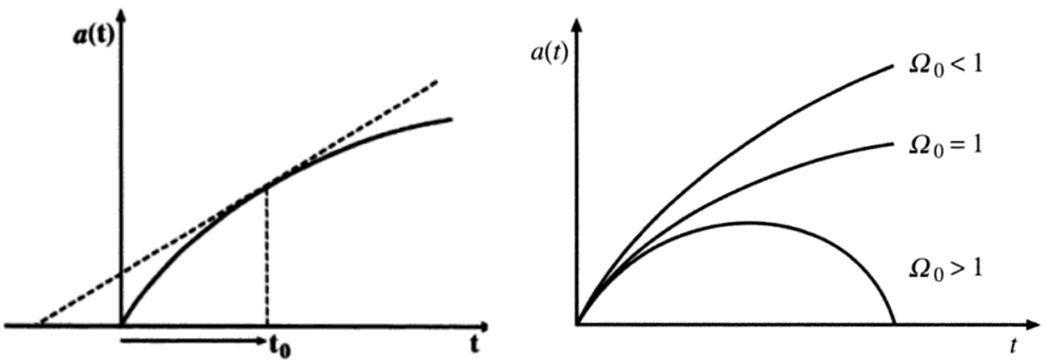

Figure 1.3: *Left panel:* The concavity of $a(t)$, along with its derivative being positive today, implies the existence of a singularity at a finite time in the past, when $a = 0$. *Right panel:* The evolution of the scale factor, with eternal expansion in the case of an open or flat universe, and an eventual recollapse in a closed universe; all three models have a vanishing cosmological constant. From Coles & Lucchin (2002).

that the cosmic evolution can be seen as a succession of several epochs, each of them characterised by the dominance of a different component. Radiation dominates in the early universe, because of its scaling $\propto a^{-4}$: substituting its contribution as the only relevant one in Eq.(1.14) and integrating over time yields the time evolution of the scale factor in this epoch, $a \propto \sqrt{t}$. At some point, referred to as matter-radiation equality ($a = a_{\rm eq}$), the radiation contribution equals that of matter, and becomes less and less important afterwards: matter starts dominating and, in the flat case (or before curvature becomes important), $a \propto t^{2/3}$, called the Einstein-de Sitter limit. A possible Λ-dominated phase can occur later in the evolution of the universe: in this case, known as de Sitter limit, the cosmological constant makes the universe expand exponentially, $a \propto \exp t$.

In a universe with no cosmological constant, the evolution of the scale factor in the future strictly depends on the geometry. For open and flat models ($K \leq 0$), Eq. (1.5) implies that $\dot{a} \neq 0$ always, which, along with the expansion observed today, means $\dot{a} > 0$ for any value of the scale factor: such models expand forever, with a constant deceleration in the flat case and with an expansion asymptotically linear in time in the open case, respectively. In the case of closed universes ($K = +1$), instead, an upper bound for the scale factor exists: the expansion ceases at $a = a_{\mathrm{max}}$, and the scale factor starts decreasing, reaching $a = 0$ inevitably again. These three regimes are summarised in the right panel of Fig. 1.3. An additional, non-vanishing cosmological constant clearly modifies this strict classification, allowing for mixed scenarios (e.g. an open universe that recollapses).

1.6 Redshift and Distances

Observationally, two measurable quantities are directly related to the expansion rate and can, thus, be employed to probe its evolution: the redshift and the distance to astrophysical objects.

The expansion of the universe causes light, which propagates from an emitting source to an observer, to be redshifted: the wavelength of a photon changes by the same amount as the scale of the universe changes while it travels. If λ_{e} is the emitted wavelength, it is related to the observed wavelength λ_{o} via

$$\frac{\lambda_{\mathrm{o}}}{\lambda_{\mathrm{e}}} = \frac{a_0}{a} = \frac{1}{a} \, , \tag{1.16}$$

where emission is associated to a generic value a of the scale factor, whereas observation is supposed to happen at present time, $a_0 = 1$; the redshift z is defined as the relative change in wavelength, namely

$$z \equiv \frac{\lambda_{\mathrm{o}} - \lambda_{\mathrm{e}}}{\lambda_{\mathrm{e}}} = \frac{1}{a} - 1 \, . \tag{1.17}$$

The redshift z and the scale factor a can thus be used in a totally equivalent way, bearing in mind that $a = 1/\left(1+z\right)$; evidently, at present time $z = 0$.

The redshift can be measured from spectroscopical observations, comparing the wavelength of the spectral lines in the radiation coming from astronomical sources to their rest-frame wavelength, which is measurable in the laboratory. Spectra, however, are “expensive” to acquire from an observational point of view, since very long exposure times are needed in order to collect enough light. Redshift can also be measured from combination of photometric observations performed in different wavelength bands: photometric redshifts are technically easier to obtain, but are affected by significantly larger uncertainties.

The definition of distance is not unique in a non-flat space-time: different measurements imply, in fact, different definitions of distance. The difference between physical distance, which changes over time according to the expansion, and the comoving distance, which stays constant, has already been outlined at the beginning of the chapter. In a more rigourous way, the proper distance $D_{\rm prop}(z_1, z_2)$ between a source object at redshift z_2 and an observer at $z_1 < z_2$ is the distance measured by the light-travel time, defined as $\mathrm{d}D_{\rm prop} = -c\,\mathrm{d}t$, which translates to

$$\mathrm{d}D_{\rm prop} = -c\,\frac{\mathrm{d}a}{\dot{a}} = -c\,\frac{\mathrm{d}a}{aH\left(a\right)} \;\;\rightarrow\;\; D_{\rm prop}\left(z_1, z_2\right) = \frac{c}{H_0}\int_{a_2}^{a_1} \frac{\mathrm{d}a'}{a'E\left(a'\right)} \,, \tag{1.18}$$

where the definition of the expansion rate (Eq. (1.12)) has been employed.

The comoving distance is, instead, measured on the comoving grid and is thus unaffected by the cosmic expansion: it is defined as $\mathrm{d}D_{\rm com} = -c\,\mathrm{d}t/a$, which yields

$$D_{\rm com}\left(z_1, z_2\right) = \frac{c}{H_0}\int_{a_2}^{a_1} \frac{\mathrm{d}a'}{\left(a'\right)^2 E\left(a'\right)} = \chi\left(z_1, z_2\right) \,. \tag{1.19}$$

However, none of the two distance measures defined above accurately describes most of the processes of interest. A classic way to determine distances in astronomy is to measure the angle subtended by a source of known physical size. The angular-diameter distance $D_{\rm A}$ is defined in analogy to the relation, which holds in Euclidean space, between the area δA and the solid angle $\delta\omega$ of an object, $\delta\omega D_{\rm A}^2 = \delta A$. Comparing this to Eq. (1.2), the solid angle of a sphere of constant radial coordinate χ has to be scaled by $a^2 f_K^2(\chi)$:

$$\frac{\delta A}{4\pi a_2^2 f_K^2\left[\chi\left(z_1, z_2\right)\right]} = \frac{\delta\omega}{4\pi} \,, \tag{1.20}$$

which implies

$$D_{\rm A}\left(z_1, z_2\right) = \left(\frac{\delta A}{\delta\omega}\right)^{1/2} = a_2 f_K\left[\chi\left(z_1, z_2\right)\right] \,. \tag{1.21}$$

Hence, the angular-diameter distance reads

$$D_{\rm A}\left(z_1, z_2\right) = a_2 f_K\left[D_{\rm com}\left(z_1, z_2\right)\right] = a_2 \frac{c}{H_0} f_K\left[\int_{a_2}^{a_1} \frac{\mathrm{d}a'}{\left(a'\right)^2 E\left(a'\right)}\right] \,, \tag{1.22}$$

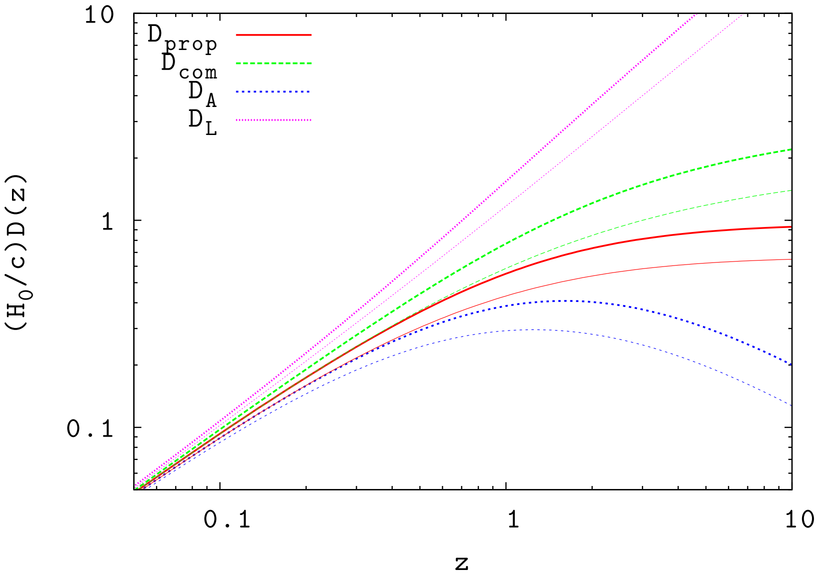

Figure 1.4: Four distance measures in a flat, expanding universe, as a function of redshift: proper distance (red solid curves), comoving distance (greed long-dashed curves), angular-diameter distance (blue short-dashed curves) and luminosity distance (magenta dotted curves). The light curves represent a model with no cosmological constant, with $\Omega_{\mathrm{m}0} = 1$, $\Omega_{\Lambda 0} = 0$, whereas the heavy curves represent a Λ-dominated universe, with $\Omega_{\mathrm{m}0} = 0.3$, $\Omega_{\Lambda 0} = 0.7$.

while the comoving angular-diameter distance is simply $d_{\mathrm{A}} = f_K\left(D_{\mathrm{com}}\right)$.

Another way of inferring distances in astronomy is to measure the flux F emitted by a source of known luminosity L, which, in Euclidean space, are related via the following relation:

$$F = \frac{L}{4\pi D_{\mathrm{L}}^2} \ , \tag{1.23}$$

where D_{L} is the luminosity distance. Again, generalising the Euclidean relation in order to hold in curved space yields the following expression for the luminosity distance,

$$D_{\mathrm{L}}\left(z_1, z_2\right) = \left(\frac{a_1}{a_2}\right)^2 D_{\mathrm{A}}\left(z_1, z_2\right) \ , \tag{1.24}$$

which is known as Etherington relation and holds for any space-time (Etherington, 1933). The luminosity distance can thus be written as

$$D_{\mathrm{L}}\left(z_1, z_2\right) = \left(\frac{a_1^2}{a_2}\right) \frac{c}{H_0} f_K\left[\int_{a_2}^{a_1} \frac{\mathrm{d}a'}{\left(a'\right)^2 E\left(a'\right)}\right] \ . \tag{1.25}$$

The four distances defined above are sketched in Fig. 1.4. It is worth noticing that, for small redshifts, i.e. $z \ll 1$, all these distance measures coincide:

$$D = \frac{cz}{H_0} + \mathcal{O}(z^2) \; , \tag{1.26}$$

where the linear evolution of the distance with redshift, which only holds locally, is referred to as Hubble law.

As is evident from the definitions of luminosity distance and angular-diameter distance, they are related to redshift via the expansion rate: sampling distances and redshifts from several distant sources is, thus, a powerful tool to probe the expansion history and the geometry of space. The distance-redshift relation is, in fact, one of the most important cosmological tests, as will be described in more detail in Chapter 2.

Furthermore, a very important scale in the universe is the size of the horizon, i.e. the maximum distance that photons can travel in the time since the Big Bang: because of the existence of such a singularity, time is finite in models with a Big Bang, thus causally connected regions are finite, too. The size of the horizon is given by $r_{\rm H} = c/H(a)$, and its present value, referred to as the Hubble radius, is approximately $c/H_0 = 3\,h^{-1}\,{\rm Gpc}$; the comoving horizon size reads $d_{\rm H} = c/aH(a)$, instead.

1.7 The Growth Rate of Linear Density Perturbations

Evidently, observations on relatively small scales show that the "local" universe is very far from being homogeneous and isotropic: the standard cosmological model has to allow deviations from smoothness. The current scenario for the formation of cosmic structures assumes that they arose from primordial, small fluctuations, which are supposed to have originated from quantum fluctuations during an early phase of accelerated expansion called inflation. These seed fluctuations then grew via gravitational instability, leading to the large scale distribution of structure in the universe.

The density fluctuations are described by the density contrast

$$\delta\left(\vec{x},a\right)=\frac{\rho\left(\vec{x},a\right)-\bar{\rho}\left(a\right)}{\bar{\rho}\left(a\right)}\,, \tag{1.27}$$

which quantifies the density inhomogeneity at comoving coordinates $\vec{x}$ relative to the mean density $\bar{\rho}(a)$. As long as $\delta \ll 1$, the fluctuation can be considered as a small perturbation to the homogeneous and isotropic background it is embedded in, and it can be treated within linear perturbation theory.

The growth of perturbations in the cosmic fluid should, in principle, be treated in a fully general-relativistic fashion, but since the perturbations are much smaller than the typical scale of the universe, the curvature effects can be neglected and a Newtonian treatment is sufficient. In order to describe the dynamics of the fluid, the continuity and Euler equations must be solved, along with Poisson's equation; by decomposing each variable (density, velocity, pressure and gravitational potential) into its homogeneous background value plus a small perturbation about it, these three equations can be brought into a single differential equation for the density contrast:

$$\ddot{\delta}+2H\dot{\delta}=\left(4\pi G\bar{\rho}\delta+\frac{c_{\mathrm{s}}^{2}\nabla^{2}\delta}{a^{2}}\right)\,, \tag{1.28}$$

where an adiabatic equation of state for the fluid has been specified, $p=c_{\mathrm{s}}^{2}\rho$, with sound speed c_{s}, and $\bar{\rho}$ represents the background value of the density. Decomposing the density contrast into plane waves, $\delta(\vec{x},a)=\delta(a)\exp(-\mathrm{i}\vec{k}\cdot\vec{x})$, Eq. (1.28) can be written as

$$\ddot{\delta}+2H\dot{\delta}=\delta\left(4\pi G\bar{\rho}-\frac{c_{\mathrm{s}}^{2}k^{2}}{a^{2}}\right)\,, \tag{1.29}$$

where the expansion of the universe acts as a friction term, thus slowing down gravitational instability. Depending on the background model, a time-dependent frequency can be derived from Eq. (1.29), either real or imaginary, with a limiting wave number k_{J} discriminating between oscillating and evolving solutions: only perturbations larger than the corresponding length scale, $\lambda_{\mathrm{J}}=2\pi/k_{\mathrm{J}}$, called the Jeans length, can grow (or decay).

As pointed out by several different empirical facts, a very important one of which is the amount of anisotropy observable in the cosmic microwave background radiation, it is legitimate to describe the density of the late universe as being dominated by cold dark matter (CDM), i.e. a pressure-less, weakly interacting matter component. In this case, Eq. (1.29) reduces to

$$\ddot{\delta} + 2H\dot{\delta} - 4\pi G\bar{\rho}\delta = 0 \; ; \tag{1.30}$$

cold dark matter has vanishing Jeans length, i.e. perturbations of any scale can grow. In the Einstein-de Sitter limit, which is, in any case, a good approximation for the early universe after matter domination, inserting a power-law ansatz for the time evolution of the density contrast, $\delta \propto t^n$, into Eq. (1.30) yields either $n = 2/3$ or $n = -1$: the first of the two cases identifies the growing mode, which implies $\delta \propto a$, whereas the decaying mode is clearly not interesting in the context of structure formation. The growing mode is usually described by the growth factor, $D_+(a)$, which quantifies the growth of the density contrast from an initial value δ_0: $\delta(a) = D_+(a)\delta_0$.

For later times, when the Einstein-de Sitter limit is no more a good approximation, Eq. (1.30) must be solved separately for each cosmological model to obtain the growth factor. For LCDM models, i.e. models with cold dark matter and a non-vanishing cosmological constant, a very good approximation to the growth factor is given by a fitting formula, depending on the parameters $\Omega_{\rm m}$ and Ω_Λ, due to Carroll et al. (1992). A more rapid expansion, as the one induced by the cosmological constant term, retards the growth of structure, as can be read from Fig 1.5.

It is worth noticing that Eq. (1.30), thus the growth factor, depends only on the expansion rate, $H(a)$, and on the evolution of the background density, $\bar{\rho}(a)$, which, in turn, depends again on the expansion rate, and on the matter density parameter $\Omega_{\rm m0}$. Underlying any measurement involving the distribution of matter on large scales, the growth rate of linear structure formation is one of the two most important functions in cosmology, along with the expansion rate, which is, however,

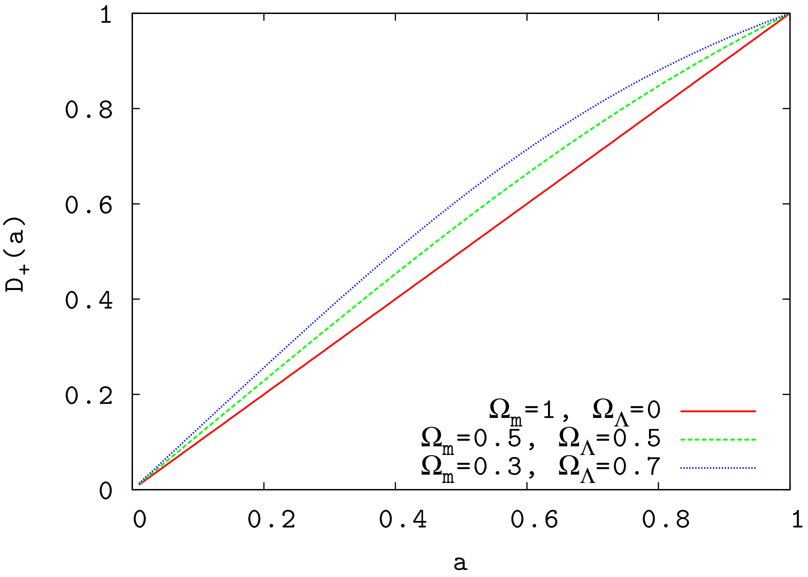

Figure 1.5: The linear growth rate for a variety of models: the red line corresponds to an Einstein-de Sitter model, where the rate is constant in time; the green and blue lines correspond to two flat ΛCDM models, with increasing contribution from a cosmological constant, and show that the growth rate is higher at early times and lower at later times, indicating that structure forms earlier in models with a lower matter density parameter.

required to calculate the growth factor itself.

As long as only scales well within the horizon are considered, Eq. (1.30) can be obtained also from relativistic perturbation theory, as was mentioned at the beginning of this section. It can also be derived in the presence of a cosmological constant (or any other smooth background), which would change the unperturbed gravitational potential, but not its perturbation: the additional contribution would appear in the expansion rate, whereas $\bar{\rho}$ and δ would still denote matter density only.

1.8 The Power Spectrum

The central limit theorem, a powerful statistical tool, states that the superposition of several random processes drawn from the same probability distribution, in the limit of infinitely many processes, turns into a Gaussian, if the variance of the parent distribution is finite. Since the current belief agrees that density anisotropies in the universe derive from inflationary quantum fluctuations, which fulfil the above requisites, it is reasonable to assume that the density field is a Gaussian random field: it is thus characterised by two quantities, namely its mean, which vanishes because of the definition of δ, and its variance.

In the linear regime, perturbations grow in place, i.e. their comoving scale is preserved: hence, it is convenient to study the evolution of density perturbations in Fourier space. The variance of δ in Fourier space defines the power spectrum $P(k)$:

$$\langle\hat{\delta}(\vec{k})\hat{\delta}^*(\vec{k}')\rangle = (2\pi)^3 P(k)\delta_{\rm D}(\vec{k}-\vec{k}') \ , \tag{1.31}$$

where $\hat{\delta}$ is the Fourier transform of the density contrast δ, whereas $\delta_{\rm D}$ is Dirac's delta distribution, which guarantees that modes relative to different wave numbers are uncorrelated, in order to preserve homogeneity; on the other side, $P(k)$ does not depend on the direction of $\vec{k}$ because of isotropy. Back in real space, the back-transform of the power spectrum is the two-point correlation function,

$$\xi(r) = \langle\delta(\vec{x})\delta(\vec{x}+\vec{r})\rangle \ , \tag{1.32}$$

which measures the coherence of the density contrast for all points in the universe separated by a distance r; the correlation function is averaged both over all positions $\vec{x}$ and over all orientations of $\vec{r}$, and does only depend on the modulus of $\vec{r}$, because of isotropy.

Historically, the normalisation of the matter power spectrum is expressed in terms of the variance of the density contrast within spheres of radius $R = 8\,h^{-1}$ Mpc, where the variance within spheres of generic radius R is given by

$$\sigma_R^2 = \int_0^\infty \frac{{\rm d}^3k}{(2\pi)^3}\, P(k)W_R^2(k) \ , \tag{1.33}$$

where $W_R(k)$ is a window function, selecting the modes contributing to the variance, and is usually either a Gaussian or a step function in Fourier space. Because of the special value of $8\,h^{-1}$ Mpc, the normalisation of the power spectrum is referred to as σ_8, and the observational determination of this parameter is a largely debated subject in modern cosmology.

Along with the expansion of the universe, the size of causally connected regions grows, thus also the scale of perturbations which can be in causal contact: a perturbation of (comoving) wavelength λ is said to "enter the horizon" when $\lambda = d_{\mathrm{H}}$.

In Sect. (1.7) it was explained that, during matter domination, perturbations grow like $\delta \propto a$; it can be analogously derived that, during radiation domination, they evolve faster, $\delta \propto a^2$. The time of matter-radiation equivalence plays, in fact, a special role in this context. If a perturbation enters the horizon before equivalence, its collapse time-scale is determined by the dark matter density, but the expansion time-scale is determined by the radiation density, which is higher and prevails: the growth is interrupted, and will start again only when matter begins dominating. Therefore, perturbations that are small enough to enter the horizon before a_{eq}, experience a suppression of growth with respect to larger perturbations. The horizon size at equivalence sets a scale $k_0 = 2\pi/d_{\mathrm{H}}(a_{\mathrm{eq}})$: perturbations with $k > k_0$ stop growing when they enter the horizon ($a = a_{\mathrm{enter}}$) and continue after equivalence, whereas larger perturbations ($k < k_0$) can grow all the time. Since larger modes continue growing $\propto a^2$ during radiation domination, the relative suppression of smaller modes is given by

$$f = \left(\frac{a_{\mathrm{enter}}}{a_{\mathrm{eq}}}\right)^2 = \left(\frac{k_0}{k}\right)^2 \;; \tag{1.34}$$

in the last equality of Eq. (1.34) use was made of $k \propto 1/\lambda$, and of

$$\lambda \propto \begin{cases} a_{\mathrm{enter}} & (a_{\mathrm{enter}} \ll a_{\mathrm{eq}}) \\ a_{\mathrm{enter}}^{1/2} & (a_{\mathrm{eq}} \ll a_{\mathrm{enter}} \ll 1)\ , \end{cases} \tag{1.35}$$

because of the different evolution of the horizon size before and after equivalence.

The matter power spectrum evolves quadratically with density: hence, $P(k) \propto a^4$ during radiation domination and $P(k) \propto a^2$. Starting from a primordial value of the power spectrum $P_0(k)$, at a_{enter} it has changed to $P_{\mathrm{enter}}(k) = k^{-4}P_0(k)$; because of what Eq. (1.35) states, this last result is independent of radiation or matter domination. It is reasonable to assume that the total power of the density fluctuations entering the horizon should be independent of time, i.e. $k^3 P_{\mathrm{enter}}(k) = \mathrm{const}$, which, along with the previous considerations, implies that the primordial power spectrum must scale linearly with the wave number, $P_0(k) \propto k$. This spectrum is scale-invariant and is usually referred to as Harrison-Zel'dovich-Peebles power spectrum (Harrison, 1970; Peebles, 1982; Peebles & Yu, 1970; Zeldovich, 1972); it is also in agreement with the most credited inflationary models, which predict that fluctuations should arise from inflation with an (almost) scale-invariant spectrum.

Because of the suppression of growth on small-scales, the final expression of the power spectrum reads

$$P(k) \propto \begin{cases} k & (k \ll k_0) \\ k^{-3} & (k \gg k_0)\ . \end{cases} \tag{1.36}$$

1.9 Non-Linear Evolution

When the density contrast approaches unity, linear theory is no longer sufficient to describe the growth of structures. The so-called Zel'dovich approximation is a formalism to describe the onset of non-linear evolution, which treats the fluid kinematically, decomposing it into particles and following their trajectories. The main result stated by the Zel'dovich approximation is that the non-linear collapse of structures is anisotropic, leading to the formation of sheets and filaments.

As non-linear evolution proceeds, also this approach breaks down, not being able to describe the gravitational interaction after particle trajectories cross. In order to perform detailed studies, the use of numerical simulations is required: in the past two decades, great progress in this field has been achieved, thanks to both increased computer performances and the development of sophisticated numerical algorithms. Structure formation over cosmological times and extremely large volumes has been simulated by several different teams, confirming that matter in the universe is extremely clustered, with highly non-linear, bound structures, known as galaxy clusters, forming at the intersection of filaments: filamentary structures fragment into smaller lumps, which stream towards higher-density regions, leaving behind giant voids. A representation of the cosmic web, as this picture of the large-scale universe is referred to, can be observed in Fig.1.6: it shows the output of the

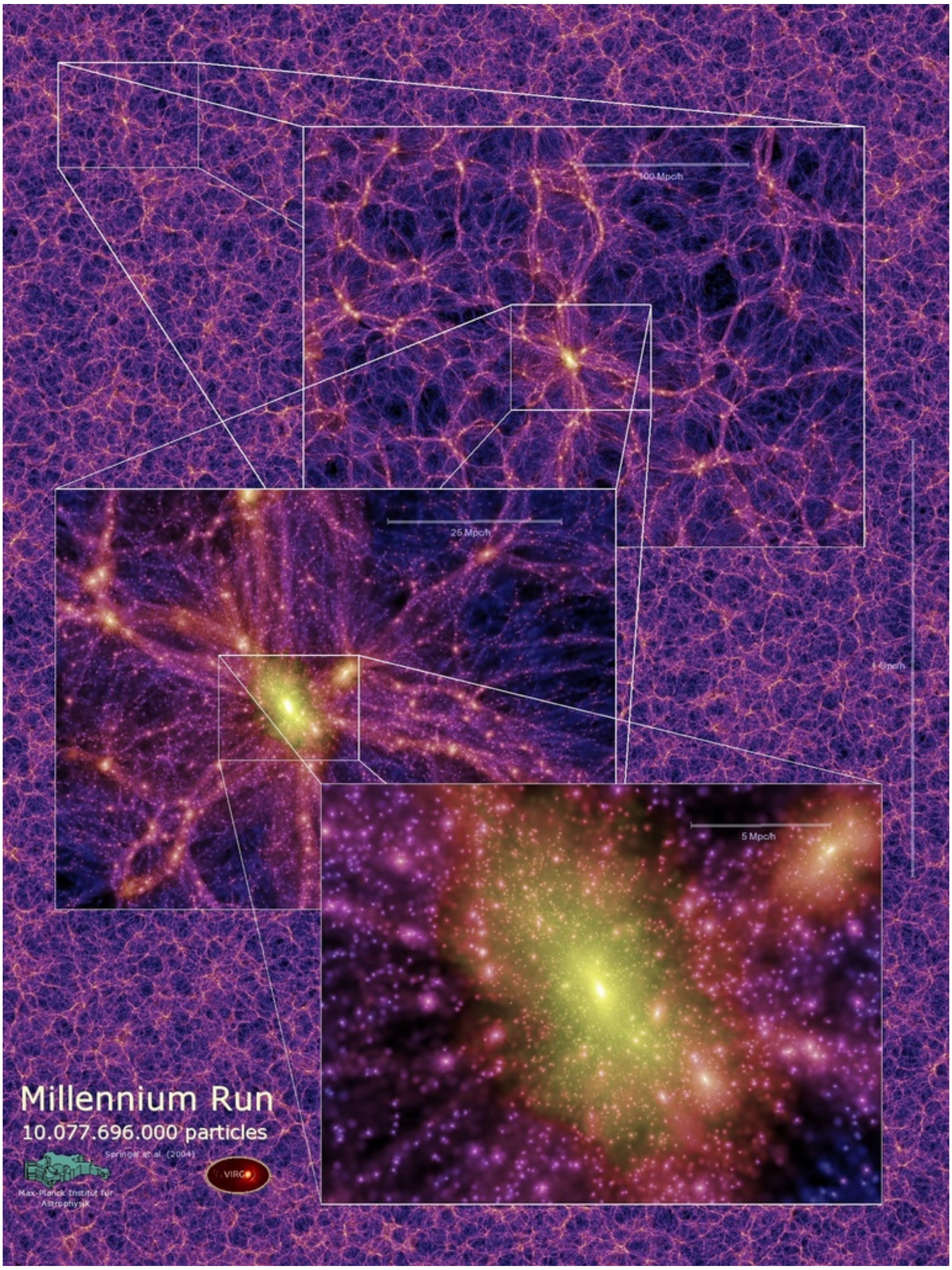

Figure 1.6: The dark matter density field on various scales, as achieved by the Millennium Run, a simulation which followed the evolution of $\sim 10^{10}$ dark matter particles from $z = 127$ to the present, within a cubic volume with $500\,h^{-1}$ Mpc side. From the Virgo Consortium.

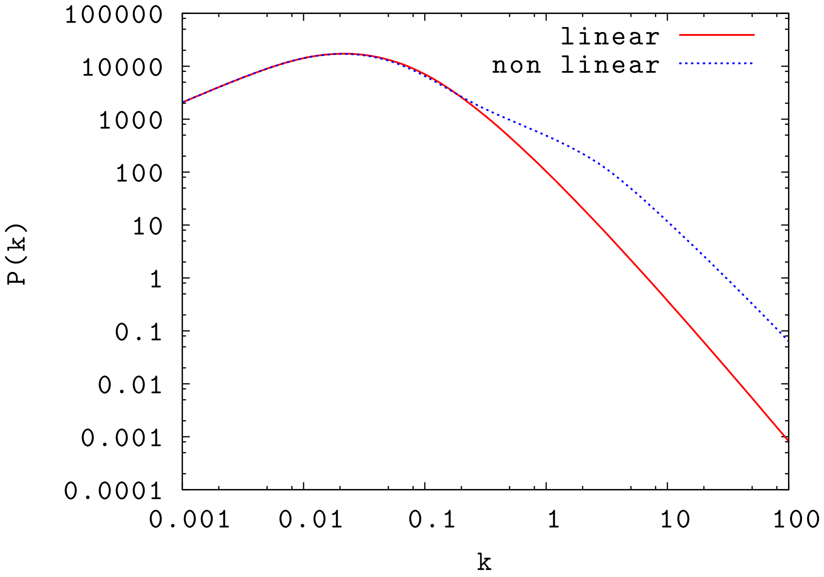

Figure 1.7: Matter power spectrum for a ΛCDM universe: the solid, red curve represents the linear power spectrum, whereas the dashed, blue line shows the increased power on small scales due to non-linear effects. The non-linear power spectrum has been calculated using the prescription by Peacock & Dodds (1996).

Millennium simulation, one of the largest ones performed so far, realised by Springel et al. (2005). As evident from the background of the image, the structure on large scale is extremely homogeneous and isotropic, whereas the sequence of close-ups, centred on one of the many galaxy clusters present in the simulation, reveals the high degree of clumpiness on smaller scale. The bright dots correspond to high concentrations of dark matter, which are associated with sites where baryonic matter collects in gaseous form and, eventually, condenses, giving rise to the formation of stars and galaxies.

During non-linear evolution, overdense regions contract, i.e. matter is transported from larger to smaller scales: the assumption that, during linear regime, perturbations grow in place, is thus no longer valid. This mode coupling enhances the amplitude of the power spectrum on small scales, at the expense of intermediate scales, whereas large scales continue to evolve linearly and independently, as shown in Fig. 1.7.

A first attempt to achieve an analytic description of non-linear clustering evolution, carried out by Hamilton et al. (1991), assumed that the two-point correlation functions in the linear and non-linear regimes are simply related by a scaling relation. A generalisation of this assumption to non-flat models, calibrated on N-body simulations, has been presented, along with analytic formulae describing the non-linear deviation of $P(k)$ on small scales, by Peacock & Dodds (1996), and a more precise and updated version followed (Smith et al., 2003).

Chapter 2

Measuring the Universe: Observational Tests for Cosmology

In this Chapter, the main observational tests representing strong motivation in favour of the standard cosmological model are reviewed, along with an explanation of the physical mechanism underlying each of these measurements. The use of type-Ia supernovae as standard candles and of the baryon acoustic oscillations (BAO) as standard ruler, along with the extremely powerful tool offered by cosmic shear, i.e. the gravitational lensing effect due to the large scale distribution of matter in the universe, are treated in detail, being the main objects of investigation in this work. For the sake of completeness, also the main results coming from the cosmic microwave background (CMB) and from big-bang nucleosynthesis (BBN) are outlined.

2.1 Type-Ia Supernovae

As anticipated in Section 1.6, the distance-redshift relation is a very powerful tool to probe the expansion of the universe. Measuring redshifts is straightforward, whereas the determination of distances to objects of unknown intrinsic brightness is more tricky. One of the most popular techniques is to identify a class of objects which have the same intrinsic brightness, usually referred to as standard candles:

probably the most reliable standard candles that can be observed up to high redshifts are supernovae of type Ia. Reviews on the cosmological implications of type-Ia supernovae can be found in Leibundgut (2001) and Perlmutter & Schmidt (2003).

2.1.1 Standard Candles and Cosmology

For an object of known absolute magnitude M, a measurement of its apparent magnitude m at a given redshift z yields an estimate of the luminosity distance, $D_{\mathrm{L}}(z)$, called the distance modulus:

$$\mu = m - M = 5\log(D_{\mathrm{L}}) + K + 25 \ , \tag{2.1}$$

where the K-correction appears because the emitted and detected photons from the receding object have different wavelength. The luminosity distance also depends on the underlying cosmology through the expansion rate, as shown in Eq. (1.25).

The effect of the cosmological parameters on the luminosity distance is illustrated in Fig. 2.1, where the distance modulus is plotted for four different models with various combinations of $\Omega_{\mathrm{m}0}$ and $\Omega_{\Lambda 0}$: the models share the same linear behaviour at very low z, but become clearly distinguishable for intermediate and high z.

However, degeneracies amongst the parameters arise, since different combinations of $\Omega_{\mathrm{m}0}$ and $\Omega_{\Lambda 0}$ might yield similar luminosity distances, at least over certain redshift ranges. The contours of constant apparent magnitude in the ($\Omega_{\mathrm{m}0}$, $\Omega_{\Lambda 0}$) plane, for two standard candles located at $z = 0.5$ and $z = 1$, respectively, are plotted in Fig. (2.2): one measurement of m narrows the range of possible values for $\Omega_{\mathrm{m}0}$ and $\Omega_{\Lambda 0}$ to a strip between two of the contour lines shown in the plot, depending on the measurement uncertainty; two measurements at different z define two different strips, whose crossing identifies a more narrowly constrained allowed region for the parameters, shown as a shaded rhombus. Clearly, such degeneracies can be lifted either with a better accuracy of the measurements or with the collection of distance measurements over several different redshifts.

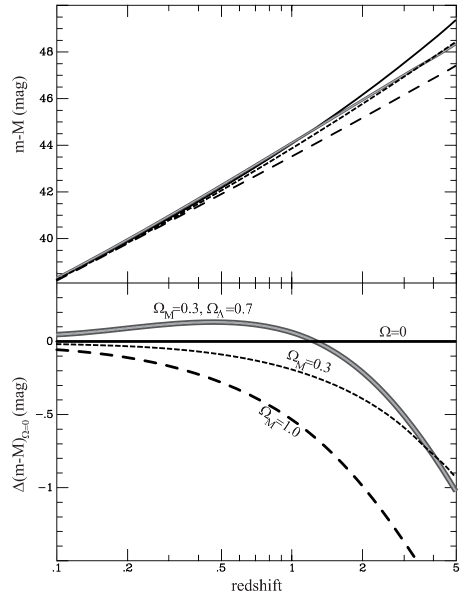

Figure 2.1: *Top panel:* The distance modulus as a function of redshift for four different cosmological models: an empty universe with $\Omega_{\rm m0} = 0$, $\Omega_{\Lambda 0} = 0$ (solid line), an open universe with $\Omega_{\rm m0} = 0.3$, $\Omega_{\Lambda 0} = 0$ (short-dashed line), and two flat universes with $\Omega_{\rm m0} = 0.3$, $\Omega_{\Lambda 0} = 0.7$ (hatched line) and $\Omega_{\rm m0} = 1$, $\Omega_{\Lambda 0} = 0$ (long-dashed line), respectively. *Bottom panel:* The empty universe has been subtracted from the other models to highlight the differences. From Perlmutter & Schmidt (2003)

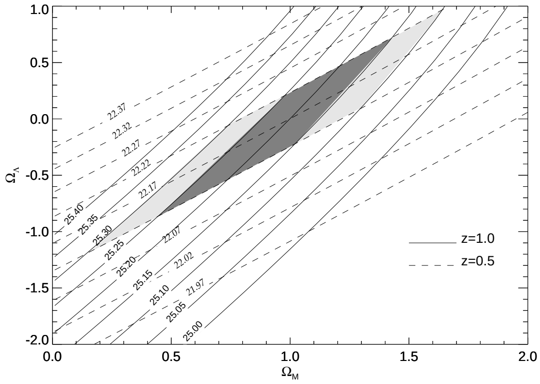

Figure 2.2: Contours of constant apparent magnitude (in the R band) in the ($\Omega_{\rm m0}$, $\Omega_{\Lambda 0}$) plane: the dashed lines show the predicted values for a standard candle at $z = 0.5$, and the solid line for one at $z = 1$, respectively. The dark-shaded region represents the allowed region for a measurement uncertainty of 0.05 mag on both objects, whereas the grey-shaded region refers to an uncertainty of 0.1 mag. From Goobar & Perlmutter (1995)

2.1.2 Type-Ia Supernovae as Standard Candles

A supernova is a stellar explosion, observable as a sudden rise in brightness followed by a gentle decline; the rise in brightness is so intense that the supernova reaches, at its peak, the luminosity of an entire galaxy ($L \sim 10^{10} \cdots 10^{11} L_\odot$).

Several types of supernova exist, related to different explosion dynamics. However, for historical reasons the classification does not directly reflect the different explosion mechanisms. It refers to differences in the observed spectra, instead: supernovae of type II have hydrogen lines in their spectra, whereas supernovae of type I have no hydrogen; furthermore, type Ia supernovae have silicon lines, type Ib have no silicon but helium lines, type Ic have neither silicon nor helium.

Supernovae of type II, Ib and Ic originate from the collapse of the core of a massive star, followed by the generation of a shock wave and the ejection of the stellar envelope, and the difference in the spectral composition is due to a possible loss of the outer envelope prior to explosion. Supernovae of type Ia, instead, arise by the thermonuclear explosion of a white dwarf (the final evolutionary stage of low-mass stars, with $M < 8M_\odot$) which accretes mass from a companion in a binary system and reaches the Chandrasekhar mass limit of $M_{\rm Ch} \sim 1.4 M_\odot$. When the mass is close to $M_{\rm Ch}$, nuclear burning begins in isolated places in the degenerate core: due to the degenerate environment, it produces a dramatic rise in temperature, followed by a thermonuclear runaway and an explosion, or more precisely a deflagration, which completely destroys the system. During the thermonuclear runaway, the carbon and oxygen in the core are converted into ^{56}Ni, which then decays into ^{56}Co and, eventually, ^{56}Fe. For further details about supernova Ia explosion, see the review by Hillebrandt & Niemeyer (2000).

The existence of an approximately fixed amount of mass, namely $M_{\rm Ch}$, to trigger the explosion, suggests that the amount of energy released during the process is also fixed: hence, type-Ia supernovae are expected to be standard candles. Observationally, a substantial scatter in the absolute luminosity has been observed: until the early '90s, it was commonly believed that this was due to observational errors, but

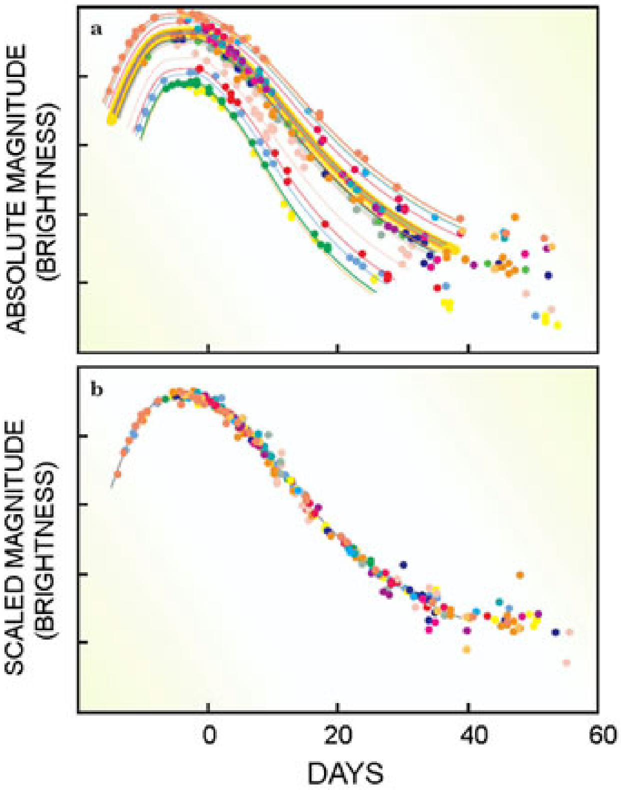

Figure 2.3: A series of light curves of type-Ia supernovae from the Calán/Tololo Supernova Survey. In the *upper plot* the scatter in absolute luminosity is evident, along with its correlation with the width of the light curve; in the *bottom plot* the scatter is substantially reduced after rescaling the luminosity according to the stretch of the light curve. From the Supernova Cosmology Project.

subsequent technical improvements demonstrated that such a difference does exist. However, observations of local samples of supernovae Ia revealed the existence of an empirical relation between the absolute luminosity at maximum and the rate of the luminosity decline, i.e. the width of the light curve: a brighter object corresponds to a broader light curve (Phillips, 1993; Phillips et al., 1999). This tight correlation, as illustrated in Fig. 2.3, allows a calibration of the absolute luminosity of the supernovae, which are thus not standard, but standardisable candles.

The width-luminosity relation of type-Ia supernovae has been long employed as purely empirical, since a thorough theoretical explanation was lacking; recently, however, detailed, time-dependent radiative transfer calculations have been performed, shedding light on its origin. Kasen & Woosley (2007) have shown that the faster decline of luminosity in cooler, dimmer supernovae is not only due to their lower opacity, which translates into shorter diffusion time for photons, but mainly to their faster ionisation evolution: supernova colours evolve towards the red, driven by blanketing due to FeII/CoII lines, more rapidly in dimmer objects, where the onset of such lines happens earlier due to their lower temperature.

2.1.3 Type-Ia Supernovae as Cosmological Probes

The 1990s witnessed the compilation of the first large samples of local type-Ia supernovae, followed by the observation of a handful high-z objects, which showed that distant supernovae appear to be fainter than their local counterparts (Riess et al., 1998; Perlmutter et al., 1999). This first, claimed evidence for an accelerated expansion of the universe was initially controversial, and other, non-cosmological explanations for the dimming of distant supernovae were sought.

A possible astrophysical effect which could explain distant supernovae being fainter than nearby ones is absorption due to dust in the intergalactic medium: a grey dust, which absorbs equally at all wavelengths, could mimic the effect of an accelerating universe, while remaining undetected to multi-colour photometry. Such a behaviour is possible when the dust grains are larger than the wavelength (a diameter of 0.1 μm is sufficient in the optical); however, the dust would re-emit the absorbed radiation in the infrared, and the very high density required to falsify the cosmological effect would be detectable in observations of the infrared background, where such a signal has not been detected. Hence, grey dust alone is not enough to explain the overall dimming of distant supernovae; however, a detailed model for the intergalactic dust is a crucial ingredient, in order to obtain accurate constraints on the cosmological parameters.

Another possible systematic effect which might influence the cosmological constraints inferred from the analysis of supernovae Ia is evolution: supernovae are, in fact, calibrated at low-redshifts, but their properties are then extrapolated to higher redshifts, which is not straightforward to assume. The evolution effects involve the metallicity, expected to be lower at higher z, and the colours, expected to be bluer at higher z. Again, there is no compelling evidence that such effects could falsify the overall cosmological conclusions; however, accurate analyses of possible evolution are performed on the supernova samples in order to keep this systematic under control.

Also gravitational lensing, i.e. the deflection of light due to an intervening mass distribution (for a more thorough discussion see Section 2.5), affects distant supernovae and has to be taken into account in the calculation of systematic errors, but does not rule out any of the cosmological interpretations of the supernova data.

In the past decades, a few other samples of supernovae Ia have been compiled, including more objects, improved control over systematics and increasingly smaller error bars: it is worth mentioning the "Gold" sample (Riess et al., 2004, 2007), the SuperNova Legacy Survey (SNLS, Astier et al. 2006), the ESSENCE sample (Wood-Vasey et al., 2007; Davis et al., 2007) and a recent compilation of data from all of the above, namely the "Union" sample (Kowalski et al., 2008). All of them, as the early data sets, but now with significantly higher precision, point towards a late-time phase of accelerated expansion, thus suggesting the existence of a non-vanishing cosmological constant, or an alternative, more exotic component which would produce such an effect. As an example, the results from the SNLS first-year data release are shown in Fig. 2.4.

2.2 Baryon Acoustic Oscillations

As standard candles can be used to probe the redshift evolution of the luminosity distance, objects of known physical size located at different z allow to probe the evolution of the angular-diameter distance: such objects, if they exist, are referred to as standard rulers. It was proposed by Kellermann (1993) to employ compact

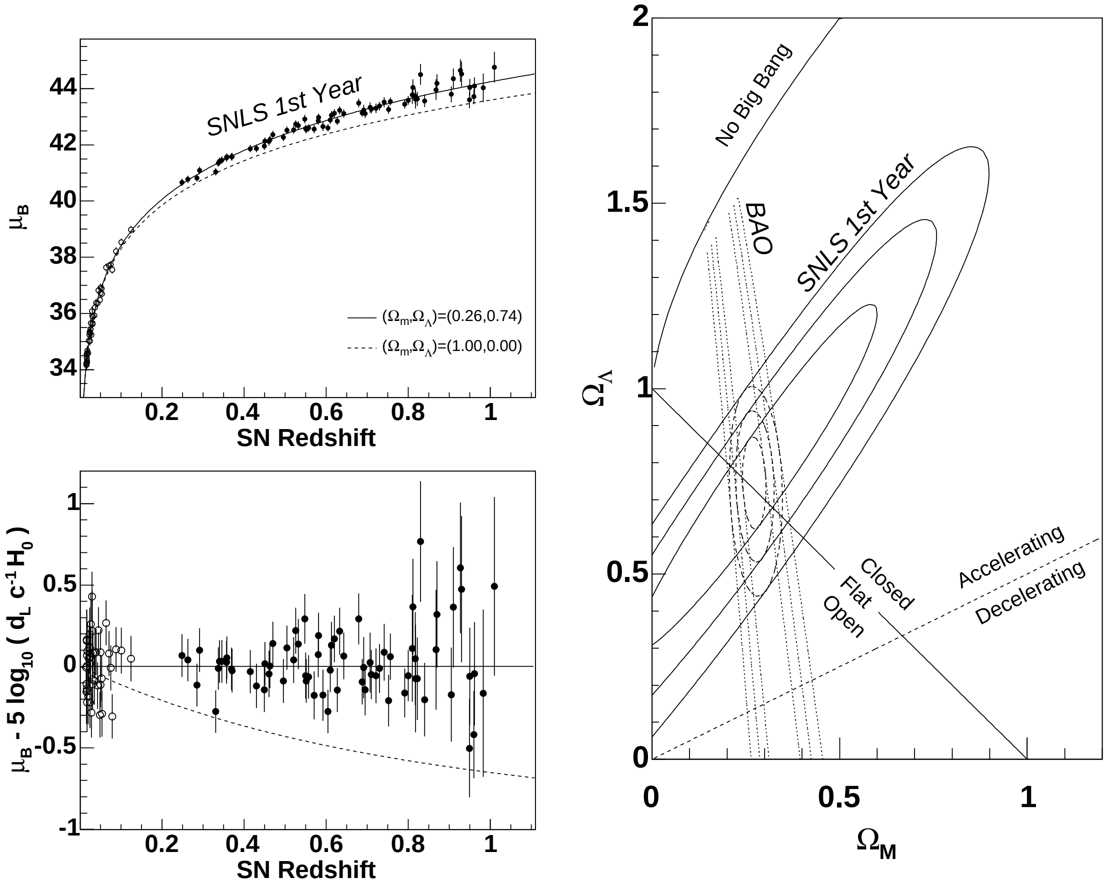

Figure 2.4: *Left panel:* The distance modulus as a function of redshift for the SNLS and nearby type-Ia supernovae, compared to a flat, Λ-dominated universe (solid line) and a flat, matter-dominated one (dashed line), with the residuals for the best fit to a ΛCDM model below. *Right panel:* The contours at the 1-σ, 2-σ and 3-σ confidence level in the ($\Omega_{\rm m0}$, $\Omega_{\Lambda 0}$) plane from the SNLS data alone (solid lines), from the Baryon Acoustic Oscillations (BAO, see Section 2.2 for more details) from the SDSS LRG sample alone (Eisenstein et al. 2005, dotted lines), and the joint contours (dashed lines). From Astier et al. (2006).

radio sources for this purpose, assuming that their properties, and particularly their average size, do not strongly depend on redshift; very soon, however, the weakness of this assumption and the large scatter in the data were pointed out, thus ruling out the possible conclusions obtained from this method. Although it is not at all obvious that astronomical objects feasible as standard rulers should exist, the cosmological scale to be measured need not be the size of an actual object: it can also be a characteristic scale imprinted e.g. on the distribution of matter on large scales, such as that of the baryonic acoustic oscillations observable in the matter power spectrum, already detected using current quality data.

2.2.1 Standard Rulers

The comoving sizes of an object, or feature, located at redshift z in the line-of-sight ($r_\parallel$) and transverse ($r_\perp$) directions are related to the observed sizes Δz and $\Delta\theta$ through the expansion rate and the angular-diameter distance, respectively:

$$r_\parallel = \frac{c\Delta z}{H\left(z\right)} \; , \quad r_\perp = \left(1+z\right) D_{\mathrm{A}}\left(z\right) \Delta\theta \; . \tag{2.2}$$

If the true scales, $r_\parallel$ and $r_\perp$, are somehow known, a measurement of the observed dimensions, Δz and $\Delta\theta$, provides an estimate of $H(z)$ and $D_{\mathrm{A}}(z)$, which can be then used to probe cosmology.

It is worth emphasising that, if the size of the standard ruler can be measured in both directions, i.e. parallel and perpendicular to the line of sight, this geometrical test provides two independent probes of the expansion rate.

2.2.2 Baryon Acoustic Oscillations as Standard Rulers

Baryon acoustic oscillations are a feature of the power spectrum of large scale structure, first pointed out by Peebles & Yu (1970) and Sunyaev & Zeldovich (1970), and represent an excellent candidate for the standard ruler test, as proposed by Blake & Glazebrook (2003) and Seo & Eisenstein (2003).

Prior to the epoch of recombination, the baryons in the universe are coupled to the photons, and the interaction between radiation pressure and gravitational instability, due to overdensities in the dark matter component, produces a series of sound waves in the baryon-photon fluid. After recombination, baryons and photons evolve separately: the acoustic oscillations are not only imprinted in the cosmic microwave background, as discussed in Section 2.4, but also in the spacial distribution of baryonic and, eventually, non-baryonic dark matter. The acoustic feature is in fact detectable as an enhancement in the statistical correlation at a certain separation, given by the scale of the sound horizon at the time of recombination, i.e. the comoving distance that a sound wave can travel before recombination:

$$s = \int_0^{t_{\rm rec}} c_{\rm s}\,(1+z)\;{\rm d}t = \int_0^{a_{\rm rec}} \frac{c_{\rm s}\,{\rm d}a}{a\,H\,(a)}\;, \tag{2.3}$$

where $t_{\rm rec}$ and $a_{\rm rec}$ refer to the epoch of recombination, and $c_{\rm s}$ is the speed of sound. Hence, the characteristic scale of baryon oscillations is determined once the epoch of recombination and the sound speed of the fluid, which depends on the baryon-to-photon ratio, are known: since these two quantities are very precisely constrained by CMB measurements, the acoustic oscillation scale can be calibrated and used as a standard ruler.

The series of acoustic oscillations in the power spectrum is visible in Fig. 2.5. The theoretical value of the BAO scale is rather straightforward to calculate, and corresponds roughly to $s = 150\,h^{-1}\,{\rm Mpc}$, whereas its measurement from a power spectrum analysis of a galaxy redshift survey is complicated by several factors. First, the matter power spectrum is estimated through the power spectrum of galaxies, therefore a bias to describe the clustering of galaxy has to be assumed: a linear bias, i.e. $P_{\rm gal} = b^2\,P_\delta$, is often used, motivated by observations of the matter power spectrum and of weak gravitational lensing (see, e.g. Lahav et al. 2002; Simon et al. 2007). Then, non-linear growth of perturbations smoothes out the acoustic features on small scales: at $z \sim 0$, only the first two peaks are not erased, whereas at higher z many more features are preserved outside of the region affected by non-linear effects, as indicated by the arrows in Fig. 2.5. The harmonic sequence in the

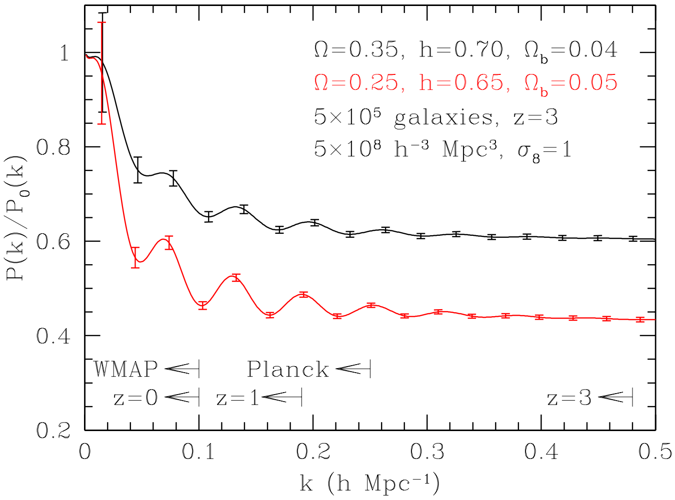

Figure 2.5: The linear power spectrum for two different cosmological models, divided by a baryon-free power spectrum in order to enhance the wiggles. The error bars correspond to forecast measurements obtained from a planned survey at $z = 3$, with survey parameters as indicated in the figure. The arrows at the bottom show the scale where non-linear effects set in, thus washing out the acoustic peaks, as a function of redshift, along with the scales probed by the CMB satellite experiments WMAP and Planck. From Seo & Eisenstein (2003).

power spectrum translates into a single peak in the correlation function, and the effect of non-linearities is to broaden this peak. Another effect which contributes to the broadening of the peak is the redshift-space distortion due to the peculiar velocities of galaxies, since the measured position of a galaxy in redshift space might not correspond to its initial position. Additionally, the redshift data need to be converted into real space in order to compute the two-point correlation function, and this process requires a cosmological model to be assumed: an incorrect choice of the background parameters would lead to a distorted power spectrum and the acoustic peaks would appear in the wrong places, although it has been proven that this effect is not dramatic, at least at low z.

2.2.3 Baryon Acoustic Oscillations as Cosmological Probes

The detection of the baryon acoustic peak requires the statistical measurement of a small signal, hence the mapping of millions of objects over very large volumes, and

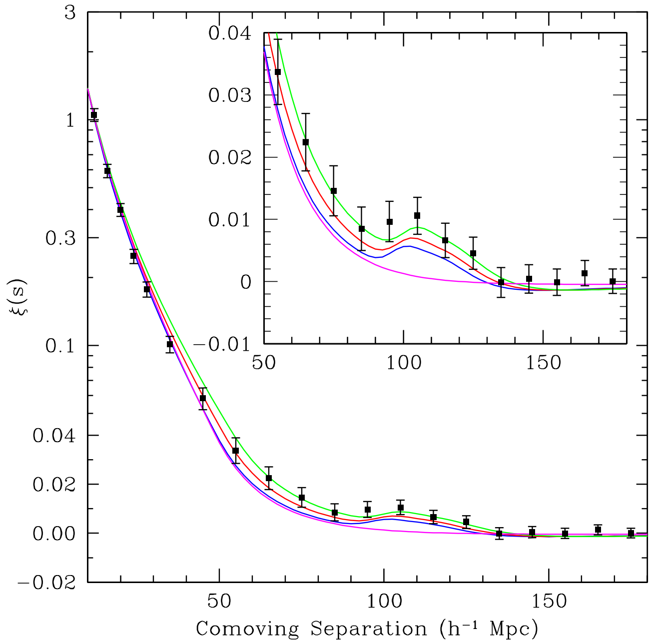

Figure 2.6: The first detection of the BAO feature in the correlation function from the SDSS LRG sample, plotted along with four different cosmological models: from top to bottom, the first three, with $\Omega_{\rm m}h^2 = 0.12$ (green line), $= 0.13$ (red line), and $= 0.14$ (blue line), all have a baryonic contribution of $\Omega_{\rm b}h^2 = 0.024$, whereas the fourth is a pure CDM model, with $\Omega_{\rm m}h^2 = 0.105$ and no baryons, hence no acoustic peak (magenta line). From Eisenstein et al. (2005).

it was only possible with the last-generation of galaxy redshift surveys, such as the Two-Degree Field Galaxy Redshift Survey (2dFGRS, Colless et al. 2001) and the Sloan Digital Sky Survey (SDSS, York et al. 2000).

Eisenstein et al. (2005) first measured the BAO feature using a spectroscopic sample of over 40,000 luminous red galaxies (LRG) from the SDSS, covering the redshift range $0.16 < z < 0.47$. The LRG are the brightest and reddest galaxies in the universe, and can be easily seen up to $z > 0.2$, which is typically the limit for galaxies in the main SDSS galaxy survey: the LRG sample thus probes a much larger volume. The detection of the peak in the correlation function, at a separation of $\sim 100\,h^{-1}$ Mpc, is illustrated in Fig. 2.6; this result confirmed once more the standard cosmological model. The peak also provided a standard ruler to measure the distance to a single, intermediate redshift, $z = 0.35$, which can be used to constrain cosmology, especially in combination with other, independent measurements.

Analogously, Percival et al. (2007a) also detected the baryon acoustic signature in a combination of the 2dFGRS and SDSS main galaxy samples, and used it to measure the distance to $z = 0.2$. This measurement, along with the one at higher z from Eisenstein et al. (2005), was employed to constrain parameters in ΛCDM models, achieving results slightly different from those obtained using type-Ia supernovae from the SNLS: BAO data seem to require a stronger cosmic acceleration at low redshift.

Future galaxy surveys are expected to detect the BAO signature in several redshift bins, thus yielding a measurement of the standard ruler at more than one (or two) values of z; spectroscopic surveys will be able to measure the scale both in the radial and transverse direction, thus providing independent estimates of the angular-diameter distance and of the expansion rate for each redshift bin, whereas photometric surveys, due to their much larger uncertainties in z, will only be sensitive to the transverse direction, thus probing only $D_{\mathrm{A}}(z)$.

2.3 Big-Bang Nucleosynthesis

In the very early universe, which was extremely hot and dense, there were no neutral atoms nor bound nuclei: any atom or nucleus which could be possibly produced would be immediately destroyed by collisions with high energy photons. As the universe cooled down, well below the typical binding energies of nuclei (of order $\sim$MeV), the nucleosynthesis of light elements set in. The abundance of the emerging nuclides depend on the duration of the event, on the density and the thermal properties of the components involved: hence, knowledge of the conditions of the early universe, which can be computed from the Friedmann equations, and of the relevant nuclear cross-sections allows to calculate the expected primordial abundance of all the relevant species, namely deuterium (D), ^{3}He, ^{4}He and ^{7}Li.

The simplest, standard model for big-bang nucleosynthesis has only one free parameter, namely the density of baryons: the predicted abundance for the aforementioned light elements are shown in Fig. 2.7 as a function of the baryon density.

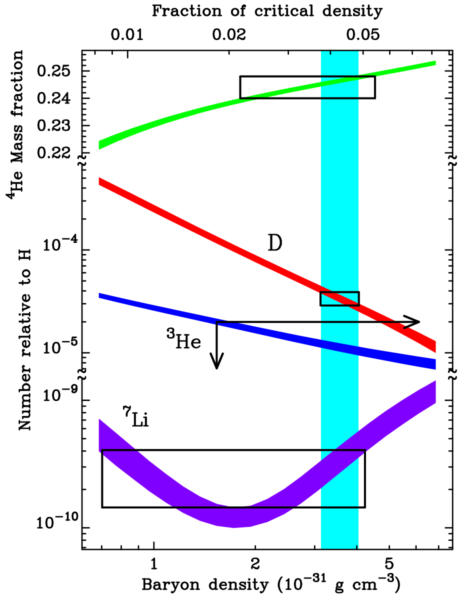

Figure 2.7: Theoretical predictions from the standard BBN model for the abundance of ^{4}He, D, ^{3}He and ^{7}Li as a function of baryon density, along with observational bounds. The vertical band is fixed by deuterium measurements only. From Burles et al. (1999).

The plot also shows a fair agreement between the theoretical predictions and observational bounds, thus being a remarkable confirmation of the big bang.

A comparison between the measured abundance of these light elements and the theoretical expectation is a probe of baryon density, but is not at all trivial, since each of the nuclei experienced a different evolution after the end of the primordial nucleosynthesis phase. Deuterium is the best baryometer, because it is only destroyed during stellar processes, thus its post-BBN evolution is monotonically decreasing and any measurement of its abundance provides a lower bound to the primordial one. The post-BBN evolution of the other elements is more complicated, instead: ^{3}He is also produced in the interior of stars, and may survive and return to the interstellar medium; the abundance of ^{4}He also increases, being the main product of hydrogen fusion in stars; ^{7}Li is both burned and formed in stellar interiors. Hence, detailed stellar and galactic evolution models are required, in order to infer accurate cosmological information from BBN.

As shown by the vertical band in Fig. 2.7, deuterium abundance represents the best diagnostic of baryon density, yielding values which closely match those from current non-BBN data, such as from measurements of the cosmic microwave background: the most up-to-date result is $0.0207 \leq \Omega_{\mathrm{b}} h^2 \leq 0.0234$, or $0.0399 \leq \Omega_{\mathrm{b}} \leq 0.045$. For further details on BBN, see the reviews by Kneller & Steigman (2004) and Steigman (2007).

2.4 Cosmic Microwave Background

The nuclear fusion of ^{4}He and other light nuclei in the early universe, described in the previous section, is necessary to explain the fact that about a quarter of the baryonic matter in the universe is composed of ^{4}He, and that such a high abundance cannot be produced only by fusion in stars. Big-bang nucleosynthesis is only possible if the temperature of the early universe was hot enough for a sufficiently long period. This fact, along with some simple considerations, allows to predict that the current temperature of the universe should be of order $T_0 \approx 1 \cdots 5\,\mathrm{K}$ (Alpher & Herman, 1949). The predicted cosmic microwave background was first detected serendipitously by Penzias & Wilson (1965), and this detection was sufficient evidence in favour of the big bang universe. Following measurements of the energy density in this radiation did nothing but confirm this result, showing that the CMB photons have a perfect black-body spectrum (as reported by the FIRAS experiment was placed on-board the COBE satellite, Mather et al. 1994). The temperature of the CMB today is $T_0 = 2.726\,\mathrm{K}$, which constrains the present value of the radiation density parameter in photons: $\Omega_{\mathrm{r}0} = 8.51 \times 10^{-5}$.

The CMB offers a look at the universe when photons, until then tightly bound to electrons, as the black-body spectrum confirms, last scattered off electrons and started travelling freely through space: this happened when the universe was only 380,000 years old, corresponding to a redshift of $z \approx 1100$. The CMB is thus one of the most powerful probes of the early universe, but it also carries a huge load of additional information, since its photons have traversed almost the whole universe after the last scattering epoch.

2.4.1 Structures in the Cosmic Microwave Background

Although extremely close to being perfectly isotropic, the CMB deviates from isotropy on several different levels, because of various reasons. First, the peculiar motion of the Earth, which moves towards the Virgo Cluster along with the Solar System, the Galaxy and the whole Local Group, imprints a dipolar pattern on the CMB with a relative amplitude of order $\approx 10^{-3}$. A series of cosmologically relevant anisotropies follow, characterised by an even smaller amplitude, of order $\approx 10^{-5}$.

The matter density fluctuations from which cosmic structure formed via gravitational instability also leave an imprint on the temperature fluctuations of the CMB: photons which were in an overdense region at last scattering lose energy, becoming cooler, whereas those that were in an underdense region gain energy, becoming hotter. This source of anisotropy, particularly effective on very large scales, is called the Sachs-Wolfe effect (Sachs & Wolfe, 1967).

As already mentioned while introducing the BAO feature in the matter power spectrum (see Section 2.2.2), before the epoch of recombination the cosmic fluid underwent a series of acoustic oscillations: the overdensities in the dark-matter component, in fact, compressed the fluid due to their gravity, whereas the radiation pressure of the tightly coupled baryon-photon fluid acted against gravity, driving the fluctuations apart (Peebles & Yu, 1970; Sunyaev & Zeldovich, 1970).

The power spectrum of the CMB is obtained by decomposing the relative temperature fluctuations into spherical harmonics: the coefficients

$$a_{lm} = \int \mathrm{d}^2\theta \frac{\delta T}{T} Y_{lm}(\vec{\theta}) \tag{2.4}$$

are averaged over m (which is allowed because of isotropy) to form the angular power spectrum

$$C_l = \frac{1}{2l+1} \sum_{m=-l}^{l} |a_{lm}|^2 \, . \tag{2.5}$$

The acoustic oscillations imprint a series of peaks and troughs in the power spectrum, whose amplitude and position depend on the background cosmology. Since only fluctuations smaller than the comoving sound horizon s at recombination are affected by acoustic oscillations, this defines a characteristic angular scale of $\theta = s/w(a_{\mathrm{rec}}) =$

0.66 deg, which can be read off the first peak in the power spectrum and, being a standard ruler, is a powerful probe of the geometry of the universe.

On smaller scales, fluctuations are damped due to the increase of the photon mean free path as recombination proceeds, which is not an instantaneous process: structures smaller than the diffusion scale, which corresponds to an angular scale of $\theta \approx 10\,\mathrm{arcmin}$, are damped (Silk damping, Silk 1968).

The three physical mechanisms described above are visible in the power spectrum of the CMB, shown in Figs. 2.8 and 2.9.

Other anisotropies, usually referred to as secondary, are due to propagation effects of the CMB photons and carry information about the distribution and formation of cosmic structure. The integrated Sachs-Wolfe effect is determined by the fact that photons travel through potential fluctuations which evolve in time: the depth of the potential well can be different when the photon enters and leaves it, thus yielding a non-zero net effect. The Sunyaev-Zel'dovich effect, instead, is due to Thomson scattering of CMB photons off electrons in the hot gas of galaxy clusters, which modifies the spectrum of the CMB observed in the line of sight of a cluster (Sunyaev & Zeldovich, 1972). These and other effects, which represent noise to those who are interested in the CMB as a probe of the early universe physics, are extremely important for studies of galaxy clusters and large-scale structure.

It is worth mentioning that, since it arises from Thomson scattering, which is sensitive to polarisation, the CMB is also expected to have a polarised intensity of order 10% of the total intensity, which carries much additional information on the properties of the early universe.

2.4.2 The Cosmic Microwave Background as a Cosmological Probe

The first 25 years of CMB observations yielded an extremely smooth picture: no anisotropies had been detected, besides the dipole. Anisotropies due to matter fluctuations in the early universe were long sought for, but not detected. If matter is tightly coupled to radiation, such fluctuations must have a relative amplitude of

Table 2.1: Some of the cosmological parameters obtained from the 5-year WMAP data (Komatsu et al., 2009), without and with the additional constraints imposed by BAO (Percival et al., 2007a) and type-Ia supernovae (Kowalski et al., 2008). Only the estimate of $\Omega_{\rm tot}$ does not assume spacial flatness; the further parameters are estimated assuming $K = 0$ and $w = -1$. Adapted from Komatsu et al. (2009).

Parameter	WMAP-5 alone	WMAP-5 + BAO + SNe
$\Omega_{\rm tot}$	$1.099^{+0.100}_{-0.085}$	1.0052 ± 0.0064
$\Omega_{\rm m}$	0.258 ± 0.030	0.274 ± 0.015
$\Omega_{\rm b}$	0.0441 ± 0.0030	0.0456 ± 0.0015
Ω_Λ	0.742 ± 0.030	0.726 ± 0.015
h	$0.719^{+0.026}_{-0.027}$	0.705 ± 0.013
σ_8	0.796 ± 0.036	0.812 ± 0.026

order $\approx 10^{-3}$: the fact that they were not detected suggested the hypothesis that the universe must be dominated by a matter component which does not interact with light, i.e. dark matter (Peebles, 1982).

The first detection of cosmologically motivated anisotropy in the CMB was possible with the satellite experiment COBE (Smoot et al., 1992). Since then, ground-based balloon experiments and interferometers made great progress in the field of CMB observations; the final breakthrough is represented, though, by the NASA satellite WMAP (Wilkinson Microwave Anisotropy Probe), launched in 2001.

The first-year results from WMAP (Spergel et al., 2003) already represented a striking evidence in favour of an almost flat ΛCDM model, and the following analyses, based on the 3-year and 5-year data, respectively, achieved even more precise constraints on the cosmological parameters (Spergel et al., 2007; Komatsu et al., 2009). Results from the 5-year WMAP data are presented in Fig. 2.8: the all-sky map of temperature fluctuations is shown in the left panel, whereas the measured power spectrum is shown in the right panel, with its prediction in the best-fit ΛCDM cosmology superimposed (the parameters of the model are listed in Tab. 2.1).

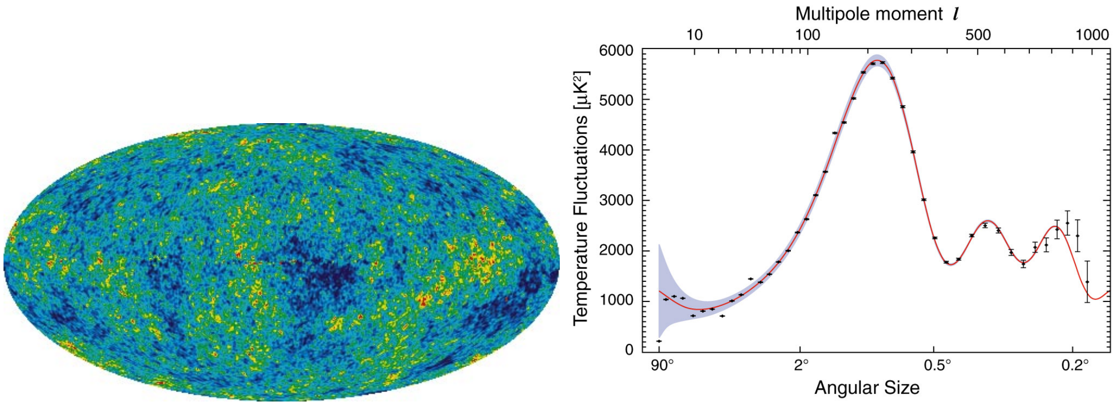

Figure 2.8: *Left panel*: The cosmic microwave temperature fluctuations from the 5-year WMAP data seen over the full sky. The average temperature is 2.726 K, and the colours represent temperature fluctuations: red regions are warmer and blue regions are colder. *Right panel*: The angular power spectrum of CMB temperature fluctuations from the 5-year WMAP data, with its prediction in the best-fit ΛCDM cosmology superimposed. From the NASA/WMAP Science Team.

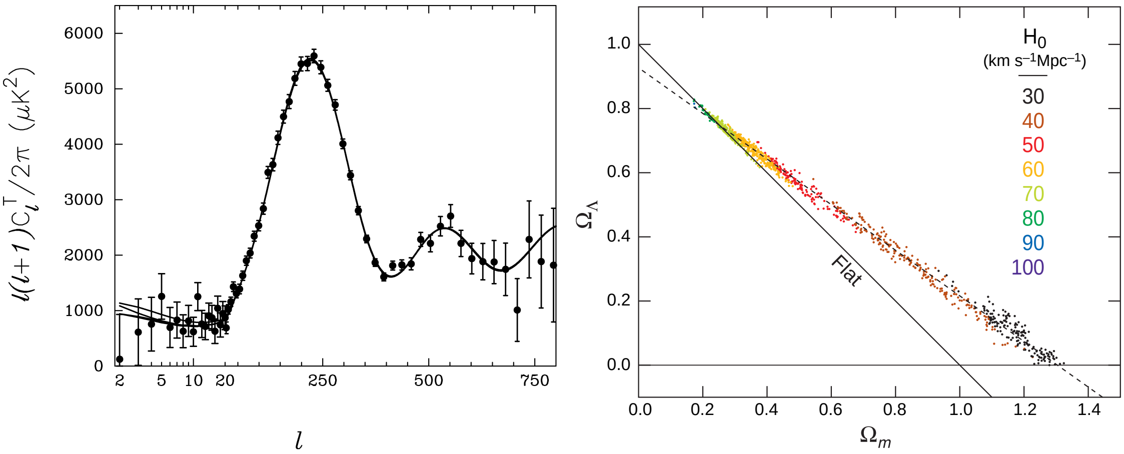

Figure 2.9: *Left panel*: The CMB power spectrum from the first-year WMAP data (filled circles) and the prediction in four nearly degenerate models, with $\Omega_k = 0.0, -0.05, -0.10, -0.20$ (solid lines). From Efstathiou (2003). *Right panel*: Range of non-flat cosmological models consistent with the three-year WMAP data only. The different colours correspond to values of the Hubble constant as indicated in the figure. From Spergel et al. (2007)

It is worth remarking that the Hubble constant cannot be independently measured from CMB data alone: it can be estimated from the location of the first peak only if a flat model is assumed and a dark-energy equation of state $w = -1$. The result, $H_0 = 70.1 \pm 1.3\,\mathrm{km\,s^{-1}\,Mpc^{-1}}$, is in perfect agreement with that achieved by the HST Key Project (Freedman et al. 2001, see Section 1.4). Turning the argument around, the position of the first peak alone is not able to constrain the geometry of the universe: as pointed out by Efstathiou (2003), the location of the peak depends on the size of the sound horizon, thus on the expansion rate at recombination. It is therefore affected by a strong degeneracy between the matter density, the dark-energy density and curvature, which precludes reliable estimates of either the dark-energy density parameter or the Hubble constant from CMB data alone, even under the assumption of $w = -1$. The left panel of Fig.2.9 shows the CMB power spectrum for four different models, with different curvature and Hubble constant, which are all nearly degenerate, apart from the very low multipoles, and all fit well the first-year WMAP data. As illustrated in the left panel of Fig. 2.9, the CMB data constrain a very tight treck in the $(\Omega_\mathrm{m}, \Omega_\Lambda)$ plane, which is slightly tilted with respect to the line identifying flat universes; however, fixing the Hubble constant from an external experiment, narrows down the constraints significantly. Whereas the 3-year WMAP data alone do not disfavour models with no cosmological constant, when combined with the value of H_0 from the HST Key Project they strongly point towards Λ-dominated, spatially flat universes.

The future of CMB observations lies in the European satellite mission Planck, expected to be launched in early April 2009: with its extended frequency coverage and an angular resolution of $\approx 5\,\mathrm{arcmin}$, it will achieve unprecedented control over the subtraction of foregrounds, one of the most delicate issues in CMB data analysis, and is also expected to measure the polarisation signal and to detect thousands of galaxy clusters through the Sunyaev-Zel'dovich effect (Tauber, 2004; Valenziano et al., 2007).

2.5 Cosmic Shear

The phenomenon of gravitational lensing, i.e. the deflection of light rays coming from distant sources by the gravitational effect of foreground massive bodies, is a powerful tool for cosmology. In particular, weak gravitational lensing due to the large-scale distribution of matter, usually referred to as cosmic shear, proved to be a very promising probe to test cosmological models and constrain their parameters.

2.5.1 Basics of Gravitational Lensing

This section introduces the basic formalism to describe gravitational lensing, following the review by Bartelmann & Schneider (2001), to which the reader is referred for a more detailed treatment.

The simplest example of a gravitational lens is a point mass M: in this case, the deflection experienced by a light ray is quantified through the deflection angle

$$\hat{\alpha} = \frac{4GM}{c^2\xi} \ , \tag{2.6}$$

where ξ is the impact parameter, assumed to be much larger than the Schwarzschild radius of the lens, $\xi \ll R_{\mathrm{S}} \equiv 2GM/c^2$.

In the case of a weak gravitational field, the field equations of general relativity can be linearised and the deflection due to an ensemble of point masses can be described as the sum of the deflections due to the individual point masses. Hence, the total deflection angle for a three-dimensional mass distribution with volume density $\rho(\vec{r})$, where $\vec{r} = (\xi_1, \xi_2, r_3)$ and the incoming light ray propagates along r_3, reads

$$\vec{\hat{\alpha}}(\vec{\xi}) = \frac{4G}{c^2} \int \mathrm{d}^2\xi' \int \mathrm{d}r_3'\, \rho(\xi_1', \xi_2', r_3')\, \frac{\vec{\xi} - \vec{\xi}'}{|\vec{\xi} - \vec{\xi}'|^2} \ ; \tag{2.7}$$

in the derivation of the previous equation, the actual light path, which is deflected, has been approximated as a straight line in the neighbourhood of the lens, since the deflection is small, in analogy to the Born approximation. The inner integral in Eq. (2.18) defines the surface mass density, i.e. the mass density projected onto a plane perpendicular to the incoming light ray,

$$\Sigma(\vec{\xi}) = \int \mathrm{d}r_3\, \rho(\xi_1, \xi_2, r_3) \ , \tag{2.8}$$

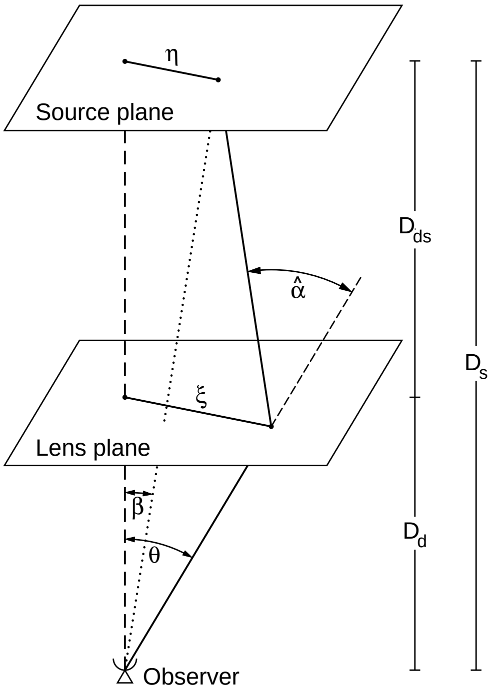

Figure 2.10: Sketch representing a typical gravitational lens system in the thin-lens approximation. From Bartelmann & Schneider (2001).

which allows to rewrite Eq. (2.18) as

$$\vec{\alpha}(\vec{\xi}) = \frac{4G}{c^2} \int \mathrm{d}^2\xi' \, \Sigma(\vec{\xi'}) \, \frac{\vec{\xi} - \vec{\xi'}}{|\vec{\xi} - \vec{\xi'}|^2} \, . \tag{2.9}$$

This expression is valid in most astrophysical situations, where the deflecting body is a well defined object (e.g. a galaxy or a galaxy cluster) and the deflection of light rays within the mass distribution is much smaller than the scale on which the properties of the mass distribution vary significantly; this is, however, not the case when considering the deflection due to the large scale structure, which is discussed in the following section.

The geometry of a typical gravitational lens system is illustrated in Fig. 2.10, where a mass concentration, placed at redshift z_d (or at angular-diameter distance D_d), deflects light rays coming from a source, placed at redshift z_s (or at angular-diameter distance D_s), and D_ds represents the angular-diameter distance between the lens and the source; in general, $D_\mathrm{ds} \neq D_\mathrm{s} - D_\mathrm{d}$. In the absence of other, neighbouring deflecting bodies and in the thin-lens approximation, i.e. if the extent of the lens is much smaller than both $D_{\rm ds}$ and $D_{\rm s}$, the light rays can be approximated by two straight lines with a kink near the deflector: the magnitude and the direction of the kink are described by the deflection angle $\vec{\hat{\alpha}}$. The lens and source planes are defined as planes perpendicular to a straight line from the observer to the lens, which is referred to as the optical axis of the system.

In Fig. 2.10, the source position on the source plane is denoted by the two-dimensional vector $\vec{\eta}$ and the impact parameter of light rays on the lens plane by $\vec{\xi}$, which are related to the deflection angle through

$$\vec{\eta} = \frac{D_{\rm s}}{D_{\rm d}}\,\vec{\xi} - D_{\rm ds}\,\vec{\hat{\alpha}}(\vec{\xi}) \ ; \tag{2.10}$$

defining the angular coordinates $\vec{\beta}$ and $\vec{\theta}$ such that $\vec{\eta} = D_{\rm s}\,\vec{\beta}$ and $\vec{\xi} = D_{\rm d}\,\vec{\theta}$, Eq. (2.10) can be rewritten as

$$\vec{\beta} = \vec{\theta} - \frac{D_{\rm ds}}{D_{\rm d}}\,\vec{\hat{\alpha}}\,(D_{\rm d}\,\vec{\theta}) \equiv \vec{\theta} - \vec{\alpha}(\vec{\theta}) \ ; \tag{2.11}$$

where the last step defines the reduced deflection angle $\vec{\alpha}(\vec{\theta})$. Eq. (2.11) is referred to as the lens equation, and it means that a source with true angular position $\vec{\beta}$ can be seen by an observer at angular positions $\vec{\theta}$ which satisfies Eq. (2.11). Due to the non-linearity of the lens equation, multiple solutions may exist for a fixed $\vec{\beta}$, giving thus rise to multiple images of the same source. The capability of a lens to produce multiple images is quantified by the dimensionless surface mass density, also referred to as convergence:

$$\kappa(\vec{\theta}) = \frac{\Sigma(D_{\rm d}\,\vec{\theta})}{\Sigma_{\rm cr}} \ , \tag{2.12}$$

where $\Sigma_{\rm cr} = (c^2/4\pi G)\cdot(D_{\rm s}/D_{\rm d}D_{\rm ds})$ is the critical mass density and depends on the configuration of the lens system. If $\Sigma \geq \Sigma_{\rm cr}$ somewhere in the lens, it produces multiple images and is referred to as “strong”.

The reduced deflection angle, in terms of the convergence, reads

$$\vec{\alpha}(\vec{\theta}) = \frac{1}{\pi}\int {\rm d}^2\theta' \kappa(\vec{\theta'})\,\frac{\vec{\theta} - \vec{\theta'}}{|\vec{\theta} - \vec{\theta'}|^2} \ , \tag{2.13}$$

which implies that $\vec{\alpha}$ can be written as $\vec{\alpha} = \nabla\psi$, where

$$\psi(\vec{\theta}) = \frac{1}{\pi}\int {\rm d}^2\theta' \kappa(\vec{\theta'})\,\ln|\vec{\theta} - \vec{\theta'}| \tag{2.14}$$

is the deflection potential; ψ is the two-dimensional analogue of the Newtonian gravitational potential and satisfies Poisson's equation $\nabla^2\psi = 2\kappa$.

Since the true position $\vec{\beta}$ of the source is unknown, the deflection angle $\vec{\alpha}$ itself cannot be measured: the observable quantities are the distortions induced by the deflection, which, to first order, are described by the Jacobian matrix

$$\mathcal{A}(\vec{\theta}) \;=\; \frac{\partial\vec{\beta}}{\partial\vec{\theta}} = \left(\delta_{ij} - \frac{\partial^2\psi(\vec{\theta})}{\partial\theta_i\partial\theta_j}\right) = \begin{pmatrix} 1-\kappa-\gamma_1 & -\gamma_2 \\ -\gamma_2 & 1-\kappa+\gamma_1 \end{pmatrix} , \tag{2.15}$$

where the shear components are defined as

$$\gamma_1 = \frac{1}{2}\left(\frac{\partial^2\psi}{\partial\theta_1^2} - \frac{\partial^2\psi}{\partial\theta_2^2}\right) , \quad \gamma_2 = \frac{\partial^2\psi}{\partial\theta_1\partial\theta_2} , \tag{2.16}$$

and the convergence is related to the lensing potential through Poisson's equation,

$$\kappa = \frac{1}{2}\left(\frac{\partial^2\psi}{\partial\theta_1^2} + \frac{\partial^2\psi}{\partial\theta_2^2}\right) . \tag{2.17}$$

Eq. (2.15) shows that the convergence produces an isotropic distortion of the shape of an extended source, while the shear contribution is anisotropic.

2.5.2 Cosmological Light Deflection

As illustrated in a rather intuitive way in Fig. 2.11, any density perturbation along the line of sight contributes to deflect light rays coming from distant sources. Assuming that the perturbations are very well localised in an otherwise homogeneous and isotropic background, that the Newtonian potential of the perturbations is small, $\Phi \ll c^2$, and that the velocities are much smaller than the speed of light, the deflection angle is given by

$$\vec{\alpha}(\vec{\theta}, w) = \frac{2}{c^2}\int_0^w \mathrm{d}w' \, \frac{f_{\mathrm{K}}(w-w')}{f_{\mathrm{K}}(w)} \, \nabla_\perp\Phi[f_{\mathrm{K}}(w')\,\vec{\theta}, w'] . \tag{2.18}$$

The deflection angle is thus a weighted integral over the gradient of Φ, taken in the direction perpendicular to the line of sight: the weight is determined by a ratio of comoving angular-diameter distances, from the deflecting potential to the source, $f_{\mathrm{K}}(w-w')$, and from the observer to the source, $f_{\mathrm{K}}(w)$.

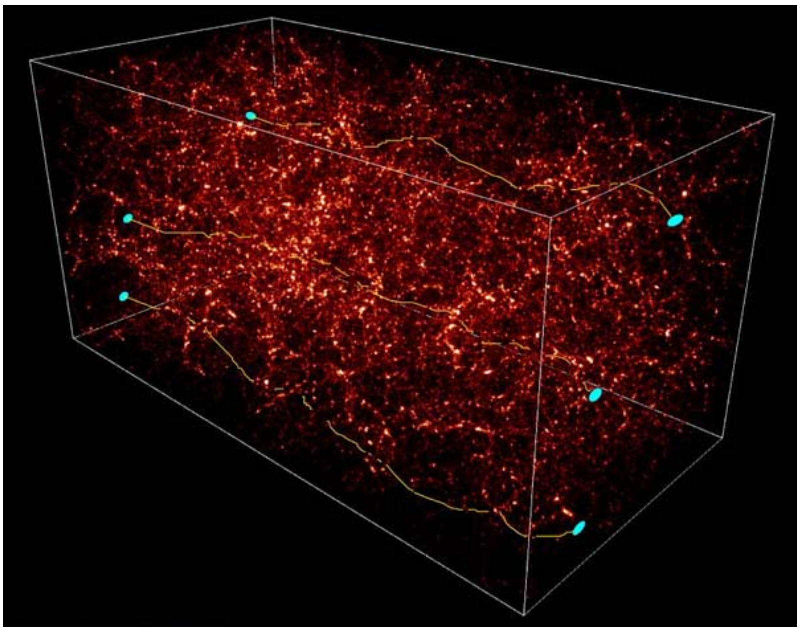

Figure 2.11: A representation of cosmic shear: the light rays coming from distant galaxies are deflected while travelling through the large-scale distribution of matter in the universe, yielding distorted images of the sources. From the NIC group at IAP.

In analogy to the thin-lens case, an effective convergence can be defined deriving the deflection angle with respect to $\vec{\theta}$. Omitting the details, the result reads

$$\kappa_{\rm eff}(\vec{\theta}) = \frac{3H_0^2\Omega_{\rm m0}}{2c^2} \int_0^{w_{\rm H}} {\rm d}w \, \bar{W}(w) \, f_{\rm K}(w) \, \frac{\delta[f_{\rm K}(w)\,\vec{\theta}, w]}{a(w)} \,, \tag{2.19}$$

where δ is the density contrast as defined in Section 1.7, and the upper integration bound, $w_{\rm H}$, stands for the horizon distance, i.e. the comoving distance to infinite redshift; in addition, the weighting function $\bar{W}(w)$ takes into account that sources are distributed in redshift:

$$\bar{W}(w) = \int_w^{w_{\rm H}} {\rm d}w' \, n(w') \, \frac{f_{\rm K}(w'-w)}{f_{\rm K}(w')} \,, \tag{2.20}$$

where $n(w){\rm d}w = n_{\rm z}(z){\rm d}z$ is the distribution function of the sources.

Although it is not possible to achieve a prediction of the light deflection relative to a particular line of sight, since the mass distribution along that light path is unknown, the statistical properties of weak lensing due to the large-scale mass distribution can be predicted from the power spectrum of the density perturbations.

Limber's equation, which relates the power spectrum of a three-dimensional field to any weighted projection of it onto two dimensions, allows to derive the convergence power spectrum $P_\kappa(l)$ in terms of the matter density power spectrum, $P_\delta(k)$:

$$P_\kappa(l) = \frac{9H_0^4\Omega_\mathrm{m}^2}{4c^4} \int_0^{w_\mathrm{H}} \mathrm{d}w \left(\frac{\bar{W}(w)}{a(w)}\right)^2 P_\delta\left(\frac{l}{f_K(w)}; w\right) \, . \tag{2.21}$$

It is worth mentioning that Limber's equation is derived assuming that the weight function varies on scales much larger than the typical scales in the considered field, and that this assumption is satisfied in this case, since $\bar{W}$ is smooth compared to δ.

Again, in analogy to the thin-lens case, the components of the shear γ can be defined, which can be estimated from the ellipticity of the sources, opposite to the convergence, which is almost impossible to quantify. It can be shown that the power spectrum of the shear is identical to that of the convergence: P_κ can thus be evaluated, if the ellipticity of distant galaxies can be measured, and its estimate can constrain the matter power spectrum P_δ.

2.5.3 Cosmic Shear Estimators

The two-point correlation function of the shear is defined as

$$\xi_\gamma(\phi) = \int \frac{l\mathrm{d}l}{2\pi} \, P_\gamma(l) \, J_0(l\phi) \, , \tag{2.22}$$

where P_γ is the shear power spectrum, and J_0 is the zero-th order Bessel function of the first kind.

The two-point correlation function of the shear can be measured from the comparison of the ellipticity of all possible pairs of galaxies separated by an angle ϕ. The separation direction is used to define the tangential and cross components of the shear, namely $\gamma_+ = \gamma \cos 2\alpha$ and $\gamma_\times = \gamma \sin 2\alpha$, where α is the angle between the above mentioned direction and the major axis of the ellipse, and the factor 2 takes into account that an ellipse is mapped onto itself by a rotation of π. The tangential and cross shear define the two correlation functions

$$\xi_{++}(\phi) = \langle\gamma_+(\theta)\gamma_+(\theta+\phi)\rangle = \frac{1}{2}\int_0^\infty \frac{l\mathrm{d}l}{2\pi} \, P_\kappa(l) \left[J_0(l\phi) + J_4(l\phi)\right] \tag{2.23}$$

and

$$\xi_{\times\times}(\phi) = \langle \gamma_\times(\theta)\gamma_\times(\theta+\phi)\rangle = \frac{1}{2}\int_0^\infty \frac{l\mathrm{d}l}{2\pi}\, P_\kappa(l)\,[J_0(l\phi) - J_4(l\phi)] \;, \tag{2.24}$$

where $J_{0,4}$ are again Bessel functions of the first kind; one can also define a mixed correlator, which is expected to vanish, $\xi_{+\times}(\phi) = 0$. The following two combinations are, though, more convenient to use: $\xi_\pm = \xi_{++} \pm \xi_{\times\times}$, which are related to the power spectrum through

$$\xi_+(\phi) = \int_0^\infty \frac{l\mathrm{d}l}{2\pi}\, P_\kappa(l)\, J_0(l\phi) \tag{2.25}$$

and

$$\xi_-(\phi) = \int_0^\infty \frac{l\mathrm{d}l}{2\pi}\, P_\kappa(l)\, J_4(l\phi) \;. \tag{2.26}$$

Other two-point statistics of cosmic shear can be derived from averaging the shear within a circular aperture and can be written in a similar form as Eqs. (2.22-2.26), i.e. as filtered versions of the convergence power spectrum. However, for cosmological purposes, the best estimator of P_κ proved to be ξ_+, which is also the one used in this work.

2.5.4 Cosmic Shear Measurements

Observations of cosmic shear are rather challenging, mainly due to the distortion being very weak. In addition, the observable quantity used to estimate the shear, namely the ellipticity of a galaxy, contains a non-negligible noise contribution: galaxies are not circular, thus the measured signal is the sum of the effect of gravitational lensing and an intrinsic ellipticity, which is unknown. In the assumption that galaxy shapes are not correlated, it is possible to average the signal over several sources, thus averaging out the intrinsic ellipticity and leaving only the shear signal. Clearly, the standard deviation of the intrinsic ellipticity distribution contributes to the errors on the estimate of the shear, along with the number of sources over which the averaging process is performed for each angular separation, which is evidently smaller for a survey which can achieve a large galaxy number density; of course, also the surveyed area is an important parameter for error estimation.

Other systematics affecting the measurement of cosmic shear are related to instrumental issues: having travelled from the source throughout the large-scale matter distribution of the universe, the light rays still have to pass through the atmosphere of the Earth, which is turbulent, and through the optics of the telescope, which might not be perfect; also the CCD which eventually detects the signal may not be flawless. All these effects, which degrade the image of the source hence the estimate of the shear signal, can be taken into account, and removed, through an accurate monitoring of the point-spread function (PSF), i.e. the response of a point-like source, typically a star, to the atmosphere-optics-detector system.

Further possible systematic effects are taken care of through a comparison of the so-called E and B-modes: since the gravitational deflection is described by second-order derivatives of a scalar potential, only curl-free (E) modes are allowed; the detection of any significant curl component (B-modes) is supposed to be due to residual systematics in the data.

2.5.5 Cosmic Shear as a Cosmological Probe

The first detection of the cosmic-shear correlation function was reported almost simultaneously by several groups (see, e.g. Bacon et al. 2000; Van Waerbeke et al. 2000), and the data were immediately used to estimate cosmological parameters. In particular, as evident from Eqs. (2.21-2.26), two-point statistics of cosmic shear are sensitive to the normalisation of the power spectrum, σ_8, and to the matter density parameter, $\Omega_{0\mathrm{m}}$: more precisely, cosmic shear constrains the product $\sigma_8\,\Omega_{0\mathrm{m}}^{\alpha}$, hence it is degenerate in these two parameters.

Ever since these first detections, a large number of cosmic-shear surveys have been realised: the most up-to-date, namely the Canada-France-Hawaii-Telescope Legacy Survey (CFHTLS), has achieved measurements of the cosmic-shear correlation function with very small error bars over a wide range in angular scales (see Hoekstra et al. 2006; Semboloni et al. 2006 for the first results). The project is still ongoing, and a recent analysis of the three-year data managed to detect the signal at very large separations, up to 230 arcmin, i.e. well into the linear regime,

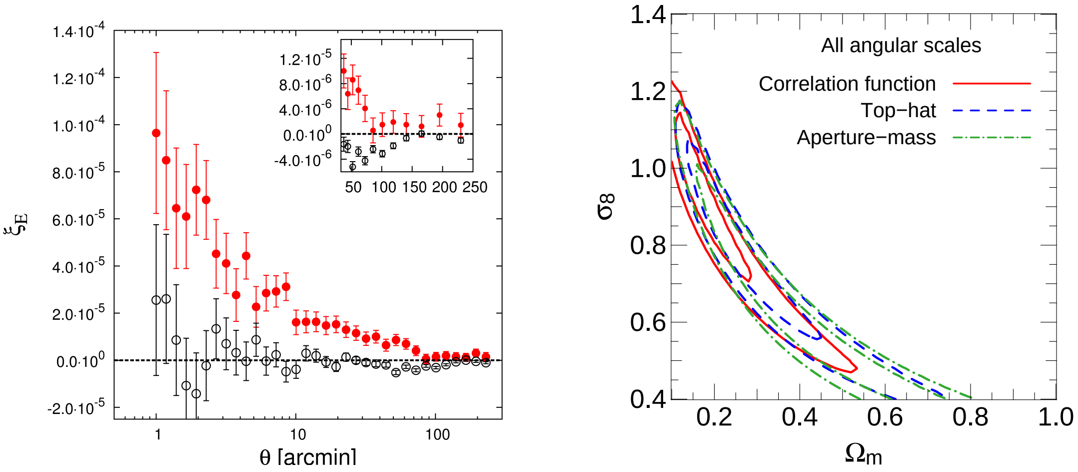

Figure 2.12: *Left panel:* The two-point correlation function from the three-year CFHTLS data: E-modes are plotted in red, and B-modes, which are compatible with zero, in black. *Right panel:* Consequent constraints on $\Omega_{0\mathrm{m}}$ and σ_8 using three different two-point statistics of the cosmic shear; the analysis assumes a flat ΛCDM model. From Fu et al. (2008).

thanks to the unprecedented width of the contiguous area of the survey (Fu et al., 2008). The two-point correlation function and the constraints in the $(\Omega_{0\mathrm{m}}, \sigma_8)$ plane, where the degeneracy is evident, are shown in Fig. 2.12.

With current and future data quality, one of the main remaining uncertainties is related to the non-linear modelling of the matter power spectrum: this is the reason why the "very weak lensing" signal detected by Fu et al. (2008) on very large scales is so promising; another issue on which cosmological inference depends crucially is the determination of the exact redshift distribution of the background sources.

The combination of cosmic shear with other cosmological probes allows to lift the aforementioned degeneracy between $\Omega_{0\mathrm{m}}$ and σ_8: in particular, a joint analysis with CMB data is extremely powerful, since the two probes yield complementary constraints. This was first pointed out by Contaldi et al. (2003), and an analogous investigation with more recent data is present also in Fu et al. (2008); both results are shown in Fig. 2.13. Combining weak lensing data with other observations also allows to test different cosmological models and to constrain the possible dynamics of dark energy: an example is the combined analysis of CFHTLS cosmic shear data

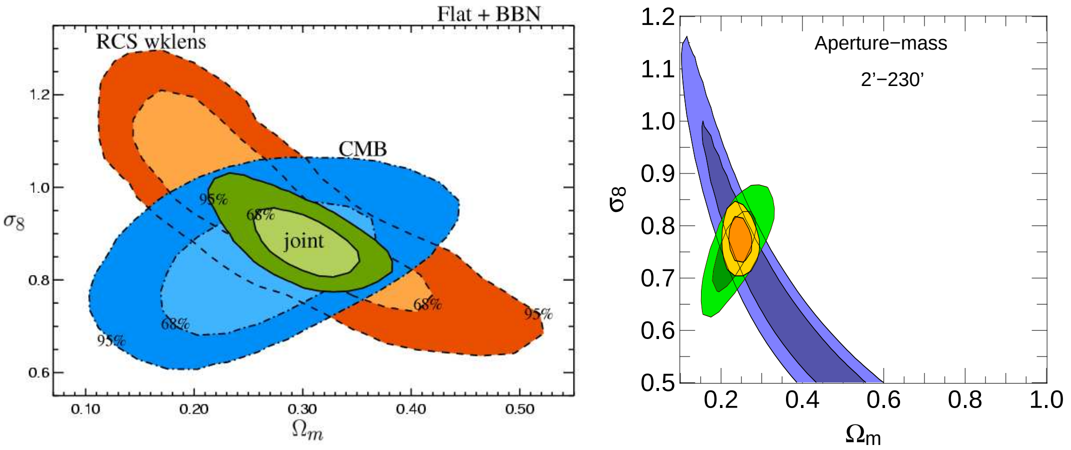

Figure 2.13: Two-dimensional likelihoods in the ($\Omega_{0\mathrm{m}}$,σ_8) plane from cosmic shear and CMB data, showing the remarkable gain in information achievable through a joint analysis. *Left panel:* the contours from cosmic shear only (data from the Red-sequence Cluster Survey) are plotted in orange, those from CMB only (data from WMAP-1, CBI and ACBAR) are plotted in blue and the joint contours are in green (Contaldi et al., 2003); *Right panel:* the contours from cosmic shear only (data from the CFHTLS) are plotted in blue, those from CMB only (data from WMAP-3) are plotted in green and the joint contours are in orange (Fu et al., 2008). Both analyses assume a flat ΛCDM model.

with galaxy clustering measurements from SDSS performed by Doré et al. (2007) in order to test alternative theories for gravity. Since the gravitational lensing signal depends not only on the intervening mass distribution, but also on the relative distances between observer, lenses and sources, it probes at the same time the expansion history and the growth of structures: the additional sensitivity to the growth factor enables to break some degeneracies that affect geometrical tests, such as type Ia supernovae or baryon acoustic oscillations, which have no power to distinguish between different models with the same expansion history.

For further details about the cosmological implications of cosmic shear, see the dedicated reviews by Van Waerbeke & Mellier (2003); Munshi et al. (2008).

Chapter 3

Solving the Cosmic Puzzle: an Alternative Approach to Dark Energy

This chapter reviews how the observational evidence for cosmic acceleration accumulated during the past decade and eventually converged towards the so-called “concordance” model for cosmology, consisting of a universe made up of dark energy and dark matter, and but a handful of ordinary, baryonic matter. The main possible theoretical scenarios to account for acceleration are briefly presented, along with some of the observational projects which are currently being developed and planned in order to solve the dark-energy puzzle. In this rather obscure context, the quest for a direct, model-independent reconstruction of the cosmic functions underlying the astronomical measurements stands out as a key approach, even more fundamental than the commonly used parametrisations, which rely on models that are still only poorly understood.

3.1 The Evidence for Acceleration

As already outlined in Chapter 2, the first evidence for cosmic acceleration dates back to a decade ago, with the compilation of large sets of distances to type-Ia supernovae (Riess et al., 1998; Perlmutter et al., 1999). These samples showed that, unexpectedly, distant supernovae appear to be fainter than their local counterparts, thus implying the occurrence of a recent phase of accelerated expansion of the universe. One of the first Hubble plots, from the Supernova Cosmology Project, is shown in Fig. 3.1; as described in the previous chapter, the significant improvements achieved in the field of supernova cosmology since these early results did nothing but confirm the original claim that cosmic expansion has been accelerating since roughly $z \sim 1$.

Along with the direct probe of acceleration coming from supernovae of type Ia, the past ten years have witnessed an outstanding convergence of several observational tests, based on very different physical mechanisms, towards the existence of an additional, unknown component with negative pressure, adding up to roughly 70% of the universe and driving the current, accelerated expansion. This indirect evidence results from a simple shortfall in the cosmic budget. Perhaps unduly simplifying the picture, the typical angular size of CMB temperature fluctuations constrains the overall spatial curvature and thus the sum of all energy density contributions, which is very close to critical (Spergel et al., 2007; Komatsu et al., 2009), whereas the the total matter density, constrained by the large-scale galaxy power spectrum (Cole et al., 2005; Percival et al., 2007b) and the evolution of galaxy clusters (Allen et al., 2003, 2004), is only a third critical: the difference between the total energy density and the matter density is attributed to the cosmological constant or the dark energy. The outstanding convergence of the latest results towards the concordance model is depicted in the top panel of Fig. 3.2, and the sketch in the bottom panel summarises what is currently believed to be the cosmic inventory.

3.2 Dark Energy and Other Scenarios

Although the evidence for the existence of a dark-energy component is almost conclusive, very little is known about its properties; furthermore, there is currently no compelling theoretical explanation for it.

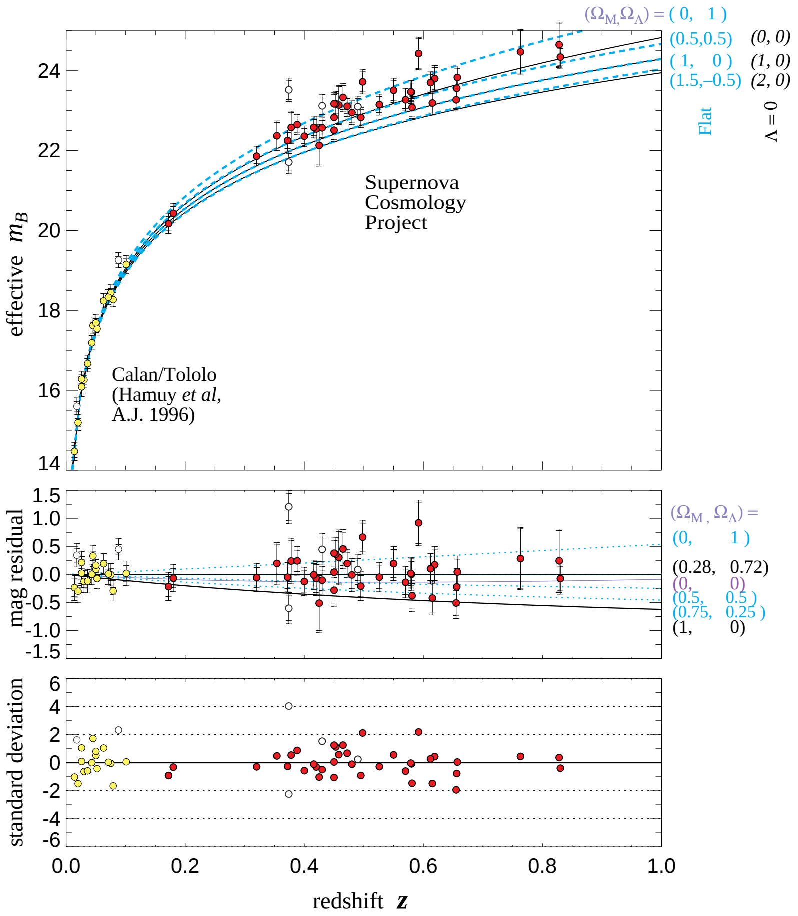

Perlmutter, *et al.* (1998)

Figure 3.1: *Top panel:* Hubble diagram for 42 high-redshift type-Ia supernovae from the Supernova Cosmology Project, and 18 low-redshift ones from the Calán/Tololo Supernova Survey. The theoretical predictions for models with different values of $\Omega_{\rm m}, \Omega_\Lambda$ are also shown. *Central panel:* magnitude residuals from the best-fit flat cosmology ($\Omega_{\rm m} = 0.28$, $\Omega_\Lambda = 0.72$); the inconsistency between the data and a flat model without a cosmological constant is evident. *Bottom panel:* uncertainty-normalised residuals from the best-fit flat cosmology. From Perlmutter et al. (1999)

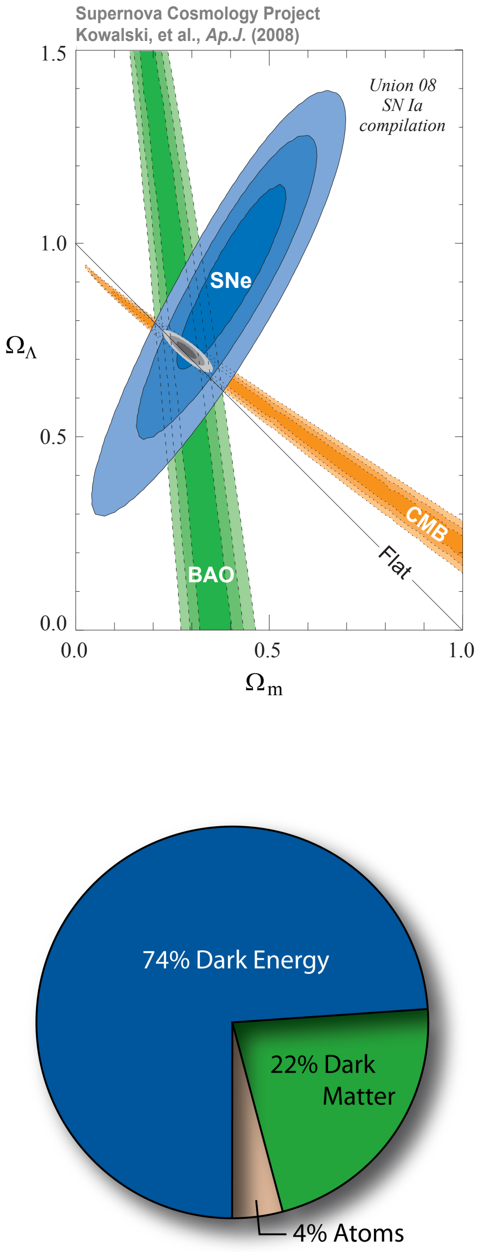

Figure 3.2: *Top panel:* Likelihood contours in the $\Omega_{\rm m}, \Omega_\Lambda$ plane: extremely tight constraints are obtained from a combination of type-Ia supernovae, baryon acoustic oscillations and the 5-year WMAP cosmic microwave background data, when the equation of state of the dark energy is fixed to be $w = -1$. From Kowalski et al. (2008). *Bottom panel:* A pie diagram illustrating the current composition of the universe, dominated by dark energy and, regarding the matter sector, by non-baryonic dark matter. From NASA/WMAP Science Team.

The simplest possibility is that the universe is permeated by an energy density which is uniform in space and constant in time: the famous cosmological constant Λ, with equation of state $w = -1$. It was originally introduced by Einstein in the field equations to allow a static solution, in an epoch when the expansion of the universe as an observational fact was still ignored; after the expansion was first detected, Einstein removed the Λ term from his theory. Decades later, the cosmological constant appeared again, to explain another "anomalous" expansion behaviour suggested by observations, namely the recent phase of acceleration. However, general arguments from particle physics predict that, if Λ is not zero, it is expected to be 120 orders of magnitude larger than what is actually measured. This delicate fine-tuning issue, along with the so-called coincidence problem, i.e. the unclear reason why, of all epochs, the cosmological constant started to dominate right "now", has triggered a rich proliferation of more exotic theoretical explanations to the dark-energy problem.

Alternatively to the cosmological constant scenario, dark energy can be explained in terms of a dynamical fluid with an equation of state $w < -1/3$, possibly time dependent, $w(a) = p(a)/\rho(a)\, c^2$, usually referred to as quintessence. Many different theories of dynamical dark energy, characterised by their differing predictions for the evolution of $w(a)$, can be derived in the context of fundamental theories. A particularly interesting candidate for quintessential dark energy is a scalar field slowly rolling down a potential, which poses strong challenges to fundamental physics from an experimental point of view.

It is worth noticing that, in the case of a time-evolving dark energy, its contribution to the expansion rate in Eq. (1.14) is no longer constant in terms of the scale factor, but evolves proportionally to a function

$$F(a) = \exp\left[-3\int_1^a (1+w(a'))\frac{da'}{a'}\right] \ , \tag{3.1}$$

which takes into account the time evolution of the equation of state. The expansion rate is thus an integrated function of $w(a)$; since almost all cosmological tests measure an integrated function of the expansion rate itself (e.g. distance measurements), the information they carry on the (possible) time evolution of the equation of state is integrated twice.

To date, no model providing a natural explanation to the fine-tuning or the coincidence problems outlined above has yet been presented: hence, there is no compelling reason to choose quintessence above the LCDM model.

Attempts to explain the recent acceleration without invoking a dark energy field have also been developed: within the framework of general relativity, either an inhomogeneous world model, with a metric different from the FLRW one, or the "back-reaction" effect from non-linear structure formation might be able to produce the observed late-time acceleration. A more radical approach to the problem of the accelerated expansion is the idea that general relativity itself breaks down on large scales. Modified gravity theories involve a modification of Einstein's field equations on the geometric side ($G_{\mu\nu}$) rather than on the matter side ($T_{\mu\nu}$): the two main classes of models are scalar-tensor theories and higher-dimensional brane-world models, both motivated in the context of string theory. For a more thorough discussion about modified gravity, see e.g. the review by Durrer & Maartens (2008).

The study of such models goes well beyond the scope of this work. It will suffice mentioning that, in modified gravity theories, the differential equation for the evolution of linear density fluctuations is no longer governed simply by Eq. (1.30): if, on one side, the expansion rate of any modified gravity model can be reproduced by a suitably chosen LCDM model, the growth rate of linear perturbation, on the other side, is able to discern between the two models. This fundamental property confirms the importance of combining different observational tests, probing both distances and the growth of structure, in order to investigate the dynamics of dark energy.

3.3 Current and Future Observational Efforts

The vast number of possibly viable models described in the previous section, ranging from the simple cosmological constant to scalar fields and modified gravity, point out the deep implications that questions about the nature of dark energy represent for fundamental physics. It is not possible, however, to attempt a conclusive answer at present: even the latest results from ground- and space-based observations are not able to decisively determine which one, amongst the many alternative models, describes at best the currently accelerating universe.

As was already pointed out, the combination of different techniques, possibly probing different physical processes and measuring both the expansion rate and the growth of structure, stands out as the main promise of the current and future observational efforts. In order to investigate the nature of dark energy, its possible time evolution and potential deviations from general relativity, the key observational tests are type-Ia supernovae, baryon acoustic oscillations, cosmic shear and galaxy clusters (see, e.g. the Dark Energy Task Force Report, Albrecht et al. 2006).

One of the main projects which are currently ongoing, targeting the issue of the nature of dark energy, is the Canada-France-Hawaii Telescope Legacy Survey (CFHTLS): its key science drivers are the monitoring of about 2000 type-Ia supernovae, i.e. the SuperNova Legacy Survey (SNLS, see Astier et al. 2006 for the first-year data release), and an exploration of the dark matter power spectrum and its evolution with redshift by means of the gravitational distortion exerted by the large scale structure on the distant galaxy population (for the first cosmic shear analysis results, see Hoekstra et al. 2006; Semboloni et al. 2006; Fu et al. 2008).

Regarding the properties and the large-scale distribution of galaxies, great success has been achieved through the completion of the two largest galaxy surveys to date, the Two-Degree Field Galaxy Redshift Survey (2dFGRS, Colless et al. 2001) and the Sloan Digital Sky Survey (SDSS, York et al. 2000). In particular, the SDSS is now entering its stage III operations, including the Baryon Oscillation Spectroscopic Survey (BOSS), a dedicated survey which will target the clustering of galaxies on large scales, mapping the BAO signature and its evolution with redshift (for more details, visit `www.sdss3.org`).

The next decade will witness an even larger effort to address the problem of dark energy from the observational point of view: huge international collaborations are planning space-based missions in order to probe the properties of dark energy and measure how cosmic expansion has changed over time. The need to go to space is motivated by different reasons for the different observational tests: cosmic shear studies need a small and stable point spread function (PSF), along with observations in infrared bands in order to achieve more accurate photometric-redshift estimations; the search for supernovae at $z > 1$ is almost impossible with ground-based telescopes, since the typical spectral feature of SiII used to identify type-Ia supernovae is redshifted into the infrared; in order to probe baryon acoustic oscillations, a large sky coverage is needed, and the possibility to observe in the infrared yields a deeper survey.

The European Space Agency (ESA) has approved the Euclid project, which joined two previously separated mission concepts, namely the Dark Universe Explorer (DUNE) and the Spectroscopic All-sky Cosmology Explorer (SPACE): the realisation of both a photometric and a spectroscopic survey will allow extreme accuracy in all the different measurements (supernovae, cosmic shear, BAO), and their combination is expected to yield a very tight estimate of the expansion and growth rate (for further details, see Refregier 2008; Cimatti et al. 2008). An analogous project planned by NASA is the Joint Dark Energy Mission (JDEM): one of its parts is SNAP, the SuperNova Acceleration Probe, a space-based observatory which should target supernovae and cosmic shear (Aldering & the SNAP collaboration, 2004). All these projects are currently undergoing preliminary design studies, and are forecasted to be launched not earlier than 2016.

Along with the ambitious space missions, several ground-based projects to be realised in the upcoming future include also dark energy amongst their science goals: the Dark Energy Survey (DES, see `www.darkenergysurvey.org`), a dedicated project which will use the CTIO telescopes in Chile, and the Large Synoptic Survey Telescope (LSST, Ivezic et al. 2008), another telescope to be built in Chile, will both target galaxy clusters, supernovae and the distribution of galaxies on large scale, in order to probe cosmic shear and the evolution of the matter power spectrum with redshift; the Square Kilometer Array (SKA, Schilizzi et al. 2008), a

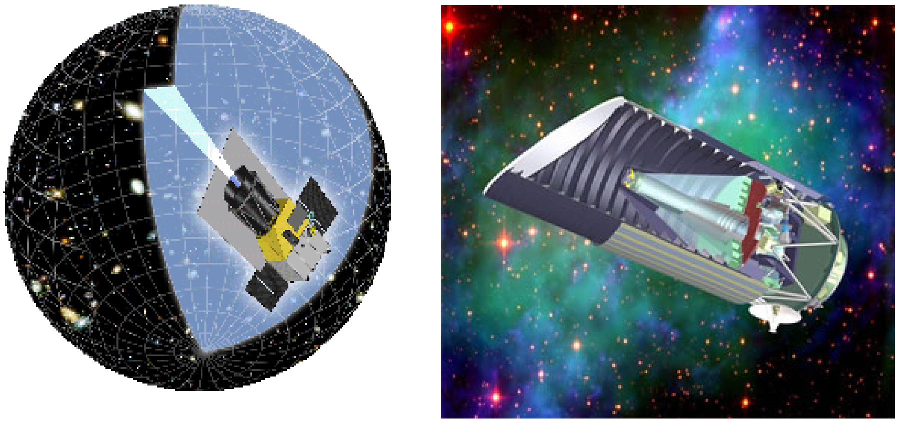

Figure 3.3: An artistic impression of the satellite observatory Euclid proposed to ESA on the left side, and of the NASA project SNAP on the right side.

future-generation radio telescope, has several science objectives spanning various areas of astrophysics, and in the context of dark energy it will yield redshift estimates for roughly one billion galaxies up to $z \sim 1.5$, allowing accurate measurements of the acoustic oscillation features in the galaxy distribution, along with a measurement of the cosmic shear distortion imprinted on radio continuum sources (Blake et al., 2004).

3.4 A Model-Independent Approach

The goal to determine the very nature of dark energy, driving the many challenging observational projects discussed in the previous section, seems to have focused all efforts uniquely on the determination of one function, namely the equation of state $w(a)$. While a detection of a more or less significant variation from -1 would clearly represent a striking discovery, this approach is not free of pitfalls.

The infinite dimensional space of dark energy models is usually compressed into a small set of parameters to characterise $w(a)$ and place it into the cosmic expansion rate in Eq. (1.14), substituting the conventional cosmological-constant term with the function $F(a)$ in Eq. (3.1). In the last years, a very popular parametrisation turned out to be

$$w(a) = w_0 + w_a(1 - a) \ , \tag{3.2}$$

where w_0 represents the current value of w and w_a takes into account its time evolution, as proposed by Chevallier & Polarski (2001) and, later, by Linder (2003).

As already pointed out, the equation of state is related via a double integration to the actually measurable quantities: distances and the growth factor depend thus only weakly on the details of $w(a)$. Regarding distance measurements, Maor et al. (2001) first described the theoretical limitation in using them to determine the value and possible time evolution of the equation of state. As shown in Fig. 3.4, the luminosity distance up to $z = 2$ is nearly identical for a set of nine different models: the central panel shows that the percentage deviation from a fiducial model with constant equation of state is less than 1%, whereas the bottom panel shows the wide range of $w(a)$ underlying the different models. If w is artificially restricted to be constant in analysis of the data, the range of models collapses to the narrow region between the dashed lines in the bottom panel, thus giving a misleading impression that $w(a)$ is well resolved. Similarly, Bassett et al. (2004) investigated the possible dangers deriving from the compression of the dark energy space into low-dimensional subspaces: they concluded that standard one- and two-parameter compressions are prone to yield misleading results, particularly regarding the possibility of rapid evolution in $w(a)$, which they cannot follow; this suggests to consider additional higher-order terms, although an extension of the parameter space may lead to severe degeneracies, making the parametrisation unable to constrain the space of dark energy models.

Reconstructing $w(a)$ is doubtlessly reasonable when testing specific dark-energy models; however, especially in sight of the above mentioned pitfalls and limitations, the question remains interesting what can be inferred on the cosmic expansion rate $H(a)$ from observations without any reference to a specific model for the energy content of the universe and how it may affect cosmic dynamics.

This work follows the latter approach. As it was stressed in the previous chapters,

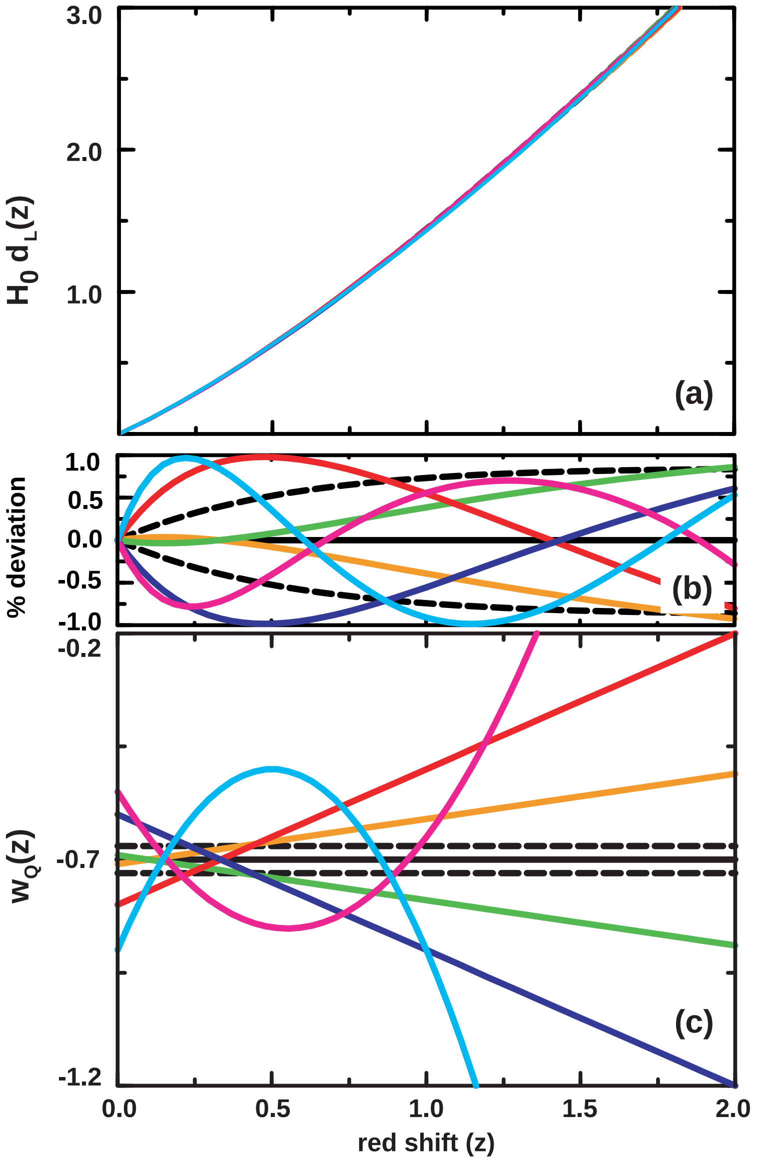

Figure 3.4: The dependence of the luminosity distance on a double integration over the equation of state $w(z)$: the *top panel* shows the luminosity distance for nine choices of the dark-energy equation of state, whose evolution in redshift is shown in the *bottom panel*; the *central panel* shows the percentage deviation from a fiducial model with constant $w = -0.7$. From Maor et al. (2001).

the expansion function is the central mathematical object underlying all cosmological measurements, augmented by the assumption of local Newtonian dynamics if structure growth in the late universe is to be included. This suggests that measurements of the function $H(a)$ itself, without any reference to Friedmann models, should be possible and much more fundamental than the common constraints of cosmological parameters entering the expansion function once the density contributions to the Friedmann models are specified.

The importance of a model-independent reconstruction of the cosmic expansion rate from luminosity distance data has been largely discussed in the literature. The possibility of reconstructing the potential of dark-energy from $H(a)$ or $\delta(a)$ was first pointed out by Starobinsky (1998), where the relations between the observational data and the expansion rate are presented. Several different techniques have been developed since then to appropriately treat the data in order to perform such a reconstruction (see, e.g., Huterer & Turner 1999, 2000; Tegmark 2002; Wang & Tegmark 2005), all of them employing a smoothing procedure in redshift bins; an example of these results is shown in Fig. 3.5. Also principal component analysis (PCA) has been used to reconstruct the dark energy equation of state as a function of redshift (see, e.g., Huterer & Starkman 2003; Crittenden & Pogosian 2005; Simpson & Bridle 2006).

As already pointed out in Sect. (1.7), from the expansion rate the growth rate of linear density fluctuations can be inferred: besides a model-independent reconstruction of $H(a)$, this work presents the resulting constraints on $D_+(a)$ as well. This is particularly interesting in sight of future missions, like Euclid, which are expected to constrain the growth rate tightly: a comparison of a direct measurement of $D_+(a)$ with its reconstruction obtained from the expansion rate could shed light on issues concerning the dynamics of dark energy.

Parallel to this work, similar attempts employing different techniques have been developed elsewhere: it is worth mentioning that a non-parametric reconstruction

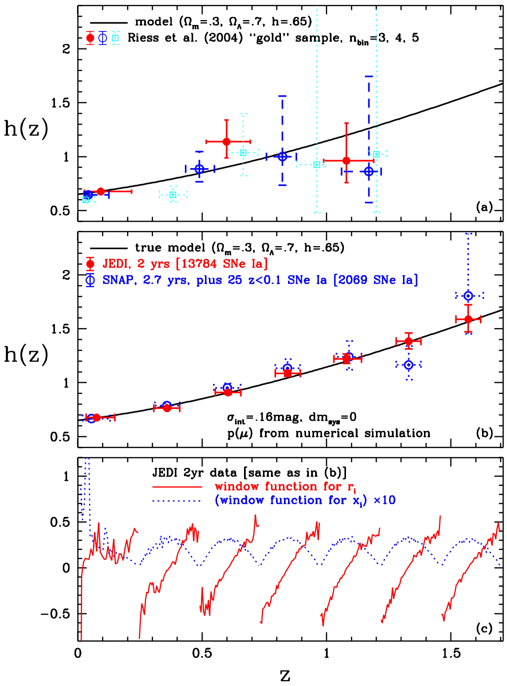

Figure 3.5: The expansion rate reconstructed in uncorrelated redshift bins from supernova data, using current (*top panel*) and future (*central panel*) samples; the window functions employed for the reconstruction in each bin are also shown (*bottom panel*). From Wang & Tegmark (2005).

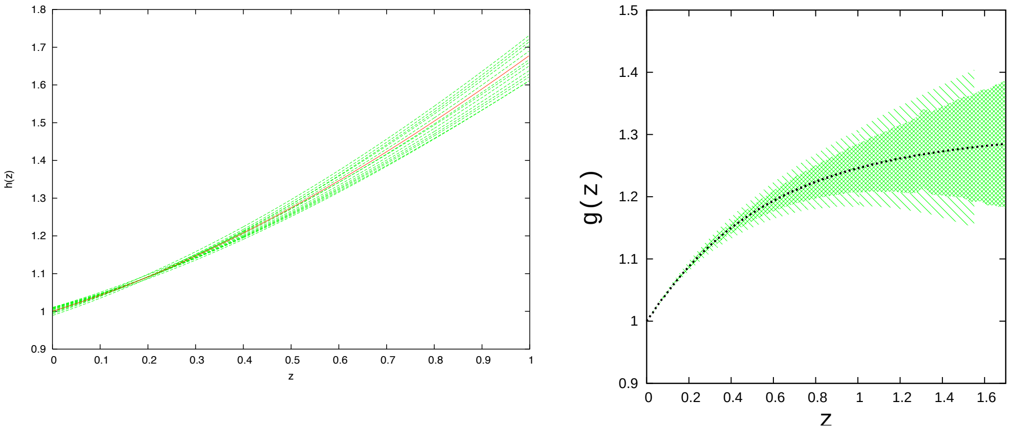

Figure 3.6: *Left panel:* An example of the expansion rate reconstruction from distance to type-Ia supernovae, using the SNLS sample. From Shafieloo (2007). *Right panel:* The growth factor reconstructed from supernova and baryon acoustic oscillation data, for a synthetic LCDM model with current (dashed area) and future (hatched area) observational standards. From Alam et al. (2008).

algorithm, which recovers the expansion function from distance data, has been developed in Shafieloo et al. (2006) and Shafieloo (2007), making use of data smoothing over redshift with Gaussian kernels, and it has been generalised by Alam et al. (2008) to reconstruct the growth rate from the estimated expansion rate. Their results are summarised in Fig. 3.6.

Chapter 4

Model-Independent Reconstruction of the Expansion Rate Using Type-Ia Supernovae

This chapter introduces the reconstruction technique that has been developed in the course of this work, in order to achieve an estimate of the expansion rate from luminosity distance data without any reference to a particular model for the dark energy. The details of the method and the assumptions it relies on are presented, along with its performance on synthetic and real type-Ia supernova data. The results presented in this chapter have been published in Mignone & Bartelmann (2008).

4.1 A Model-Independent Approach to the Expansion Rate

If space-time is on average homogeneous and isotropic and topologically simply connected, it must be described by a Robertson-Walker metric characterised by a time-dependent scale factor $a(t)$, as described in Eqs. (1.2) and (1.3). General relativity enters when the scale factor is to be related to the energy content of the universe. However, the geometry of space-time, in particular the distance measures, are determined already once the scale factor and its first derivative are specified by the expansion function $H(a)$.

Instead of specifying a particular Friedmann model and constraining the parameters contained in $H(a)$ as outlined in Eq. (1.14) and its possible generalisation to quintessence models, shown in Eq. (3.1), the goal of this work is to recover the expansion rate of the universe, $H(a)$, as a function of the scale factor a, without assuming any specific parameterisation for it. For simplicity of notation, the curvature parameter is put $K = 0$, hence the comoving angular-diameter distance coincides with the comoving distance, i.e. $f_K(\chi) = \chi$, according to Eq. (1.3); this is a first-order approximation even in the case of small $K \neq 0$. This simplification could be dropped if necessary without any change of principle.

Recalling Eq. (1.19), the comoving distance between an observer at the present epoch and an astronomical source, identified by a value a of the scale factor, reads

$$\chi(a) = \frac{c}{H_0} \int_a^1 \frac{\mathrm{d}a'}{a'^2 E(a')} \; ; \tag{4.1}$$

due to Etherington's relation, presented in Eq. (1.24), the luminosity distance, in the case of $K = 0$, can be written as

$$D_\mathrm{L}(a) = \frac{c}{H_0} \frac{1}{a} \int_a^1 \frac{\mathrm{d}x}{x^2 E(x)} \equiv \frac{c}{H_0} \frac{1}{a} \int_a^1 \frac{\mathrm{d}x}{x^2} e(x) \; , \tag{4.2}$$

where the inverse expansion rate $e(a) \equiv E^{-1}(a)$ has been defined. For the sake of simplicity, the normalising Hubble length c/H_0 is dropped in the following discussion, thus scaling the luminosity distance by the Hubble length.

Differentiating Eq. (4.2) with respect to a, and dropping c/H_0, the following relation is obtained,

$$D'_\mathrm{L}(a) = -\frac{1}{a^2} \int_a^1 \frac{\mathrm{d}x}{x^2} e(x) - \frac{e(a)}{a^3} \; , \tag{4.3}$$

which can be brought into the generic form of a Volterra integral equation of the second kind for the unknown function $e(a)$,

$$e(a) = -a^3 D'_\mathrm{L}(a) + \lambda \int_1^a \frac{\mathrm{d}x}{x^2} e(x) \; , \tag{4.4}$$

with the inhomogeneity $f(a) \equiv -a^3 D'_{\mathrm{L}}(a)$ and the simple kernel $K(a,x) = x^{-2}$. The general parameter λ will later be specialised to $\lambda = a$. As detailed e.g. in Arfken & Weber (2005), Eq. (4.4) can be solved in terms of a Neumann series,

$$e(a) = \sum_{i=0}^{\infty} \lambda^i e_i(a) \; , \tag{4.5}$$

where a possible (but not mandatory) choice for the functions e_i is

$$e_0(a) = f(a) \; , \quad e_n(a) = \int_1^a K(a,t) e_{n-1}(t) \mathrm{d}t \; . \tag{4.6}$$

The first guess for $e_0(a)$ is equivalent to say that the integral or the parameter λ in Eq. (4.4) is small. This crude approximation, which is valid in all relevant cosmological cases, is then improved iteratively until convergence is achieved.

4.2 Application to Type-Ia Supernovae

As explained in Section 2.1, after application of the empirical relation between light-curve width and luminosity, observations of type-Ia supernovae yield measurements of the distance moduli μ_i and redshifts z_i for a set of N objects, which can be converted into a set of luminosity distances $D_{\mathrm{L}}(a_i)$ dependent on the scale factors $a_i = (1 + z_i)^{-1}$.

The model-independent technique outlined in the previous section requires taking the derivative of the luminosity distance with respect to the scale factor, as evident from Eq. (4.3). Due to measurement errors and scatter of the data about the fiducial model, it is not feasible to directly differentiate the luminosity distance data, since the result would be extremely noisy and any estimate of $D'_{\mathrm{L}}(a)$ unreliable. Thus, the data need to be appropriately smoothed. It is here proposed to do so by fitting a suitable function $D_{\mathrm{L}}(a)$ to the measurements $D_{\mathrm{L}}(a_i)$ and approximating the derivative in Eq. (4.4) by the derivative of $D_{\mathrm{L}}(a)$. This choice is justified under the assumption that the derivative of the fitted data is in fact a good representation of the actual derivative of the data.

For doing this in a model-independent way, it is convenient to expand $D_{\rm L}(a)$ into a series of suitably chosen orthonormal functions $p_j(a)$,

$$D_{\rm L}(a) = \sum_{j=0}^{M-1} c_j p_j(a) \; . \tag{4.7}$$

The M coefficients c_j in Eq. (4.7) are estimated via minimisation of the χ^2 function

$$\chi^2 = \left(\vec{D}_{\rm obs} - \bar{D}(\vec{a})\right)^T C^{-1} \left(\vec{D}_{\rm obs} - \bar{D}(\vec{a})\right) \; , \tag{4.8}$$

where $\vec{D}_{\rm obs}$ is a vector containing the N measured luminosity distances, $\vec{a}$ is a vector of the measured scale factors, and

$$\bar{D}(a_i) \equiv \sum_{j=0}^{M-1} c_j p_j(a_i) \equiv (P\vec{c})_i \tag{4.9}$$

is the vector of model luminosity distances to the scale factors $\vec{a}$.

In the final expression of Eq. (4.9), P is an $N \times M$ matrix with elements $P_{ij} \equiv p_j(a_i)$, and $\vec{c}$ is the M-dimensional vector of expansion coefficients. Using the fact that the covariance matrix C^{-1} is symmetric, the set of coefficients minimising χ^2 is

$$\vec{c} = \left(P^T C^{-1} P\right)^{-1} \left(P^T C^{-1}\right) \vec{D}_{\rm obs} \; . \tag{4.10}$$

In this representation of the data, the derivative of the luminosity-distance function is simply given by

$$D'_{\rm L}(a) = \sum_{j=0}^{M-1} c_j p'_j(a) \; , \tag{4.11}$$

thus avoiding the noise which would be introduced by a direct differentiation of the data.

Using the linearity of the integral equation (4.4), it can be solved for each mode j of the orthonormal function set separately. Inserting the derivative of a single basis function $p'_j(a)$ in place of $D'_{\rm L}(a)$ in Eq. (4.4), its contribution to the solution is given in terms of the Neumann series

$$e^{(j)}(a) = \sum_{k=0}^{\infty} a^k e_k^{(j)}(a) \; , \tag{4.12}$$

with

$$e_0^{(j)}(a) \equiv -a^3 p_j'(a) \;, \quad e_n^{(j)}(a) = \int_1^a e_{n-1}^{(j)}(x) x^{-2} \mathrm{d}x \tag{4.13}$$

according to Eq. (4.6). These modes of the inverse expansion function can be computed once and for all for any given orthonormal function set $\{p_j(a)\}$. Due to the linearity of the problem, the final solution is then given by

$$e(a) = \sum_{j=0}^{M-1} c_j e^{(j)}(a) \;. \tag{4.14}$$

4.3 Error Analysis

It is now explained how the errors on the supernova distance measurements propagate into the expansion coefficients c_j and eventually into the expansion rate. The Fisher matrix of the χ^2 function given in Eq. (4.8) reads

$$F_{ij} \equiv \left\langle \frac{\partial^2 \chi^2}{\partial c_i \partial c_j} \right\rangle \;, \tag{4.15}$$

which is, in this particular case, given by

$$F_{ij} = \sum_{k=0}^{N} \frac{p_i(a_k) p_j(a_k)}{\sigma_k^2} \;, \tag{4.16}$$

where k runs over all supernova measurements and the σ_k^2 are the individual errors on the luminosity distances. By the Cramér-Rao inequality, the errors Δc_i satisfy

$$(\Delta c_i)^2 \geq (F^{-1})_{ii} \;. \tag{4.17}$$

These errors will propagate into the estimate $e(a)$ of the (inverse) expansion function given in Eq. (4.14),

$$[\Delta e(a)]^2 = \sum_{j=0}^{M-1} \left[\frac{\partial e(a)}{\partial c_j}\right]^2 (\Delta c_j)^2 = \sum_{j=0}^{M-1} \left[e^{(j)}(a)\right]^2 (\Delta c_j)^2 \;. \tag{4.18}$$

Since the expansion rate is $E(a) = 1/e(a)$, its error is finally given by

$$[\Delta E(a)]^2 = \frac{[\Delta e(a)]^2}{e^4(a)} \;. \tag{4.19}$$

4.4 Application to Synthetic Data Sets

In this section, it is demonstrated using synthetic data sets how the method performs in two different model cosmologies, an Einstein-de Sitter and a standard ΛCDM model, using simulated samples with the characteristics of both current and future surveys.

4.4.1 Illustration: Einstein-de Sitter Model

In order to illustrate the proposed method in detail, a simple and unrealistic model cosmology is employed, i.e. an Einstein-de Sitter universe with matter-density parameter $\Omega_{\mathrm{m0}} = 1$, vanishing cosmological constant $\Omega_\Lambda = 0$ and Hubble constant $h = 0.7$. The expansion function is

$$E(a) = a^{-3/2} \,, \quad e(a) = a^{3/2} \,, \tag{4.20}$$

and the luminosity distance is simply

$$D_{\mathrm{L}}(a) = \frac{2}{a}(1 - \sqrt{a}) \tag{4.21}$$

in units of the Hubble radius c/H_0. A suitable choice for the orthonormal function set could start from the linearly independent set

$$u_j(x) = x^{j/2-1} \,, \tag{4.22}$$

which can be orthonormalised by the usual Gram-Schmidt procedure. The orthonormalisation interval should be $[a_{\mathrm{min}}, 1]$, where $a_{\mathrm{min}} = (1 + z_{\mathrm{max}})^{-1}$ is the scale factor of the maximum redshift z_{max} in the supernova sample: a set of orthonormal functions, $\{p_j(a)\}$, is thus obtained. Projecting the distance in Eq. (4.21) onto the basis functions, it is straightforward to see that only the first two modes p_0 and p_1 have non-vanishing coefficients. The derivatives of p_0 and p_1 are then used to construct the corresponding Neumann series following Eq. (4.13), and from them the (inverse) expansion rate can be recovered. Further details are presented in the last section of this chapter.

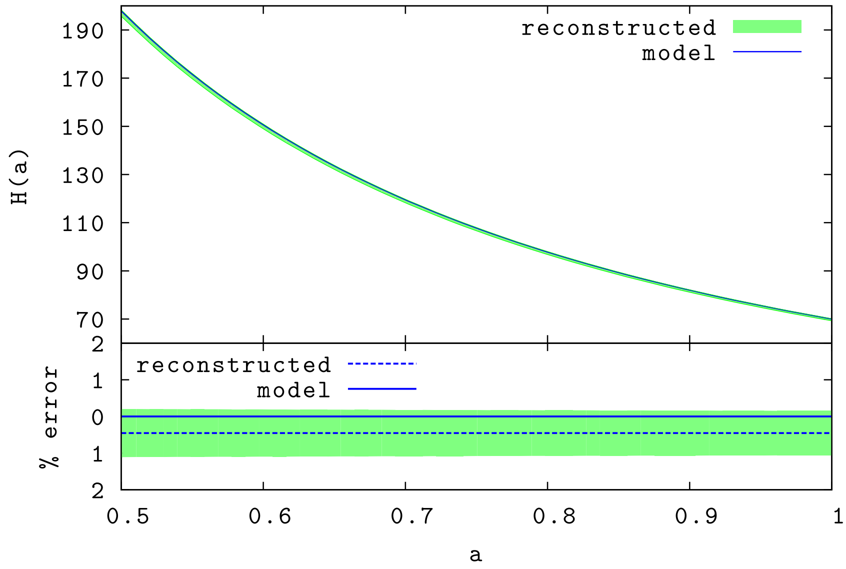

Figure 4.1: The reconstructed expansion rate for a simulated sample of supernovae in an Einstein-de Sitter universe. The observational characteristics of the sample resemble those of the first-year SNLS data. The green shaded area represents the reconstruction with 1-σ errors thereof, the blue curve represents the model. The bottom plot shows the residuals between the reconstruction and the model.

The procedure described above has been applied to a synthetic sample of type-Ia supernovae in the Einstein-de Sitter universe. The observational characteristics of the sample, such as its size, the redshifts and the distribution of typical errors of individual measurements, are adapted to those of the first-year SNLS data (Astier et al., 2006). Thus, the synthetic sample consists of 120 supernovae up to redshift $z = 1$. It enables one to determine the expansion coefficients c_0 and c_1 with relative errors of order (1-2)%. The reconstructed expansion rate $H(a)$ is shown in Fig.4.1.

The purpose of this simplified example is to show that it is possible to achieve a robust and highly accurate reconstruction of $E(a)$ when the relevant expansion coefficients can be obtained from the data with suitable significance.

4.4.2 ΛCDM model

The preceding analysis is now repeated in a more realistic case, namely with a synthetic sample simulated in a standard ΛCDM universe with $\Omega_{\rm m0} = 0.3$, $\Omega_{\Lambda 0} = 0.7$ and $h = 0.7$. The expansion function is

$$E(a) = \left(\Omega_{\rm m0} a^{-3} + \Omega_{\Lambda 0}\right)^{1/2} \ . \tag{4.23}$$

In this case the first two modes of the basis $\{p_j(a)\}$ chosen before are insufficient to reproduce $D_{\rm L}(a)$ accurately. Calculating the *true* coefficients of the expansion of $D_{\rm L}(a)$, which are obtained by projecting it onto the different basis functions, it is evident that at least the first five coefficients are significantly different from zero. This is illustrated in Fig. 4.2, where the model luminosity distance to its reconstruction using the basis functions and the *true* coefficient of its expansion are compared. If only three or four coefficients are included, the reconstruction deviates significantly from the model even at low redshift.

However, the measurement errors on the data play a crucial role in this analysis. With current standard data sets, only the first three coefficients can be determined significantly, while more than just three are needed to achieve an accurate reconstruction with the proposed basis functions. The reconstructed expansion function, obtained including three coefficients, is shown in the top panel of Fig. 4.3, where it is compared to the expansion rate of the underlying cosmological model. If only the first three modes are considered, *all* the coefficients are statistically significant, although it is known from the theoretical model that the reconstruction is incomplete. The errors on the first two coefficients c_0 and c_1 are of order (1-2)%, increasing to 8% on c_2. The errors on higher-order coefficients are larger than the coefficients themselves, indicating that they become compatible with zero and should therefore be excluded from the reconstruction.

The precision with which coefficients can be determined from the data is likely to improve dramatically with future generation, space-based supernova surveys such as the SNAP mission (Aldering & the SNAP collaboration, 2004), which is expected to measure high-quality light curves and spectra for ≈ 2000 type-Ia supernovae in

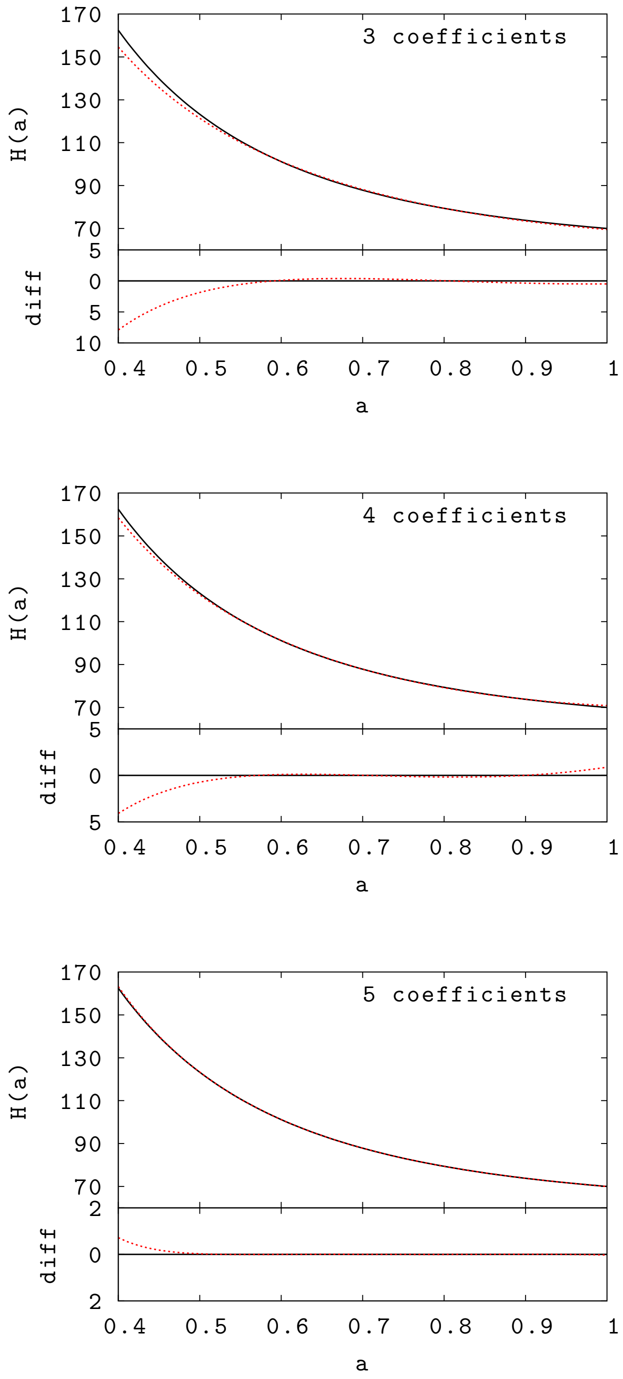

Figure 4.2: The expansion rate in a ΛCDM model with $\Omega_{\rm m0} = 0.3$ and $\Omega_\Lambda = 0.7$ (solid line) and its reconstruction obtained using the *true* coefficients (dashed line), truncated up to the third (*top panel*), fourth (*central panel*) and fifth (*bottom panel*) coefficient, respectively. The difference between the reconstruction and the model is shown in the bottom panels. When the fifth coefficient is included, the two curves nearly coincide up to $a = 0.4$.

the redshift range $0.1 < z < 1.7$. With data of such high quality it will become possible to achieve an extremely accurate reconstruction of the expansion rate with this method. As discussed above, at least five coefficients are needed in order to reconstruct the expansion rate of an underlying ΛCDM model with the set of functions described above.

Following the expected SNAP redshift distribution reported in Shafieloo et al. (2006), a synthetic data set with SNAP characteristics has been produced. As done in Shafieloo et al. (2006), also 25 more supernovae with $z < 0.1$ have been added, which are supposed to be observed by future low-redshift supernova experiments. Applying this reconstruction technique, the first five coefficients are significantly constrained, with errors on the first two coefficients being of order 0.1%. The result, obtained using five coefficients, is shown in the bottom panel of Fig. 4.3 together with 1-σ errors.

The choice of the orthonormal function set is in general arbitrary. Obviously, for each underlying model there will be a preferred function set, in the sense that the number of coefficients required to reproduce the expansion rate is minimal when using such a set. It is certainly possible to find a more suitable function set for the ΛCDM model, but since the ultimate goal of this work is to reconstruct the expansion rate from the observed data introducing as little theoretical prejudice as possible, finding the most suitable function set to reproduce the ΛCDM expansion rate is not the primary interest of this analysis. Hence, all the results presented in this Chapter made use of the basis described in Sect. 4.4.1; a possible refinement of the method, employing principal component analysis, is presented in Chapter 6.

4.4.3 Convergence of the Neumann Series

A separate, but related issue is to what power of the parameter λ the Neumann series has to be followed, or, equivalently, to what power k of the scale factor a the expansion in Eq. (4.12) has to proceed. The truncation criterion must again be based on the quality of the data. Convergence of the series is achieved at different powers k for different redshift intervals. In order to achieve convergence on the

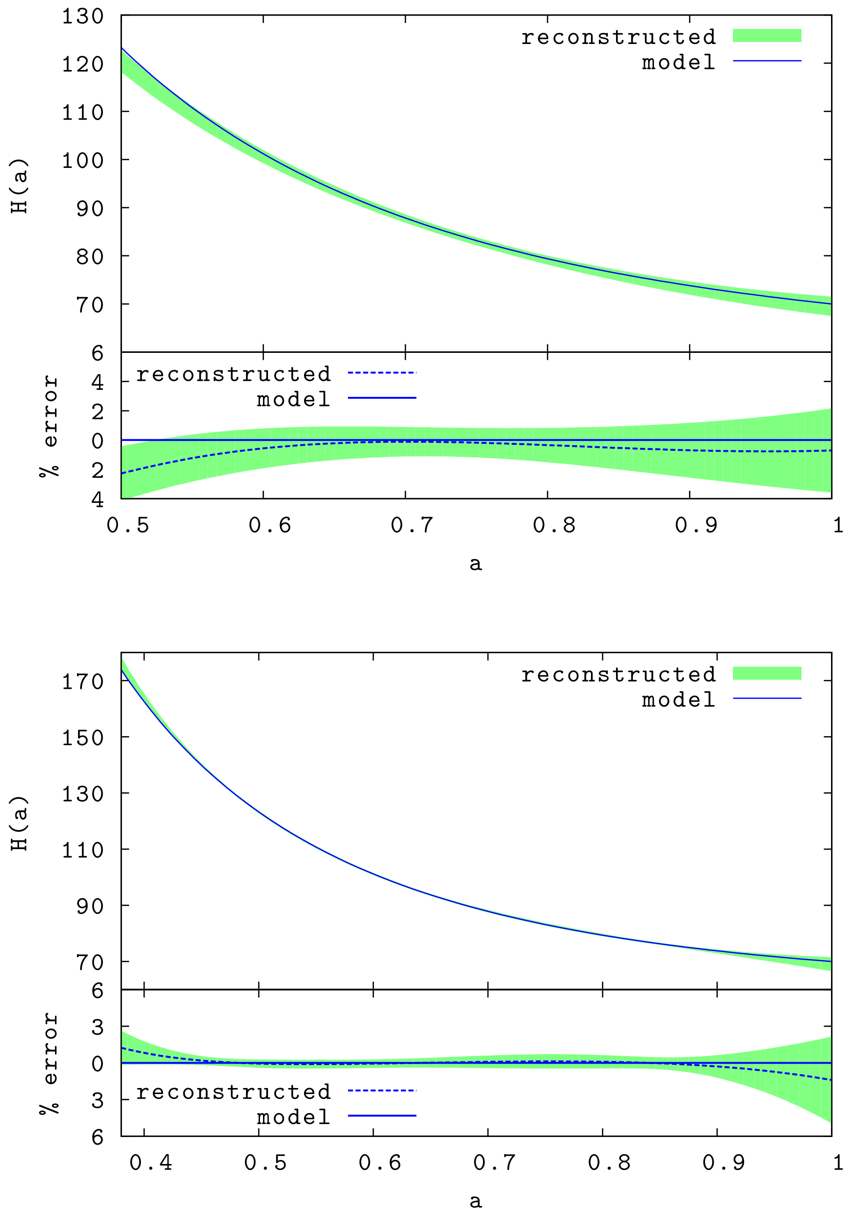

Figure 4.3: The reconstructed expansion rate for a simulated sample of supernovae in a ΛCDM universe with observational characteristics resembling those of two different surveys, namely the first-year SNLS data (*top panel*; three coefficients used), and the forecast SNAP experiment (*bottom panel*; five coefficients used), respectively. The green shaded area represents the reconstruction with 1-σ errors thereof, the blue curve represents the model. The bottom plot shows the residuals between the reconstruction and the model.

interval $0.5 \leq a \leq 1$, the series can be truncated after $k = 4$. However, the inclusion of a fourth-order term produces a difference to the preceding three orders which is already within the error bars, and can therefore be neglected. This trend is clearly enhanced when more coefficients are included in the reconstruction, since in this case the errors are larger.

4.5 Recovery of Sudden Transitions in the Expansion Rate

As emphasised above, this method can obtain the expansion function $E(a)$, or rather its reciprocal $e(a)$, based on a representation of the derivative of the measured data. It is here argued that dealing with the derivative of luminosity distance data is not expected to cause a major problem, based on the reasonable assumption that the luminosity distance is a very smooth function. As it is evident from Eq. (4.2), $D_{\mathrm{L}}(a)$ is related to the expansion function via an integral. Hence, even if $E(a)$ had a peculiar feature at some intermediate redshift, this would be smoothed out by the integration.

The issue is addressed by means of a toy model where the expansion function has indeed a sudden transition. The toy model has been constructed starting from the expansion rate of the Einstein-de Sitter model and deforming it by a gentle jump at some intermediate value a_* of the scale factor,

$$E(a) = \begin{cases} -\arctan\left[\gamma\left(a - a_*\right)\right] + \delta & (a > \tilde{a}) \\ a^{-3/2} + 1 & (a \leq \tilde{a})\ . \end{cases} \tag{4.24}$$

Using Eq. (4.2), the corresponding luminosity distance has been obtained, which is quite smooth and deviates from its Einstein-de Sitter counterpart in a way depending on a_*. The expansion rate and the luminosity distance of this toy model are plotted in Fig. 4.4, compared to those of the Einstein-de Sitter model.

Again, a synthetic sample of type-Ia supernovae within this model has been produced, with the same observational characteristics of either SNLS or SNAP, and the

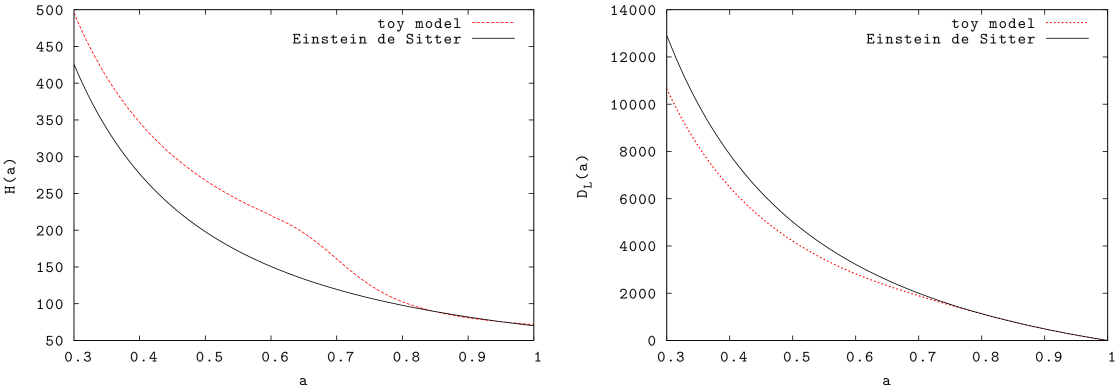

Figure 4.4: The expansion rate of the toy model compared to the Einstein-de Sitter one (*left panel*), and the corresponding luminosity distance (*right panel*). The parameters for the toy model are: $a_* = 0.7$, $\tilde{a} = 0.6$, $\gamma = 11$, $\delta = 2.3$.

reconstruction procedure applied to it. In order to reproduce the transition feature, more than three coefficients are needed. This is not feasible with SNLS-like data because coefficients beyond the third lose significance. With a SNAP-like sample instead, the expansion rate can be recovered. The results obtained with both synthetic samples, with three coefficients for the SNLS and six for the SNAP case, are shown in Fig. 4.5 together with their 3-σ errors. Figure 4.5 shows that this method can also recover expansion histories with unexpected transitions, even though the reconstruction is less accurate than that of a perfectly smooth expansion rate.

An attempt to fit this sample to a flat ΛCDM model and explore the parameter space spanned by $\Omega_{\mathrm{m}0}$ and w has also been carried out. The dark-energy equation-of-state parameter w is allowed to differ from -1, first assuming that it is constant in redshift and then parameterising its time evolution according to the parametrisation mentioned in Eq. (3.2), namely $w(a) = w_0 + w_a(1 - a)$. All the models considered are found to be capable of producing good fits to the luminosity distance data, but they all fail to reproduce the underlying expansion rate when the best fit parameters are inserted back into Eq. (1.14). In most cases, the likelihood has more than one maximum, since different combinations of the considered parameters constrain the two different branches of the expansion rate. Unless the time evolution of the dark-energy equation-of-state is modelled *ad hoc*, it is very unlikely to reproduce the

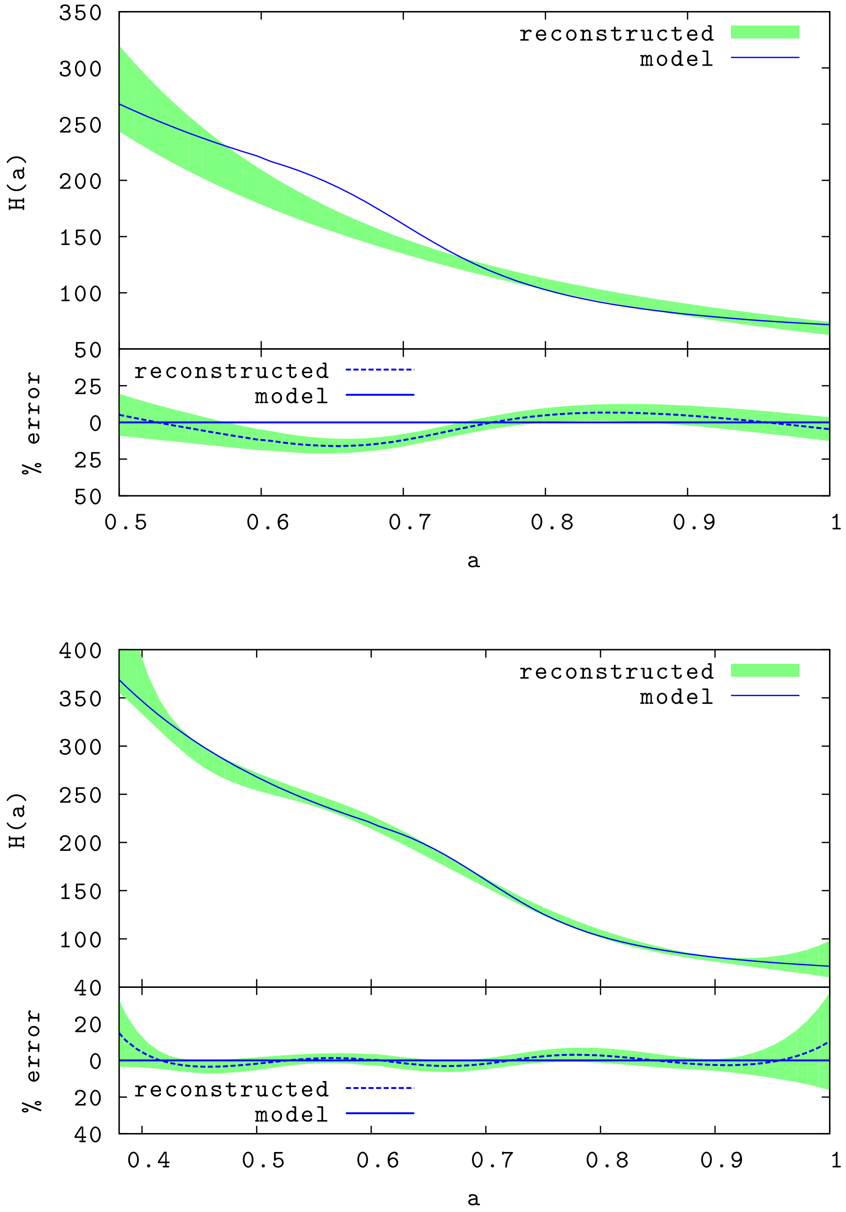

Figure 4.5: The expansion rate of the toy model (blue curve) and its reconstruction, with 3-σ errors thereof (green shaded area), obtained from a SNLS-like data set with three coefficients (*top panel*), and from a SNAP-like data set with six coefficients (*bottom panel*). The bottom plots show the residuals between the reconstruction and the model.

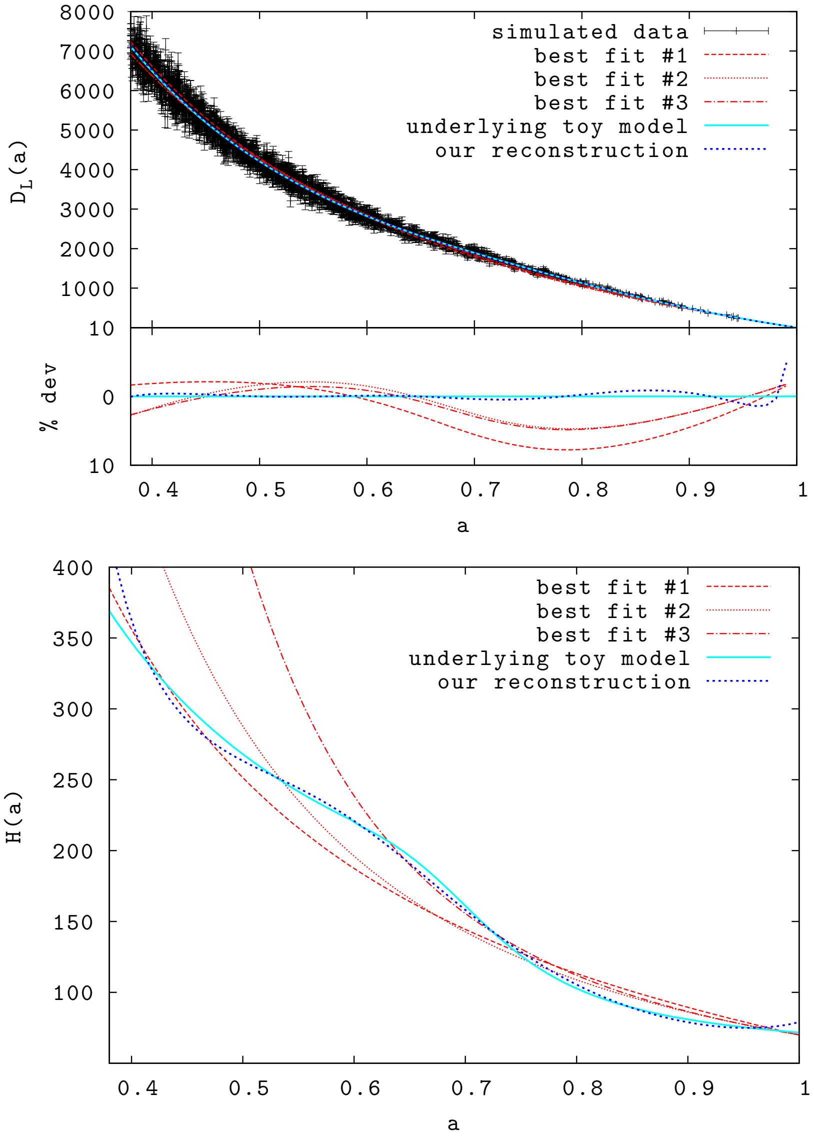

Figure 4.6: *Top panel:* The luminosity distance of the toy model (cyan curve) together with the SNAP-like simulated sample (black points), compared to the model-independent fit (blue dashed curve) and three other cosmological fits (red curves). The bottom plot shows the residuals between the different fits and the model. *Bottom panel:* The expansion rate of the toy model, of the model-independent reconstruction and of the other models. The different red curves correspond to three different fits to a flat ΛCDM: in case #1 (red dashed curve) it is imposed $w = -1$ only Ω_{m0} is allowed to vary, in case #2 (red dotted curve) both Ω_{m0} and w (constant in redshift) are allowed to vary, and in model #3 Ω_{m0}, w_0 and w_a are allowed to vary, according to Eq. (3.2).

sudden feature of the toy model in this way. However, the method developed in this work achieves this because the parameters involved in the fit trace the relation the between luminosity distance and the expansion rate. The different results obtained with the usual approach and this method for the fit to the luminosity distance and for the expansion rate are displayed in Fig. (4.6).

4.6 Application to Real Data: the First-Year SNLS

The method was finally applied to the first-year SNLS data (Astier et al., 2006). The sample consists of 71 new supernovae observed from the ground with the Canada-France-Hawaii Telescope, the farthest being at redshift $z = 1.01$, plus 44 nearby supernovae taken from the literature. Thus, the total sample contains 115 supernovae in the redshift range $0.015 < z < 1.01$.

Assuming a flat, ΛCDM universe with constant $w = -1$, Astier et al. (2006) obtained a best fit of $\Omega_{\mathrm{m0}} = 0.263 \pm 0.037$. Releasing the flatness assumption and adding constraints from the baryon acoustic oscillations (BAO) measured in the SDSS (Eisenstein et al., 2005), they obtained $\Omega_{\mathrm{m0}} = 0.271 \pm 0.020$ and $\Omega_{\Lambda 0} = 0.751 \pm 0.082$. Furthermore, they investigated models with constant equation of state $w \neq -1$: assuming flatness and the BAO constraints, their best-fit parameters are $\Omega_{\mathrm{m0}} = 0.271 \pm 0.021$ and $w = -1.023 \pm 0.087$.

The fit to the luminosity-distance data obtained applying the model-independent method to this sample, with the orthonormal function set described in Sect. 4.4.1, is shown in the top panel of Fig. 4.7. It yields three significant expansion coefficients because the data quality, especially at high redshift, does not allow constraints of higher-order modes, as discussed in Sect. 4.4.2.

The expansion rate reconstructed with this method is compared in the bottom panel of Fig. 4.7 to that of the best-fit model of the SNLS analysis, i.e. a flat ΛCDM with $\Omega_{\mathrm{m0}} = 0.263$.

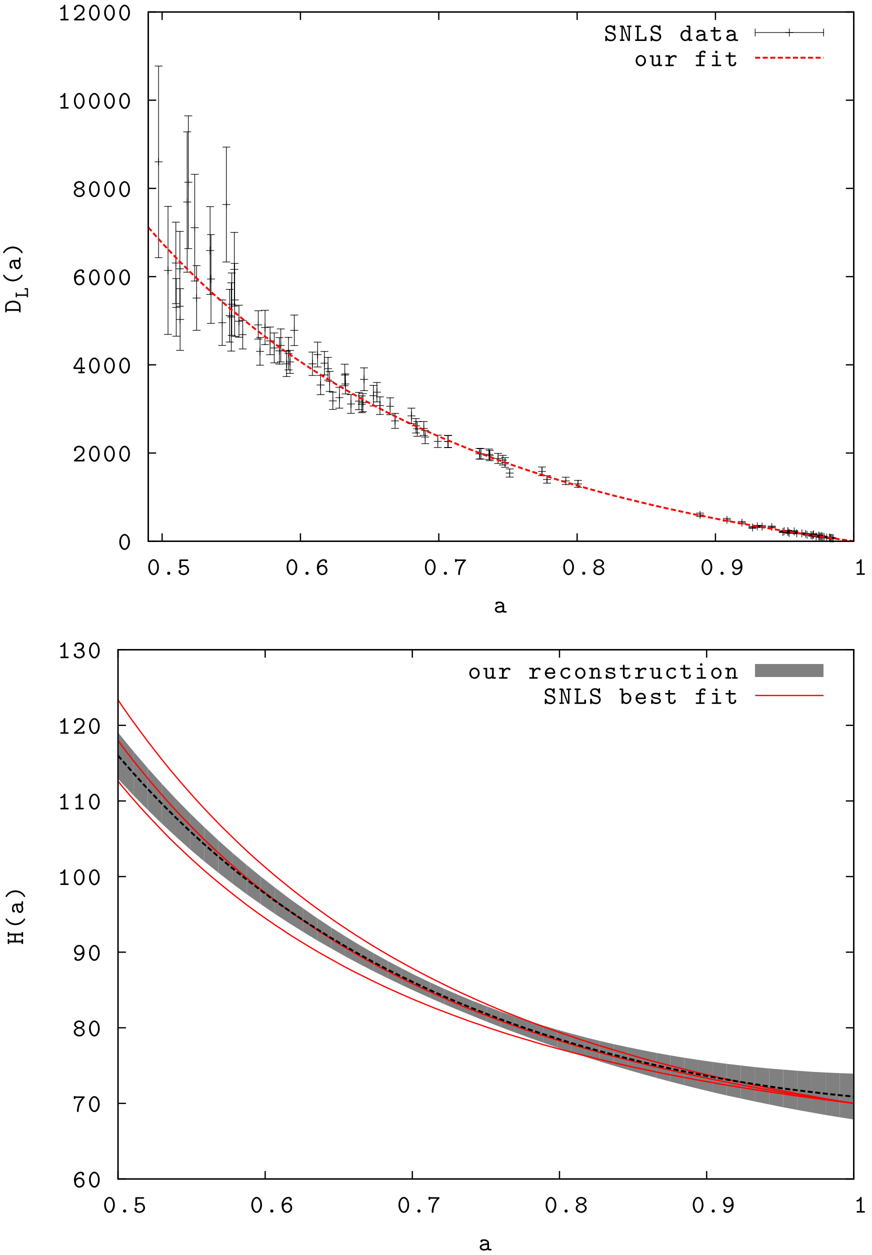

Figure 4.7: *Top panel:* The 1st year SNLS sample and our fit for the luminosity distance. *Bottom panel:* The model-independent reconstruction of the expansion rate and 1-σ errors thereof (gray shaded area), compared to the expansion rate of a ΛCDM model with the best fit parameter from Astier et al. (2006), $\Omega_{\rm m0} = 0.263 \pm 0.037$, and 1-$\sigma$ errors thereof (red curves).

4.7 Extending the Sample Beyond $z = 1$

Another interesting problem concerns what could improve the performance of the method. Clearly, both a larger sample of supernovae and a better accuracy in the individual measurements would help reducing the errors on the coefficients, which would eventually enable a significant estimate of more coefficients, and thus a more precise reconstruction of the expansion rate. From a mathematical point of view, adding more objects and reducing the uncertainties are equivalent: a sample four times larger than another yields the same results obtained with the smaller sample, if its error bars were to be reduced by one half. However, since the measurement accuracy cannot be indefinitely shrunk below a given limit, because of systematic uncertainties, a long run strategy to make best use of the method would be to increase the size of the sample.

Extending the sample to higher redshift can also help reducing the errors on the estimated coefficients. The issue is addressed by means of an extremely simplified example: an additional set of 20 objects, uniformly distributed between $z = 1$ and $z = 1.7$, has been added to the previously described simulated ΛCDM SNLS-like sample of supernovae, which only goes up to $z = 1$. The excess in the Fisher matrix due to the inclusion of the higher-z sample influences the errors on the coefficients, reducing the first by $\sim 10\%$ and the following ones by $\sim 20\%$, whereas if only 20 more objects with $z \leq 1$ were added, the gain would be smaller. However, this still does not allow more than three coefficients to be significantly pinned down, with the orthonormal function set described in Sect. 4.4.1.

The method has also been applied to a supernova sample which extends beyond $z = 1$, namely the one compiled by Davis et al. (2007), including the combined ESSENCE/SNLS/nearby dataset from Wood-Vasey et al. (2007) and the HST data from Riess et al. (2007). It contains 192 supernovae, of which 15 fall within $1 < z < 1.75$. Although this sample contains more objects than the SNLS and extends to higher redshifts, the quality of the reconstruction achieved is not better than the one obtained using the SNLS data set. In fact, the errors on the coefficients

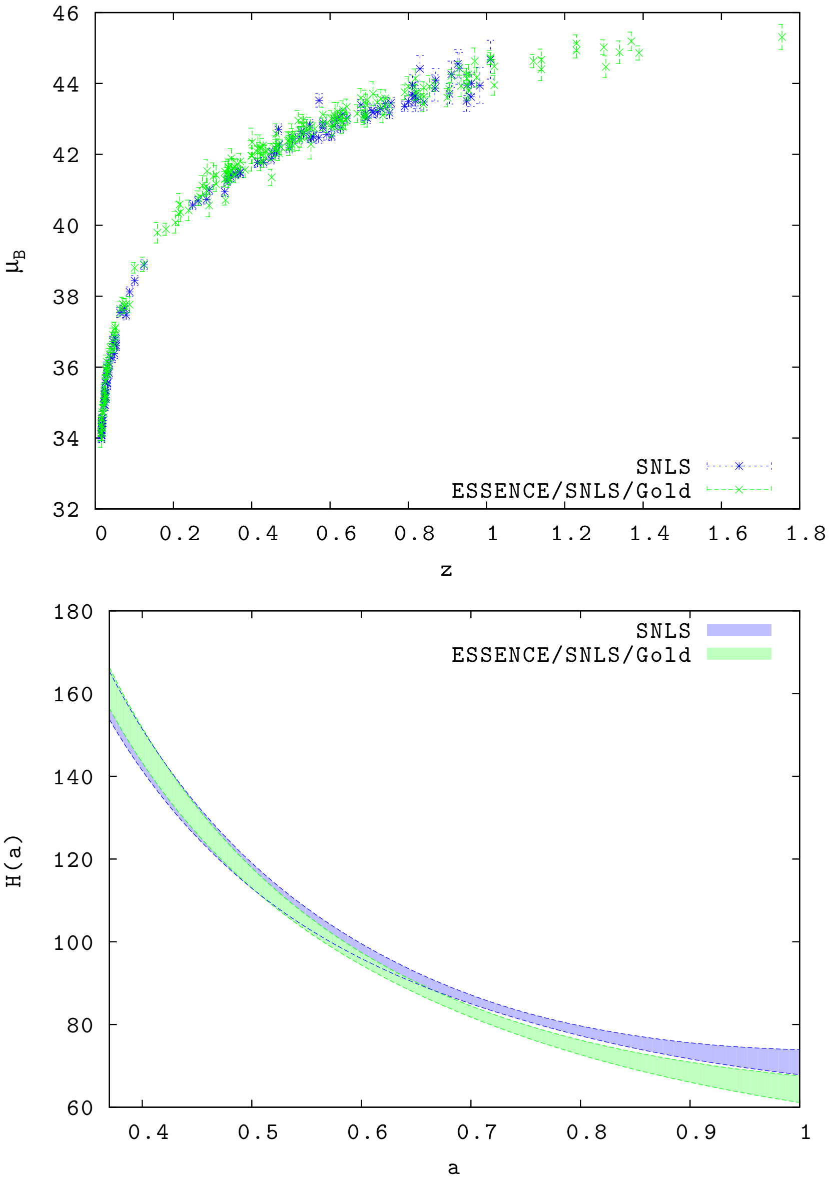

Figure 4.8: *Top panel:* The Hubble plot from the 1st year SNLS sample (Astier et al., 2006) and from the extended ESSENCE sample compiled by Davis et al. (2007). *Bottom panel:* The corresponding reconstruction of the expansion rate and 1-σ errors thereof, obtained from the two different samples; in both cases, three coefficients have been employed.

are slightly larger, because the individual uncertainties on the distance moduli in the extended ESSENCE sample are significantly higher than the SNLS ones (at least for $z < 0.8$), due to the different way luminosity distances are estimated from the photometric data by the two groups (a review on the different supernova light-curve fitters is given in Conley et al. 2007). The two different data sets and the corresponding reconstructions of the expansion rate are shown in Fig. 4.8; the disagreement between the two reconstructions at very low redshifts is due not only to differences in the data sets, but also to the fact that the method does not marginalise over the normalisation constant, H_0, thus slightly underestimating the error bars on $H(a)$.

4.8 Exact Solution for the Einstein-de Sitter Case

It is here shown how to construct the (inverse) expansion rate of the Einstein-de Sitter model from the first two modes of the function set obtained applying Gram-Schmidt orthonormalisation to the set of linearly independent functions specified by Eq. (4.22). The first two modes are

$$p_0(x) = \frac{1}{\sqrt{\alpha}}\frac{1}{x} \ , \quad p_1(x) = \frac{1}{\sqrt{C}}\left(\frac{1}{\sqrt{x}} + \frac{2\beta}{x}\right) \ , \tag{4.25}$$

with

$$\begin{aligned} \alpha &= \frac{1-a_{\min}}{a_{\min}} \ , \\ C &= 4 - \frac{8}{1-\sqrt{a_{\min}}} - \ln a_{\min} \ , \\ \beta &= \frac{1}{\sqrt{\alpha}}\frac{-1+\sqrt{a_{\min}}}{\sqrt{1-a_{\min}}} \ . \end{aligned} \tag{4.26}$$

It is straightforward to see, by projecting the distance in Eq. (4.21) onto the basis functions, that only the first two modes are needed, i.e.

$$D_{\mathrm{L}}(a) = \sum_{j=0}^{1} \tilde{c}_j p_j(a) \ , \tag{4.27}$$

where $\tilde{c}_j = \int_{a_{\min}}^{1} D_{\mathrm{L}}(a) p_j(a) da$ stands for the j-th *true* coefficient of the expansion. In this case $\tilde{c}_0 = 2(1+2\beta)\sqrt{\alpha}$ and $\tilde{c}_1 = -2\sqrt{C}$.

From the derivative of $p_0(a)$,

$$p_0'(x) = -\frac{1}{\sqrt{\alpha}}\frac{1}{x^2} \ , \tag{4.28}$$

the zero-th order Neumann series can be constructed following Eq. (4.6):

$$\begin{aligned} e_0^{(0)}(a) &= -a^3 p_0'(a) = \frac{1}{\sqrt{\alpha}} a \ , \\ e_1^{(0)}(a) &= \int_1^a \frac{\mathrm{d}x}{x^2} e_0^{(0)}(x) = \frac{1}{\sqrt{\alpha}} \ln a \ , \\ e_2^{(0)}(a) &= \int_1^a \frac{\mathrm{d}x}{x^2} e_1^{(0)}(x) = \frac{1}{\sqrt{\alpha}} \frac{a - 1 - \ln a}{a} \ . \end{aligned} \tag{4.29}$$

Up to second order, the zero-th order Neumann series for the (inverse) expansion rate is

$$e^{(0)}(a) = \sum_{k=0}^{2} a^k e_k^{(0)}(a) \tag{4.30}$$

$$= \frac{1}{\sqrt{\alpha}} \left(a + a \ln a + a(a-1) - a \ln a\right) = \frac{1}{\sqrt{\alpha}} a^2 \ . \tag{4.31}$$

Again, from the derivative of $p_1(a)$

$$p_1'(x) = -\frac{1}{\sqrt{C}} \left(\frac{1}{2x^{3/2}} + \frac{2\beta}{x^2} \right) \ , \tag{4.32}$$

the first-order Neumann series can be constructed:

$$\begin{aligned} e_0^{(1)}(a) &= -a^3 p_1'(a) = \frac{1}{\sqrt{C}} \left(\frac{a^{3/2}}{2} + 2\beta a \right) \ , \\ e_1^{(1)}(a) &= \int_1^a \frac{\mathrm{d}x}{x^2} e_0^{(1)}(x) = \frac{1}{\sqrt{C}} \left(\sqrt{a} + 2\beta \ln a - 1 \right) \ , \\ e_2^{(1)}(a) &= \int_1^a \frac{\mathrm{d}x}{x^2} e_1^{(1)}(x) = \\ &= \frac{1}{\sqrt{C}} \left(\frac{1}{a} - \frac{2}{\sqrt{a}} - 2\beta \frac{\ln a + 1}{a} + 1 + 2\beta \right) \ . \end{aligned} \tag{4.33}$$

The first-order Neumann series up to second order thus reads

$$e^{(1)}(a) = \sum_{k=0}^{2} a^k e_k^{(1)}(a) = \frac{1}{\sqrt{C}} \left(-\frac{a^{3/2}}{2} + (1 + 2\beta) a^2 \right) \ . \tag{4.34}$$

Now Eqs. (4.30) and (4.34) can be employed, along with the *true* coefficients of the expansion, and recalling the relations in Eq. (4.26), the inverse expansion rate for an Einstein-de Sitter universe is recovered:

$$
\begin{aligned}
e(a) &= \sum_{j=0}^{1} \tilde{c}_j e^{(j)}(a) = \\
&= \frac{2}{\sqrt{\alpha}}(1+2\beta)\sqrt{\alpha}a^2 - 2\sqrt{C}\frac{1}{\sqrt{C}}\left(-\frac{a^{3/2}}{2} + (1+2\beta)a^2\right) = \\
&= a^{3/2}\ . \qquad (4.35)
\end{aligned}
$$

Chapter 5

Reconstruction of the Linear Growth Factor and Application to Cosmic Shear

This chapter explains how the reconstructed expansion rate obtained from supernova data, following the details presented in Chapter 4, can be employed to estimate the linear growth factor for structure formation. Such a reconstruction of the growth factor, as well as the one of the expansion rate, does not depend on any assumption about dark energy. The expansion rate and the linear growth factor are the two main ingredients to describe the weak gravitational lensing signal due to the large scale structure: the results of a model-independent analysis of synthetic cosmic shear data are presented, showing that this approach, combined with a traditional ΛCDM analysis, contributes to tighten the constraints on the parameters $\Omega_{\rm m}$ and σ_8.

5.1 A Model-Independent Reconstruction of the Linear Growth Factor

As already outlined in Section 1.7, in the standard scenario of structure formation the density constrast δ of a linear dark matter perturbation evolves according to Eq. (1.30), a second-order differential equation where the expansion rate H acts as a friction term:

$$\ddot{\delta} + 2H\dot{\delta} - 4\pi G\bar{\rho}\delta = 0\ , \tag{5.1}$$

where dots indicate derivatives with respect to time. Recalling the Hubble expansion function $H(a) = H_0 E(a) = \dot{a}/a = \mathrm{d}a/(a\mathrm{d}t)$, Eq. (5.1) can be rewritten in terms of derivatives with respect to the scale factor a:

$$\delta'' + \left(\frac{3}{a} + \frac{E'(a)}{E(a)}\right)\delta' - \frac{3}{2}\frac{\Omega_\mathrm{m}}{a^5 E^2(a)}\delta = 0\ . \tag{5.2}$$

The solution to Eq. (5.2) can be calculated analytically for an Einstein-de Sitter model, where $E(a) = a^{-3/2}$ and $\delta(a) \propto a$. It is worth mentioning that this result is independent of Ω_m, in the sense that, due to the form of Eq. (5.2), the solution would still be $\delta(a) \propto a$ even if the expansion rate had the form $E(a) = \sqrt{\Omega_\mathrm{m}}\, a^{-3/2}$, which is an approximation for any ΛCDM model (even quintessence models with non-evolving dark energy) at very early times.

The Einstein-de Sitter solution is usually employed also when dealing with other models, to calculate plausible initial conditions, since, at very early time, it is reasonable to assume an Einstein-de Sitter-like expansion. From $\delta(a) \propto a$ one finds $\delta(a_\mathrm{early}) = a_\mathrm{early}$, $\delta'(a_\mathrm{early}) = 1$, where it is usually assumed $a_\mathrm{early} = a_\mathrm{eq}$, i.e. the time of matter-radiation equality.

In the literature, Eq. (5.2) is integrated numerically after choosing a cosmological model; in the case of a ΛCDM, a fitting formula for the growth factor, provided by Carroll et al. (1992), is generally used.

The approach chosen here is different: the solution to Eq. (5.2) is calculated by making use of the expansion rate from the empirical reconstruction detailed in the previous chapter, together with independent information on the matter density parameter Ω_m. The estimate of the growth factor for linear density perturbations achieved in this way does not rely on any specific model for the dark energy; it depends, though, on the assumptions underlying Eqs. (5.1) and (5.2).

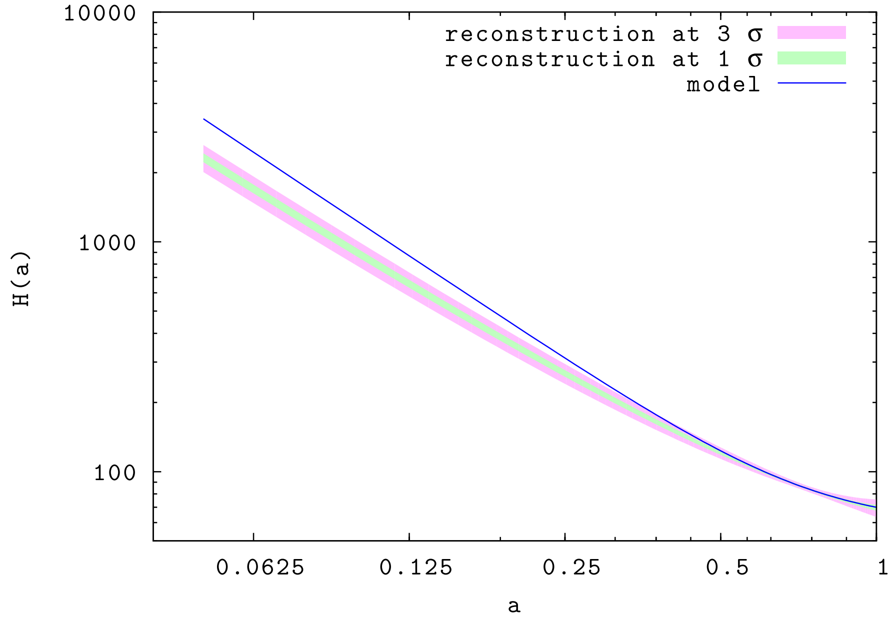

Figure 5.1: The reconstructed expansion rate for a simulated sample of supernovae in a ΛCDM universe, analogous to the one plotted in the top panel of Fig. 4.3 but extended to earlier epochs. The green contours stand for the reconstruction with 1-σ errors thereof, the pink contours for the 3-σ errors, and the blue curve represents the model. Note the logarithmic scale.

5.1.1 Initial Conditions

A delicate issue in this process is the choice of the right initial conditions to solve the differential equation. Although the method described in Chapter 4 yields, in principle, a reconstruction of $E(a)$ for any value of the scale factor, the expansion function will be strongly constrained by the data only in the redshift range where supernovae are observable, as is evident from Fig. 5.1, which shows the same result as the top panel of Fig. 4.3 but extended to $a \to 0$. The reconstruction, which reproduces the underlying model very accurately up to $a = 0.5$, becomes clearly unreliable at $a < 0.4$, even at the 3-σ confidence level.

A possible approach to overcome such a complication is to solve the differential equation only over the redshift range where the data are defined, but in this case the initial conditions at the value of a corresponding to the maximum redshift of the supernova sample must be provided, and they cannot be determined without assuming a cosmological model, nor using the Einstein-de Sitter approximation, which is manifestly not valid at such low redshits. This is shown in the top panel of Fig. 5.2, which shows the expected growth factor $D(a)$, normalised such that $D = 1$ at present, in a ΛCDM (red solid line) and in an Einstein-de Sitter model (magenta dotted line), along with the growth factor obtained integrating Eq. (5.2) using the exact ΛCDM expansion function, but imposing the initial conditions at $a = 0.5$, instead than at a_{eq}. Both Einstein-de Sitter-like initial conditions (i.e. $\delta(a = 0.5) = 0.5$, $\delta' = 1$; blue dashed line) and the correct value for δ' as expected in ΛCDM (black dotted line) have been used, in order to emphasise how the knowledge of the derivative of δ improves the result significantly.

In this work it has been chosen, instead, to solve the equation over a larger redshift range, going backwards in time enough in order to be able to set Einstein-de Sitter-like initial conditions. As evident from the bottom panel of Fig. 5.2, the latter approach (i.e. using the reconstructed $E(a)$ and Einstein-de Sitter-like initial conditions at an early time, plotted in light blue) yields an accurate estimate of the growth factor over a much larger redshift range with respect to the previous one (i.e. using the exact expression for $E(a)$ but Einstein-de Sitter-like initial condition at later times, plotted in blue).

5.1.2 Dependence on Ω_{m}

The previous discussion assumes a perfect knowledge of the matter density parameter. The top panel of Fig. 5.3 shows the solution to Eq. (5.2), obtained by making use of the exact expression of the expansion rate and different values for Ω_{m}, ranging beteween 0 and 1, where the correct value is $\Omega_{\mathrm{m}} = 0.3$ (plotted in light blue). It is also shown, in the bottom panel, how the choice of Ω_{m} influences the solution obtained by making use of the reconstructed expansion rate instead of the exact one.

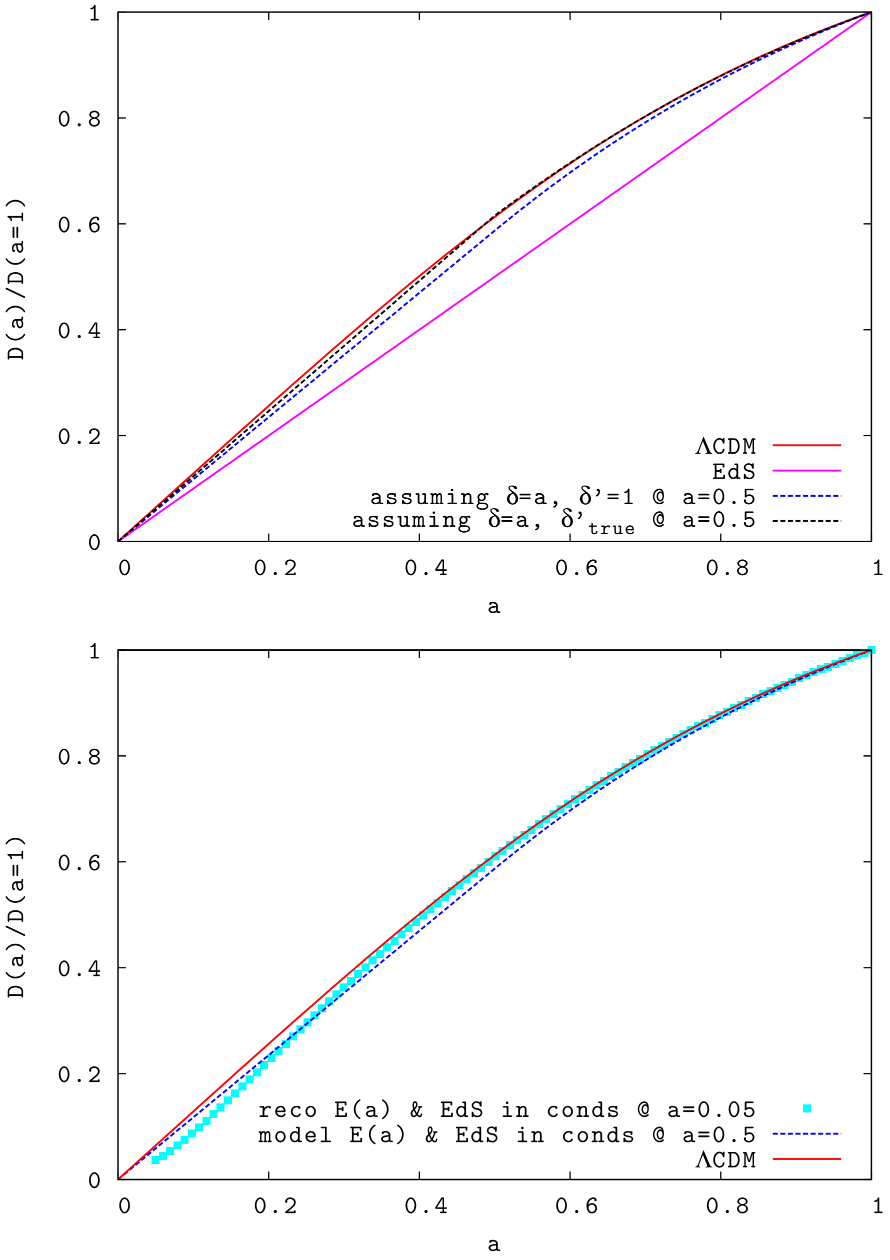

Figure 5.2: *Top panel:* The growth factor, normalised to $= 1$ at the present epoch, as expected in a ΛCDM (red solid line) and Einstein-de Sitter (magenta solid line) model, and as reconstructed solving Eq. (5.2), employing the exact model expansion rate and imposing the following initial conditions at $a = 0.5$: $\delta \propto a$, $\delta' = 1$ (blue dashed line) and $\delta \propto a$, $\delta' = \delta'_{\rm true}(a = 0.5) \approx 0.85$ (black dashed line), respectively. *Bottom panel:* Analogously, the growth factor as expected in a ΛCDM (red solid line) and as reconstructed solving Eq. (5.2), employing the exact model expansion rate and imposing Einstein-de Sitter-like initial conditions at $a = 0.5$ (blue dashed line), and employing the expansion rate reconstructed from a ΛCDM simulated sample of SNe Ia and imposing Einstein-de Sitter-like initial conditions at $a = 0.05$ (cyan squares), respectively.

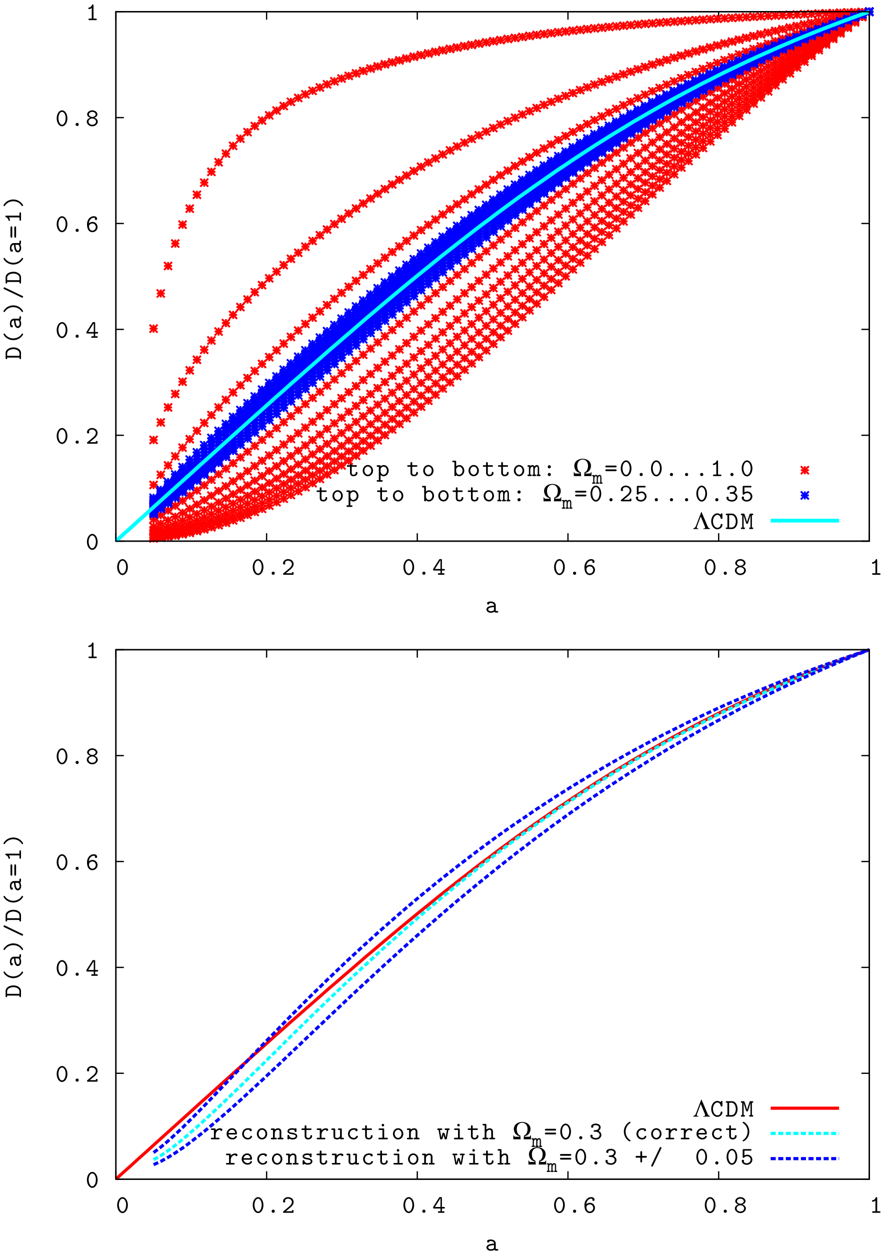

Figure 5.3: *Top panel:* The growth factor, normalised to $= 1$ at the present epoch, as expected in a ΛCDM with $\Omega_{\rm m} = 0.3$ (cyan solid line) and as reconstructed solving Eq. (5.2), employing the exact expression for the expansion rate but assuming several different values for the matter density parameter (plotted in red: $\Omega_{\rm m} = 0, 0.1, 0.2, ..., 1.0$; plotted in blueblue: $\Omega_{\rm m} = 0.25, 0.26, 0.27..., 0.35$). *Bottom panel:* The growth factor as expected in a ΛCDM with $\Omega_{\rm m} = 0.3$ (red solid line) and as reconstructed solving Eq. (5.2), employing the empirical estimate for the expansion rate and the exact value $\Omega_{\rm m} = 0.3$ (cyan dashed line), and an incorrect value $\Omega_{\rm m} = 0.3 \pm 0.05$ (blue dashed lines).

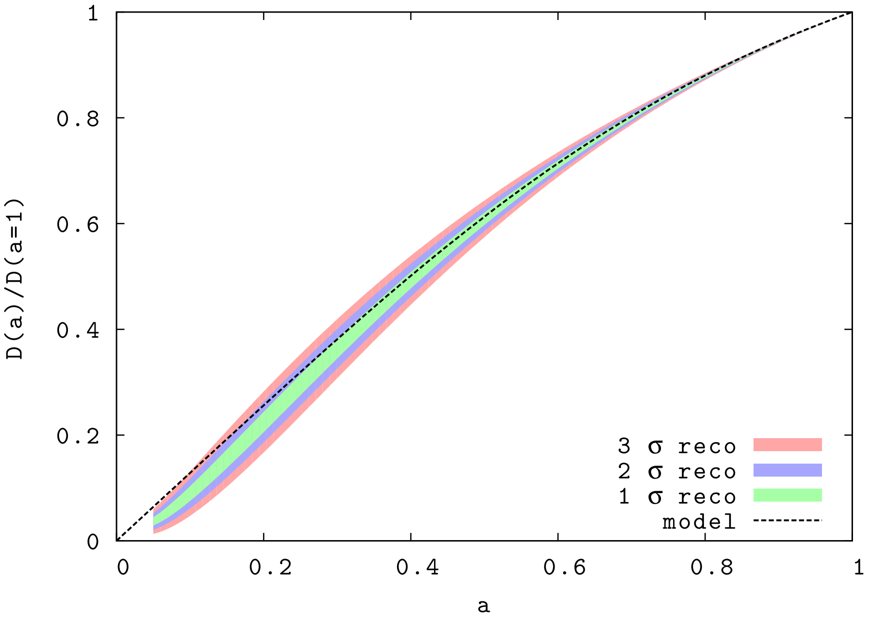

Figure 5.4: The growth factor, normalised to = 1 at the present epoch, reconstructed solving Eq. (5.2) with the empirical estimator of $E(a)$, with 1-σ (green), 2-σ (ble) and 3-σ (red) error bars, respectively; the black dashed line represents the growth factor of the underlying ΛCDM model. The value of Ω_m is here assumed to be known without uncertainty.

5.1.3 Dependence on the errors on $E(a)$

Furthermore, the solution for the growth of density fluctuations is here obtained starting from an estimator of the expansion rate, and the errors on it (i.e. on the expansion coefficients) propagate into errors on the growth factor $D(a)$ as follows:

$$\Delta D(a) = \sqrt{\sum_{i,j=0}^{M-1} \frac{\partial D(a)}{\partial c_i}\frac{\partial D(a)}{\partial c_j}\Delta c_i \Delta c_j}\ . \tag{5.3}$$

This is shown in Fig.(5.4), where the reconstructed growth factor, here obtained assuming perfect knowledge of Ω_m, is plotted with 1, 2 and 3-σ error bars thereof: up to very early times ($a \geq 0.1$) the reconstructed growth factor agrees with that of the model at the 2-σ confidence level, or better.

5.2 A Novel Method to Combine Supernova and Cosmic Shear Data

As already mentioned in Section 2.5, the weak gravitational lensing signal imprinted on distant galaxies by large scale structures, usually referred to as cosmic shear, is an extraordinary tool to probe the matter content of the universe. Being able to provide an unbiased description of the matter density distribution from linear to non-linear scales, over the redshift range covered by the lensed sources, cosmic shear is a powerful probe to constrain cosmological parameters, such as the matter density parameter, $\Omega_{\rm m}$, and the amplitude of the matter power spectrum, σ_8. However, as pointed out in Section 2.5.5, current data sets suffer from a significant degeneracy between these two parameters, which may be lifted through the combination with independent measurements, such as CMB anisotropy data.

This work presents a novel method to overcome the aforementioned degeneracy between $\Omega_{\rm m}$ and σ_8, making use of a combination of cosmic shear and type-Ia supernova data. It is based on the method described in Chapter 4, which is able to reconstruct the cosmic expansion rate $E(a)$ from luminosity distance data without reference to a specific Friedmann model, and yields a robust reconstruction even using a sample of type-Ia supernovae of current quality. This reconstruction technique can be employed to calculate distances, to be then applied in the analysis of other cosmological datasets without assuming a specific model but relying directly on empirical evidence, with the limitations being set only by the quality of the data.

In particular, this method can be employed to calculate the distances involved in the cosmic shear signal and, with the assumption that gravity is described by Newtonian dynamics on small scales, also to calculate the growth factor for linear matter perturbations, to be then used in computing the cosmic shear power spectrum on linear scales. Hence, the cosmic shear signal on linear scales is parametrised in terms of the matter density parameter, $\Omega_{\rm m}$, and of the amplitude of the matter power spectrum, σ_8, in a different way than usual when a ΛCDM model is assumed: regarding the dynamics of structure growth, the dependence of the signal on σ_8 and

Ω_m is the same, but Ω_m does not enter into the specification of the geometry. The information that can be extracted following this approach is thus complementary to the one inferred within the ΛCDM assumption.

5.3 Cosmic Shear parameterisation

As already discussed in Section 2.5, the underlying quantity beneath the cosmic shear signal is the three-dimensional power spectrum of the dark matter distribution: its projection along the line of sight, referred to as the convergence (κ) power spectrum, is

$$P_\kappa(l) = \frac{9H_0^4\Omega_\mathrm{m}^2}{4c^4}\int_0^{w_\mathrm{H}} \mathrm{d}w \left(\frac{\bar{W}(w)}{a(w)}\right)^2 P_\delta\left(\frac{l}{f_K(w)};w\right) \,, \tag{5.4}$$

where w is the comoving radial coordinate, w_H refers to the horizon, $a(w)$ is the scale factor, and $f_K(w)$ is the comoving angular-diameter distance. Furthermore, P_δ is the dark matter power spectrum, and $\bar{W}(w)$ is a weight function taking into account the ratio of angular-diameter distances between lens and source, and observer and source, averaged over the redshift distribution of sources $n(w)$:

$$\bar{W}(w) = \int_w^{w_\mathrm{H}} \mathrm{d}w'\, n(w')\, \frac{f_K(w'-w)}{f_K(w')} \,. \tag{5.5}$$

The convergence power spectrum is related to the observed two-point statistics, such as the shear correlation functions $\xi_\pm$, in the following way:

$$\xi_\pm(\theta) = \frac{1}{2\pi}\int_0^\infty \mathrm{d}l\, l\, P_\kappa(l)\, J_{0,4}(l\theta) \,, \tag{5.6}$$

where θ is the angular separation between galaxy pairs, and $J_{0,4}$ are Bessel functions of the first kind.

As Eq. (5.4) points out, distances and the matter power spectrum are the basic ingredients to calculate P_κ: hence, at least on scales where the linear regime is still valid, knowledge of $E(a)$ and $D(a)$ is sufficient to perform cosmic-shear analyses. Distances are calculated from the expansion rate via

$$w(a_1,a_2) = \frac{c}{H_0}\int_{a_2}^{a_1} \frac{\mathrm{d}a}{a^2E(a)} \,, \tag{5.7}$$

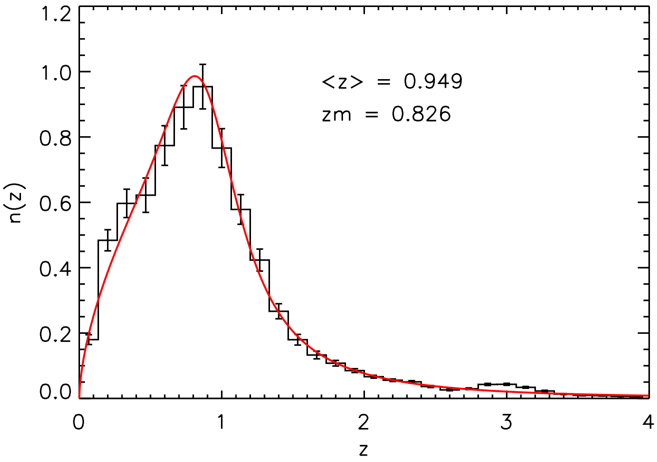

Figure 5.5: The redshift distribution of galaxies used for the weak lensing analysis of the third-year CFHTLS Wide data release. From Fu et al. (2008).

whereas the growth factor contributes quadratically to the matter power spectrum, taking into account its temporal evolution on linear scales: $P_\delta(k,a) = [D(a)]^2 \, P_\delta(k)$.

Regarding the contribution due to non-linear evolution in the power spectrum, it has initially not been included, in order to preserve the model-independence of the method, since current data sets allow to probe scales which are well within the linear regime. However, the integration in Eq. (5.6) goes up to very large l, and is thus sensitive to the inclusion (or not) of the non-linear evolution; the issue is addressed in Section 5.6.

In the following work, $E(a)$ is estimated from a simulated sample of type-Ia supernovae with observational characteristics similar to the SNLS (Astier et al., 2006) but luminosity distances drawn from a ΛCDM model: the reconstructed function is plotted in the top panel of Fig. 4.3 and employs three coefficients.

The sample contains data up to $z \approx 1$, and the reconstructed expansion rate is compatible with that of the model up to higher redshifts ($z \approx 1.5$), within 1-σ error bars. It is thus possible to apply it to the cosmic shear data, since the source redshift distributions from state-of-the-art surveys peak around $z \approx 0.8$ and decline quite rapidly for $z > 1$, as shown in Fig. 5.5.

5.4 Likelihood Analysis

5.4.1 General Remarks

This section presents the likelihood surfaces in the ($\Omega_{\rm m}$, σ_8) plane obtained from *the same* sample of simulated cosmic shear data, analysed assuming on one hand a flat ΛCDM model, and on the other hand the empirical parameterisation based on the model-independent reconstruction of $E(a)$ presented in Chapter 4. In the ΛCDM case, the non-linear power spectrum is modelled after the prescription by Peacock & Dodds (1996), whereas in the case of the empirical parameterisation, no correction for the non-linear evolution has been employed. The observable quantity is the two-point correlation function ξ_+ as a function of angular scale θ, and only scales $\theta > 10\,$arcmin have been considered, so that the assumption of linear density evolution is valid.

The log-likelihood is calculated as follows:

$$\chi^2_{1,2} = \frac{1}{2}\sum_{i,j}\left(\bar{\xi}_i - \xi_i^{(1;2)}\right)\left(C^{-1}\right)_{i,j}\left(\bar{\xi}_j - \xi_j^{(1;2)}\right) \,, \tag{5.8}$$

where $\bar{\xi}_i$ represents the simulated data vector, the indices $(1,2)$ refer to the ΛCDM model and the empirical parameterisation, respectively, and C is the covariance matrix of the two-point correlation function ξ_+, calculated according to the formula provided by Joachimi et al. (2008), which is valid under the assumption of Gaussian density fluctuations.

5.4.2 The Simulated Samples

First, a sample with characteristics similar to the most up-to-date measurements has been considered, with reference to Fu et al. (2008); a possible future experiment, with technical specifics reasonably within the reach of future ground and space-based projects, has also been examined, in order to fully probe the potential of the method. The observational characteristics of the two data sets are listed in Tab. 5.1, and the corresponding two-point correlation functions are plotted in Fig. 5.6. The

Table 5.1: The characteristics of the two simulated surveys considered in the course of this work.

	State-of-the-art Survey	Future Survey
Survey area	34.2 deg^2	100 deg^2
Galaxy number density	13.3 arcmin^{-2}	30 arcmin^{-2}
Intrinsic ellipticity dispersion	0.42	0.3

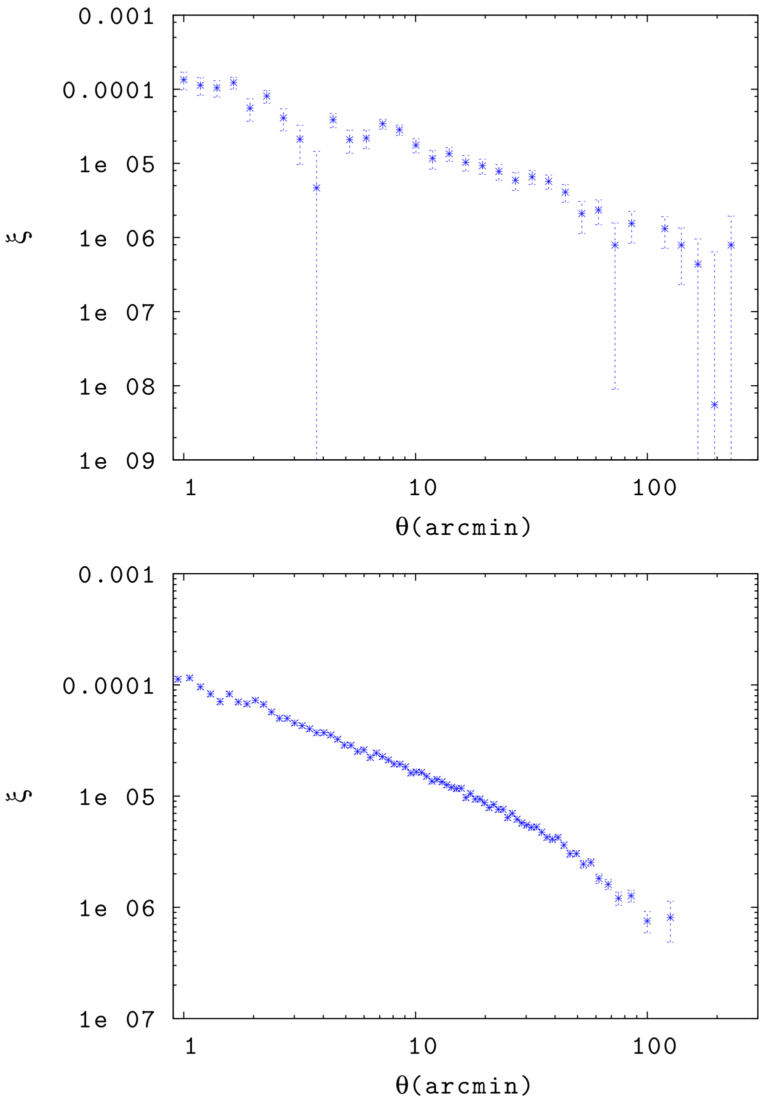

Figure 5.6: The two-point shear correlation function for the two synthetic data sets used in this analysis: from a state-of-the-art survey similar to the one analysed by Fu et al. (2008) (*top panel*) and from a possible future survey (*bottom panel*).

reference cosmology is, in both cases, a flat ΛCDM model, with $\Omega_{\rm m} = 0.3$, $\Omega_\Lambda = 0.7$, $h = 0.7$, $w = -1$ and $\sigma_8 = 0.8$.

The redshift distribution of the sources $n(z)$, which appears in Eq. (5.5), has been chosen to match the fitting formula presented in Fu et al. (2008):

$$n(z) = A\,\frac{z^a + z^{ab}}{z^b + c}\ , \tag{5.9}$$

where the normalisation A was calculated integrating up to the maximum redshift of the catalogue, $z_{\rm max} = 6$. The fit to the data obtained by Fu et al. (2008) is shown in Fig. 5.5, where the values of the parameters in Eq. (5.9) are $A = 1.555$, $a = 0.612$, $b = 8.125$ and $c = 0.620$, respectively.

5.4.3 Nuisance Parameters

In other cosmological studies of cosmic shear data, the parameters of the source redshift distribution (in this case a, b, c) are treated as nuisance parameters in the likelihood analysis and then marginalised over; for the sake of simplicity, the following analysis considers, instead, a lower-dimensionality likelihood, where the source redshift distribution parameters are fixed to their best-fit values. The inclusion of such parameters in the analysis does not change its principle, but only renders it more lengthy.

Regarding the empirical parameterisation, an additional set of parameters need to be taken into account, namely the expansion coefficients $\{c_i\}$. In principle, these should be treated as nuisance parameters and marginalised over. Fortunately, the particular dependence of the likelihood on the coefficients makes it possible to circumvent this step. In the special case of interest, where three coefficients are taken into account, the two-dimensional projections of the five-dimensional likelihood $\mathcal{L}_5(\Omega_{\rm m}, \sigma_8; \{c_i\})$ on the two parameters $\Omega_{\rm m}$, σ_8 and on each one of the coefficients are either planes or very close to planes, in the space of the other two coefficients. This suggests factorising the dependence on the coefficients in the following way:

$$\mathcal{L}_5\left(\Omega_{\rm m}, \sigma_8;\ \{c_i\}\right) \approx \mathcal{L}_0\left(\Omega_{\rm m}, \sigma_8;\ \{\hat{c}_i\}\right) \cdot f\left(\{c_i\}\right)\ , \tag{5.10}$$

where $\mathcal{L}_0$ indicates the two-dimensional likelihood, calculated as a function of Ω_m and σ_8 only, having fixed the values of the coefficients to their best-fit values coming from the supernova analysis, $\{\hat{c}_i\}$. The dependence on the coefficients is taken into account through

$$f\left(\{c_i\}\right) = \sum_i \left(c_i - \hat{c}_i\right) \alpha_i + 1 \ , \tag{5.11}$$

where the parameters α_i depend on the projections of the five-dimensional likelihood on the individual coefficients. In order to achieve a two-dimensional likelihood, $\mathcal{L}_5$ has to be marginalised over the coefficients:

$$\mathcal{L}_2\left(\Omega_\mathrm{m}, \sigma_8\right) = \int \mathrm{d}\vec{c}\, P\left(\vec{c}\right) \mathcal{L}_5\left(\Omega_\mathrm{m}, \sigma_8;\, \{c_i\}\right) \ . \tag{5.12}$$

If the priors $P(\vec{c})$ on the coefficients are chosen to be Gaussian, inserting the above assumption into Eq. (5.12) yields

$$\mathcal{L}_2\left(\Omega_\mathrm{m}, \sigma_8\right) \approx \mathcal{L}_0\left(\Omega_\mathrm{m}, \sigma_8;\, \{\hat{c}_i\}\right) \int \mathrm{d}\vec{c}\, P\left(\vec{c}\right) f\left(\{c_i\}\right) = \mathcal{L}_0\left(\Omega_\mathrm{m}, \sigma_8;\, \{\hat{c}_i\}\right) \ , \tag{5.13}$$

meaning that the marginalised, two-dimensional likelihood $\mathcal{L}_2(\Omega_\mathrm{m}, \sigma_8)$ can be approximated with the two-dimensional likelihood $\mathcal{L}_0(\Omega_\mathrm{m}, \sigma_8;\, \{\hat{c}_i\})$, where the values of the coefficients have been fixed to their best-fit values.

5.4.4 Separate Analysis

In Fig. 5.7 the likelihoods in the (Ω_m, σ_8) plane are shown, with both the traditional ΛCDM parameterisation and the empirical parameterisation developed in the course of this work; the top plots, with broader contours, refer to a state-of-the-art data set, whereas the bottom plots, with tighter contours, refer to a hypothetic, future survey.

The empirical parameterisation is not able to lift the degeneracy between the two parameters. It is however evident, in the results derived from both surveys, that the two approaches suffer from different degeneracies: cosmic shear typically constrains the product $\Omega_\mathrm{m}^\alpha \sigma_8$, with $\alpha \approx 0.6$ in the ΛCDM case, and $\alpha \approx 0.9$ in the case of the empirical parameterisation. The reason for that is the different parameterisation of the geometric part of the cosmic shear signal, which translates into

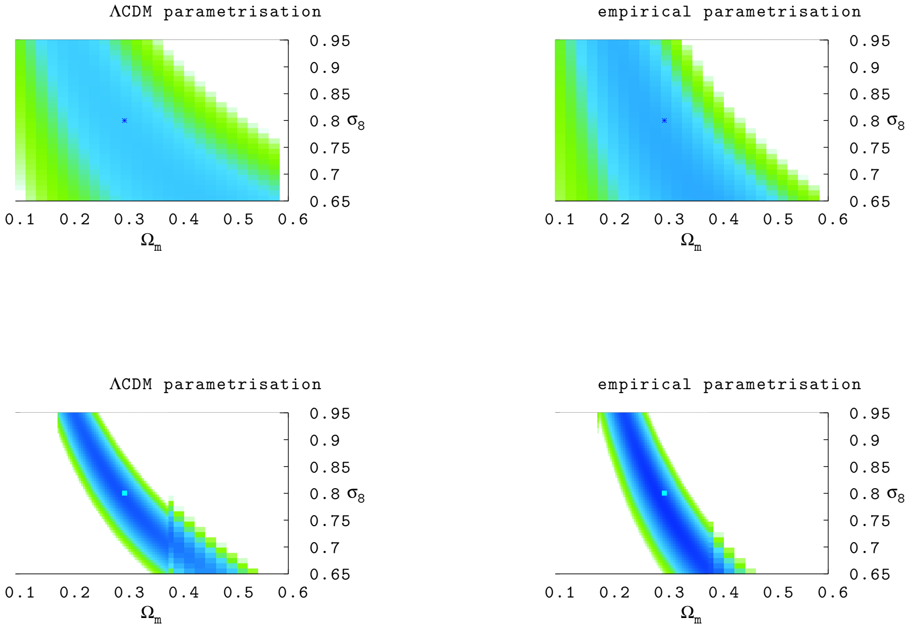

Figure 5.7: The two-dimensional likelihood in the ($\Omega_{\rm m}$, σ_8) plane for a state-of-the-art (*top panels*) and a future (*bottom panels*) survey, obtained by making use of the traditional ΛCDM parameterisation (*left panels*) and the empirical parameterisation developed in this work (*right panels*). The fiducial model, with $\Omega_{\rm m} = 0.3$ and $\sigma_8 = 0.8$, is indicated.

a different dependence on Ω_m. The complementarity of these results suggests that a combination of them might yield significantly tighter constraints on Ω_m and σ_8, especially in the case of a future survey.

It has to be remarked that the results of the empirical parameterisations are slightly biased towards lower Ω_m and higher σ_8: this is due to the total lack of information about the non-linear evolution in the matter power spectrum, which is more thoroughly discussed in Section 5.6.

5.5 Combined Analysis

The likelihood analyses performed in the two different cases yield complementary results: it is possible to combine them, using the tools of multimodel inference. The basic concepts which are employed in the following analysis of the cosmic shear data are outlined; for further details about the theoretical framework of multimodel inference, see Burnham & Anderson (2004) and references therein.

5.5.1 Multimodel Inference Theory

Multimodel inference arises from the simple consideration that ordinary inference, based on one model only, namely the best model found during model selection, treats this model as if it were the only one considered, thus ignoring uncertainty coming from the model selection process itself. The introduction of an explicit criterion to define what *is* a best model allows to attach a weight to each fitted model, taking into account the uncertainty that each of these models is the target best model: in this way, inference based on the full set of models is possible.

The Akaike information criterion (Akaike, 1973, 1974) is an unbiased tool for model selection:

$$\mathrm{AIC} = -2\log(\mathcal{L}(\hat{\theta}|\mathrm{data})) + 2K \ , \tag{5.14}$$

where K is the number of estimable parameters in the chosen model and $\hat{\theta}$ is the maximum likelihood exstimator of the parameter θ based on the assumed model and given the data. When K is large relative to the size of the sample n, the Akaike information criterion is scaled to take into account the smallness of the sample:

$$\mathrm{AIC}_c = -2\log(\mathcal{L}(\hat{\theta}|\mathrm{data})) + 2K + \frac{2K(K+1)}{n-K-1} \,, \tag{5.15}$$

which asymptotically tends to Eq. (5.14) for large n. The individual values of AIC (or AIC_c, respectively) contain arbitrary constants and are affected by the size of the sample, therefore they are usually rescaled to the minimum value, $\mathrm{AIC}_{\mathrm{min}}$, over the different models:

$$\Delta_i = \mathrm{AIC}_i - \mathrm{AIC}_{\mathrm{min}} \,. \tag{5.16}$$

Clearly, $\Delta = 0$ for the best model in the set, and Δ_i quantifies the loss of information due to the choice of the i-th model rather than the best one. For each model,

$$L(\theta|\mathrm{data}, i) = \exp(-\Delta_i/2) \tag{5.17}$$

is a measure of the likelihood over the model set, i. e. over the parameter space, given the data and the i-th model.

The model likelihoods are usually normalised such that their sum equals 1 and they can be treated as probabilities: hence, the Akaike weights are defined as

$$w_i = \frac{\exp(-\Delta_i/2)}{\sum_j \exp(-\Delta_j/2)} \,. \tag{5.18}$$

5.5.2 Joint Constraints

Multimodel inference can be employed when a parameter is in common over all models, as are Ω_{m} and σ_8 in the case of this work, and it is particularly useful when two or more models have nearly equal support. In particular, in the assumption that both models, i.e. the ΛCDM and the empirical parameterisation, are a good description of the underlying universe, the results obtained assuming the two models separately can be combined in order to tighten the constraints on Ω_{m} and σ_8.

The Akaike weights are calculated for each point $\vec{p}$ in the ($\Omega_{\rm m}$, σ_8) plane, according to Eq. (5.18), for both models $i = 1, 2$:

$$w_i\left(\vec{p}\right) = \frac{\exp\left[-\Delta_i\left(\vec{p}\right)/2\right]}{\sum_{j=1,2}\int {\rm d}\vec{p}\,\exp\left[-\Delta_j\left(\vec{p}\right)/2\right]}\ ; \tag{5.19}$$

the total probability is given by $P_{\rm tot}(\vec{p}) = \sum_{i=1,2} w_i$, whereas $P_{\rm joint}(\vec{p}) = \prod_{i=1,2} w_i$ identifies the probability that both models are true. The Akaike weights for the two separate models are shown in the top panel of Fig. 5.8, in the case of a future cosmic shear survey; the bottom panel of Fig. 5.8 shows, instead, the points where the joint probability is significantly different from zero, i.e. the values of $\Omega_{\rm m}$ and σ_8 which are more plausible given the data and the assumption of both models.

The additional information coming from the model-independent reconstruction of the expansion rate from supernova data is crucial to break the degeneracy and obtain very tight constraints on $\Omega_{\rm m}$ and σ_8, even though the assumption that the underlying model is well described by a ΛCDM has not been released.

As already mentioned, the slight bias in the determination of the best-fit value for ($\Omega_{\rm m}$, σ_8) is due to the fact that no information on the non-linear evolution of the power spectrum is included in the empirical parameterisation.

5.6 Including Non-Linear Evolution

This section presents the results of an analysis almost identical to the one performed in the previous sections, with the only difference that a correction for the non-linear evolution of the power spectrum on small scales is applied here also to the empirical parameterisation.

The prescription proposed by Peacock & Dodds (1996) for the non-linear evolution only needs as an input the linear growth factor and the linear power spectrum, hence it can in principle be calculated using the empirical estimate of $D(a)$ achieved from the expansion rate.

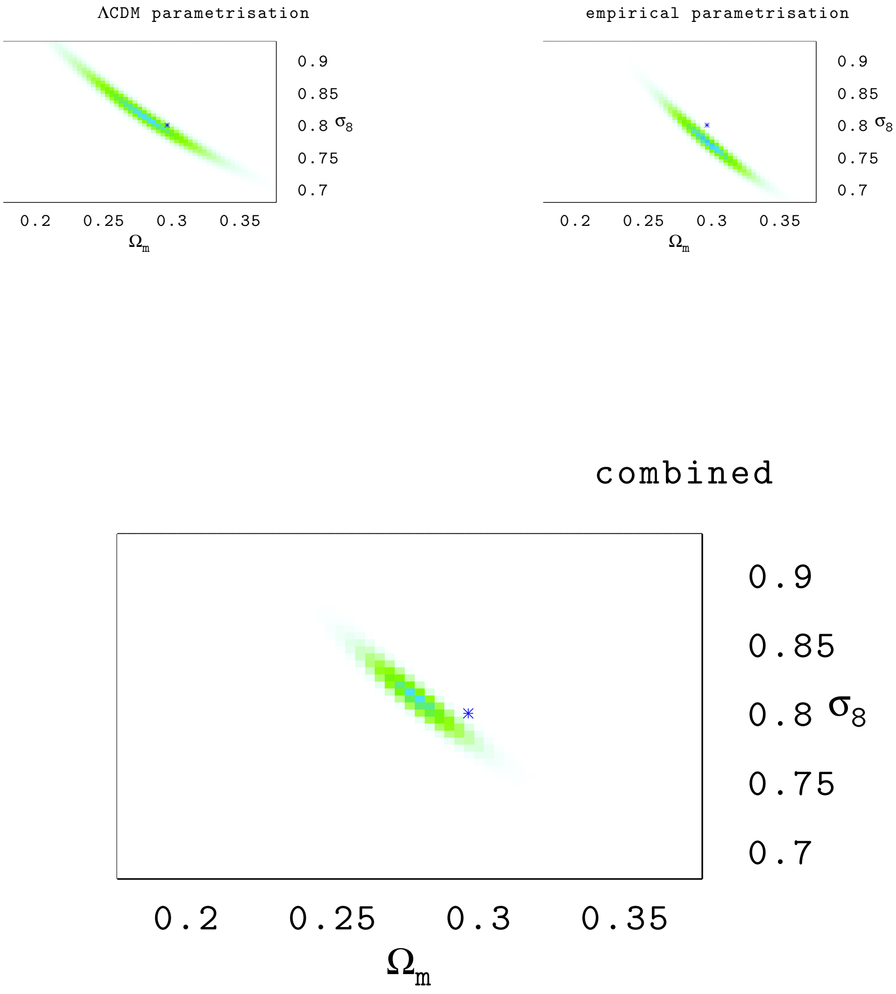

Figure 5.8: The Akaike weights, or probabilities, for the two different models (*top panels*) and the joint probability (*bottom panel*) in the ($\Omega_{\rm m}$, σ_8) plane, for a synthetic data set coming from a future cosmic shear survey. The fiducial model, with $\Omega_{\rm m} = 0.3$ and $\sigma_8 = 0.8$, is indicated.

It has to be mentioned that this prescription makes use of the growth factor normalised such that $D = a$ at early times. The method detailed in Section 5.1 can reconstruct, to very high accuracy, the shape of the growth factor and, thus, the growth factor normalised such that $D = 1$ today, at least on the redshift range where supernova data are available; it is, however, unable to determine the absolute normalisation of the growth factor at early epochs, since the expansion rate used to solve the differential equation is absolutely unconstrained, thus significantly underestimated, at such epochs. Neglecting this fact slightly underestimates the power spectrum, on small scales, at $z = 0$, with respect to the exact form given by Peacock & Dodds (1996), and yields virtually no effect at higher z (e.g. $z \sim 0.3$, which is most relevant for lensing). This approach is however better than ignoring the non-linear evolution at all: the mismatch between the non-linear power spectrum and this estimate of it is in fact smaller, by a factor ~ 5, than the one between the non-linear and the linear power spectrum.

In full analogy to Fig. 5.8, the top panel of Fig. 5.9 shows the Akaike weights for the two separate models, in the case of a future cosmic shear survey; the bottom panel of Fig. 5.9 shows the combined results: it is clearly evident that the bias, present in Fig. 5.8, has disappeared, and that the very tight constraints point towards the fiducial values for $\Omega_{\rm m}$ and σ_8.

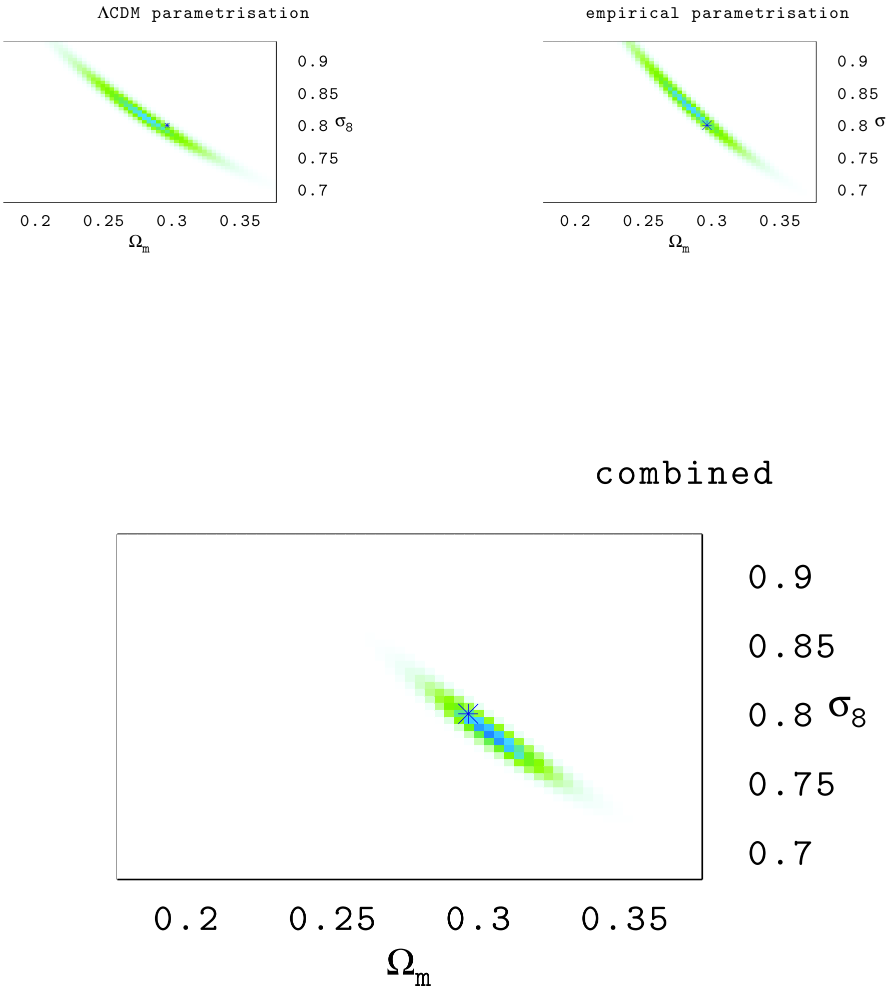

Figure 5.9: Analogous to Fig. 5.8, but including the non-linear evolution of the power spectrum from Peacock & Dodds (1996) also in the empirical parameterisation: the bias has disappeared.

Chapter 6

Extending the Model-Independent Reconstruction of the Expansion Rate: BAO and PCA

This chapter describes two separate, further applications of the model-independent reconstruction technique described in Chapter 4. First, a feasibility study of a possible application of the method to future-generation BAO data sets is presented: the angular-diameter distance is here employed, analogously to the luminosity distance in the supernova case, to estimate the expansion rate, and the reconstruction is then compared to the direct estimate of the expansion rate, also achievable from BAO data (for this part of work the collaboration of Licia Verde is acknowledged). Then, the issue of whether an optimal basis function set for the reconstruction method exists is addressed: principal component analysis (PCA) is employed to derive a basis of functions which maximises the separability of different cosmological models in the analysis of a generic data set, and this basis is eventually inserted in the algorithm described in Chapter 4 to reconstruct the expansion rate (this part of work has been carried out in collaboration with Matteo Maturi).

6.1 The Expansion Rate from Baryon Acoustic Oscillations

The model-independent technique developed during this work and described in Chapter 4 makes use of luminosity distance data in order to reconstruct the cosmic expansion rate, $H(a)$, without assuming any specific model for the dark energy. Because of Etherington's relation, Eq. (1.24), which relates the luminosity distance to the angular-diameter distance, it is straightforward to generalise the method, so that it can be applied to observational probes of the latter, such as baryon acoustic oscillations. As described in Section 2.2, future (spectroscopic) BAO experiments are expected to yield independent estimates of D_{A} and H in redshift bins: it is thus interesting to compare the direct estimate of the expansion rate to the one reconstructed using distance data drawn from the same galaxy survey.

6.1.1 Simulating the Data Set

The future BAO experiment simulated in this work is the Baryon Oscillation Spectroscopic Survey (BOSS), which will run from 2009 to 2014 at the SDSS telescope and will cover the redshift range $z = 0 - 0.7$ (for further details visit `www.sdss3.org`).

The cosmological distance errors are calculated following Seo & Eisenstein (2007) and the public C-program provided by the authors: the power spectrum is assumed to have Gaussian statistical errors, which are constructed straightforwardly from the finite volume of the survey and the incomplete sampling of the underlying density field with galaxies, and these errors are then propagated to the cosmological distance scale using the Fisher matrix formalism. The key element of such a method, besides the survey specifications, is the inclusion of non-linear effects which, as described in Section 2.2.2, tend to degrade the BAO signature.

The formalism to include non-linearities, developed by Eisenstein et al. (2007), assumes that the erasure of the acoustic signature can be understood in terms of motions of matter and galaxies relative to the initial preferred separation, caused by either cluster formation or coherent motions, such as bulk flows. The smearing of the BAO peak, due to these small-scale motions, is modelled by means of the distribution of the differences of the Lagrangian displacements of pairs of particles initially separated by a separation equal to the sound horizon. The rms radial displacement across ($\Sigma_\perp$) and along ($\Sigma_\parallel$) the line of sight are well predicted by a simple model:

$$\Sigma_\perp = \Sigma_0 \, D \, , \tag{6.1}$$

$$\Sigma_\parallel = \Sigma_0 \, D(1+f) \, , \tag{6.2}$$

where $\Sigma_0 = 12.4(\sigma_8/0.9)(\mathrm{Mpc}/h)$, $f = \mathrm{d}(\ln D)/\mathrm{d}(\ln a) \approx \Omega_m(z)^{0.6}$, and D is the growth factor normalised such that $D = 1/(1+z)$ at very high z, i.e. $D = 0.758$ at $z \approx 0$. The enhancement of the displacement along the line of sight is due to the fact that velocities and displacements are well correlated on large scales, hence the same velocity that gives the real-space displacement also alters the position in redshift space.

If the transverse displacements are approximated as being the same as the radial ones, the distribution of the displacement vector is nearly an elliptical Gaussian. To the extent that Σ_0 is treated as a constant, the effect on the correlation function becomes a simple convolution, and the modification of the power spectrum is simply a multiplication by a Gaussian:

$$P(\vec{k}) = P_{\mathrm{lin}}(\vec{k}) \exp\left(-\frac{k_\parallel^2}{2\Sigma_\parallel^2} - \frac{k_\perp^2}{2\Sigma_\perp^2} \right) \, . \tag{6.3}$$

The resulting formalism to calculate errors in the cosmological distance scale is function of the surveyed volume V, of the shot noise nP, where n is the comoving number density of galaxies and P the power spectrum, and of the parameters $\Sigma_\perp$ and $\Sigma_\parallel$, taking into account the non-linear effects; also needed are the bias factor, b, and the redshift distortion parameter, $\beta = \Omega_m(z)^{0.6}/b$.

The fitting formulae provided by Seo & Eisenstein (2007) are applied to calculate a 2-dimensional Fisher matrix, which yields the fractional errors on the measurement of the sound horizon scale along ($s_\parallel$) and across ($s_\perp$) the line of sight, which

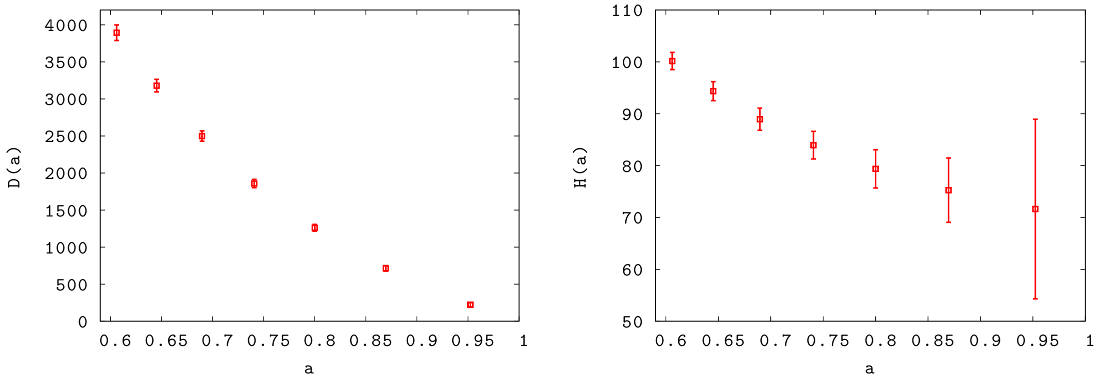

Figure 6.1: The simulated measurements of distance (*left panel*) and expansion rate (*right panel*), obtained using the technical specifics of the BOSS survey.

are equivalent to fractional errors on $D_{\rm A}/s$ and $H \cdot s$, respectively, where s is the sound horizon scale determined by the CMB, $s = 153.3 \pm 2\,{\rm Mpc}$ (from Tab. 3 of Komatsu et al. 2009).

A synthetic set of measurements of $D_{\rm A}(z)$ and $H(z)$, with values drawn from a flat ΛCDM model ($\Omega_{\rm m} = 0.3$, $\Omega_\Lambda = 0.7$, $h = 0.7$, $w = -1$) and error bars calculated using the formalism described above, is shown in Fig. 6.1 for 7 equally spaced redshift bins between $z = 0$ and $z = 0.7$. In order to reproduce the planned specifics of the BOSS survey, the following parameters have been used: a survey area of 10,000 sq.deg., a mean galaxy density of $2.6 \times 10^{-4}\,(h/{\rm Mpc})^3$, a shot noise $nP \approx 2$ and a bias factor $b = 1.6$ (L. Verde, private communication). Due to the scarcity of data points in redshift, no scatter has been added about the fiducial model, in order to avoid the introduction of a non-physically motivated bias.

6.1.2 The Expansion Rate: Reconstruction and Direct Estimate

In order to apply the reconstruction algorithm described in Chapter 4 to the BAO data detailed in the previous section, the angular-diameter distance has to be translated into luminosity distance:

$$D_L(z) = D_A(z)\,(1+z)^2\,, \tag{6.4}$$

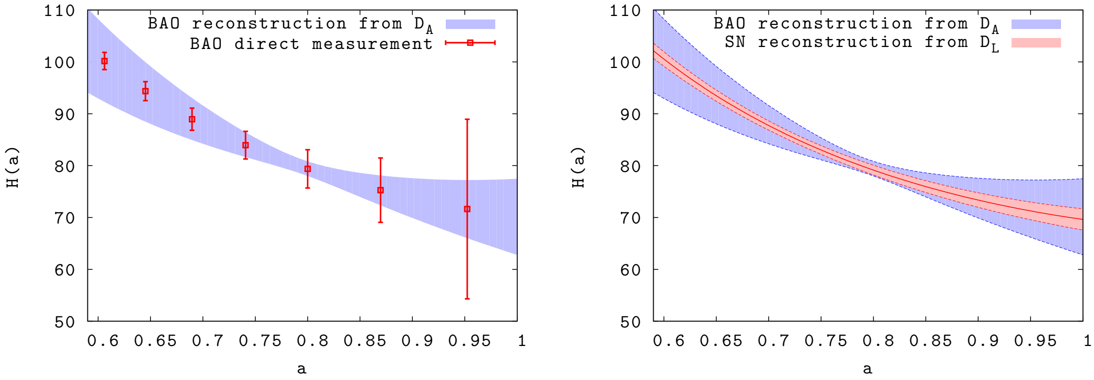

Figure 6.2: *Left panel*: The expansion rate reconstructed from simulated, BOSS-like distance data (blue filled contours) and directly estimated from the same survey (red points). *Right panel*: The expansion rate reconstructed from simulated BAO distance data, reproducing the future survey BOSS (blue filled contours) and from simulated supernova data, reproducing the state-of-the-art SNLS survey (red filled contours); the thick red line represents the model.

along with the errors thereof:

$$\Delta D_L(z) = (1+z)^2 \sqrt{\Delta D_A(z)^2 + 4\frac{\Delta z^2 D_A(z)^2}{(1+z)^2}} \approx (1+z)^2 \Delta D_A(z) \; ; \tag{6.5}$$

the last step is only valid for spectroscopic surveys, where the uncertainty on the redshift estimation, Δz, is negligible.

The result of the reconstruction of the expansion rate applied to the BAO distance data is shown in the left panel of Fig. 6.2, along with the direct measurements of the expansion rate from the detection of the BAO feature in the radial direction: the results are clearly consistent, but the use of the reconstruction technique yields no significant gain to the direct measurement, with the reconstruction having smaller error bars than the direct measurement at lower redshifts and larger at higher redshifts.

Photometric surveys targeting baryon acoustic oscillations are unable to yield a direct, independent measurement of $H(z)$: had the error bars achieved from this reconstruction of $H(z)$ using only distance data been significantly smaller, over the whole redshift range, than those of the direct measurement, this method could have represented an alternative to probe the expansion rate without the need for spectroscopy. Unfortunately, this did not turn out to be the case.

The quality of the BAO data used in this work allows to estimate the first three coefficients of the expansion, analogous to the SNLS-like sample of type-Ia supernovae described in Section 4.4.2; however, in the BAO case the errors on the coefficients, and thus on the recovered expansion rate, are larger, as shown in the right panel of Fig. 6.2. The method is in fact sensitive to the number of data points, hence it performs significantly better with supernova data than with BAO; for the same reason, the addition of the seven data points from BAO to a supernova sample does not improve any better the constraints obtained from supernovae alone.

6.2 Optimisation of the Basis Function Set with Principal Component Analysis

This section presents an application of principal component analysis, aimed at the definition of the best linear transformation to perform an optimal dimensionality reduction of any cosmological data set: this approach is able to construct a basis function set which maximises the power to discern between different cosmological models and to highlight the possible existence of unexpected features not foreseen when a specific model is adopted. In particular, the case of luminosity-distance data sets is considered, and the optimised basis is then used to improve the reconstruction technique described in Chapter 4 to derive the expansion rate from distance data.

The following formalism has been derived having in mind the analysis of cosmological data sets, but its application is completely general. For further details regarding principal component analysis techniques, also known as Karhunen-Loève methods, see Tegmark et al. (1997) and references therein.

6.2.1 An Optimised Basis Function Set for Cosmology

Following the formalism developed by Maturi & Mignone (2009), any data set can be represented as a vector $\vec{d} \in \mathbb{R}^n$, whose dimension n corresponds to the number of available data points in the set. In order to investigate this space, it is sampled with a set of M vectors which model the data, hereafter referred to as the training set T:

$$\left\{\vec{t_i} \in T \mid i = 1, ..., M\right\} \quad \text{with} \quad \vec{t_i} \in \mathbb{R}^n ; \tag{6.6}$$

the sampling of the model vectors $\vec{t_i}$ is the same as the one of the data vector to be analysed, and it can be discrete and irregular, depending on the quality of the data.

Once the possible models which are spanned by the data have been sampled, the extraction of the information they contain can be optimised via a linear transformation, $W : \mathbb{R}^n \rightarrow \mathbb{R}^n$, which maps the training set vectors into a space, referred to as the feature space, where their projections $\vec{\tau_i} = W^T \vec{t_i} \in \mathbb{R}^n$ (hereafter referred to as features) have the maximum scatter in very few components. This linear transformation is given by a set of n orthonormal vectors, $\{\vec{w_i} \in \mathbb{R}^n \mid i = 1, ..., n\}$, known as principal components.

The principal components are found by solving the following eigenvalue problem:

$$\vec{w_i} = \lambda_i \, S \vec{w_i} \, , \tag{6.7}$$

and by sorting them in descending order, i.e. $|\lambda_i| \geq |\lambda_{i+1}|$, to ensure the largest feature separation in the very first components. The so-called scatter matrix,

$$S = \sum_{i=1}^{M} \left(\vec{t_i} - \vec{t}_{\mathrm{ref}}\right) \left(\vec{t_i} - \vec{t}_{\mathrm{ref}}\right)^T \in \mathcal{M}_{\mathrm{n \times n}} \, , \tag{6.8}$$

encodes the differences (or scatter) between each training vector $\vec{t_i}$, i.e. a given model, and a reference vector, $\vec{t}_{\mathrm{ref}}$, around which the scatter is maximized. The reference vector defines the origin of the feature space and is usually set as the average of the training set, $\vec{t}_{\mathrm{ref}} \equiv \langle \vec{t} \rangle$, but a different $\vec{t}_{\mathrm{ref}}$ can be used instead, depending on the specific problem at hand.

The model vectors $\vec{t_i}$ can in principle be a set of arbitrary functions, but it is convenient to consider models that at least weakly resemble the data set. The training set is, in this work, based on Friedmann ΛCDM cosmologies with different cosmological parameters, but of course other kind of cosmological models can be used as well, such as e.g. cosmologies with dynamical dark energy, based on modified gravity theories, or even a mixture of different cosmological models.

It is worth remarking that the principal components derived in this way constitute a full basis system for the training-set cosmologies only. They are, however, very flexible and able to reproduce trends which are unknown to the models belonging to the training set. Furthermore, the principal components $\vec{w}_i$ have no direct physical meaning, since they are, by construction, linear combinations of the same observable in different models: this preserves a certain degree of model-independence in the formalism.

6.2.2 Principal Components as an Optimisation Problem

The derivation of the principal components, as outlined in the previous section, can be interpreted as a constrained optimisation problem, where the subset of the linear orthonormal transformation W which maximizes the separation between different cosmologies is sought. This is achieved by maximising the following quantity, $L = \vec{w}_i^T S \vec{w}_i + \tilde{\lambda}_i(\vec{w}_i^T \vec{w}_i - 1)$, with respect to $\vec{w}_i$, i.e. by looking for the solution of $\delta L / \delta \vec{w}_i^T = 0$. This leads to the eigenvalue problem expressed by Eq. (6.7), with $\lambda_i = -1/\tilde{\lambda}_i$, and consequently to the principal components $\vec{w}_i$.

If the number of training vectors is smaller than their dimension, i.e. $M < n$, only the first M principal components will be associated to non-vanishing eigenvalues. Therefore, only the first M principal components need to be derived: this is achieved by computing the M eigenvectors $\vec{w}_i'$ of the matrix $S' = \Delta^T \Delta \in \mathcal{M}_{\mathrm{M}\times\mathrm{M}}$, where $\Delta = (\vec{t}_i - \vec{t}_{\mathrm{ref}}) \in \mathcal{M}_{\mathrm{n}\times\mathrm{M}}$. These are related to the first M eigenvectors of the scatter matrix S, namely $\vec{w}_i = \Delta\, \vec{w}_i' \in \mathbb{R}^n$, with $i = 1, ..., M$.

The increase in computational speed is especially remarkable for large data sets, where $M \ll n$. In addition, all the relevant information is, in most cases, constrained by a very small number of independent components, $m < M$ (usually up to three for this kind of applications), allowing an even stronger dimensionality reduction.

6.2.3 Cosmological Applications

Although, in the framework of this work, the approach described so far is only applied to luminosity distance data, it has been derived in a fully general fashion: it allows in fact a straightforward way to combine different observables for a joint data analysis, by simply redefining the data vector and training set in order to include all the contributions from different experiments (e.g. distances to type-Ia supernovae, values of the cosmic shear correlation function and CMB multipoles).

The features $\vec{\tau}$, obtained by projecting the cosmological observables on the principal components, represent a very convenient cosmological parametrization. These parameters are, in fact, fully independent, their number is minimised with respect to the data quality and they provide the best discriminatory power between different cosmological models. Moreover, they can be used as a common parametrisation to compare and describe cosmological data sets without reference to a specific model, since only the properties of the observables, but not the physics behind them, are parametrised.

In any case, it is possible to univocally associate the features $\vec{\tau}$, which do not have any physical meaning, to the physical properties of any given model, by simply mapping the feature space with the projection of the investigated model (or models), thus establishing a precise relation between any point of the feature space and the cosmological parameters of a given model.

Two examples of features are shown in Fig. 6.3: the training set consists in the luminosity distance from type-Ia supernovae in the left panel, and in the CMB power spectrum in the right panel. Both examples are based on non-flat ΛCDM models where the Hubble constant, the equation of state of dark energy and the normalisation of the matter power spectrum are fixed to $h = 0.7$, $w = -1$, $\sigma_8 = 0.8$, respectively, and only the matter and dark-energy density parameters are allowed to vary in the range $0.1 < \Omega_{\rm m} < 0.5$ and $0.5 < \Omega_\Lambda < 0.9$, respectively. Each point in Fig. 6.3 represents a different cosmology and the separation between the points is maximised by definition; the reference cosmology, $\vec{t}_{\rm ref}$, sits in the origin of the

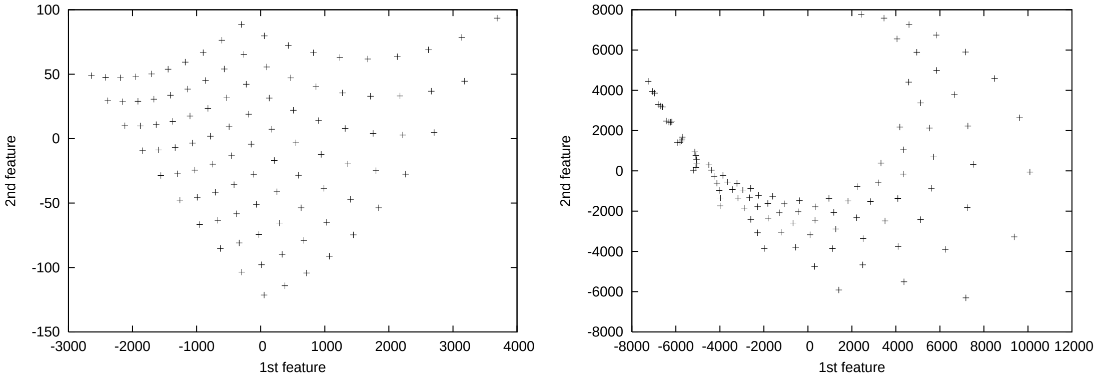

Figure 6.3: Features for a series of ΛCDM cosmologies with $h = 0.7$, $w = -1$, $\sigma_8 = 0.8$, $0.1 < \Omega_\mathrm{m} < 0.5$ and $0.5 < \Omega_\Lambda < 0.9$. The *left panel* refers to type-Ia supernova data (with the same sampling as in the SNLS, Astier et al. 2006), and the *right panel* to CMB data (computed on the multipoles of the WMAP-3 data release, Hinshaw et al. 2007).

feature space. It is worth noticing that, for the CMB data, at least three features would be necessary for a satisfactory description because of the rich complexity of the data set.

6.2.4 Reconstruction of the Expansion Rate

The reconstruction algorithm described in Chapter 4 requires the luminosity-distance data to be smoothed, and does it by expanding $D_\mathrm{L}(a)$ into a basis of orthonormal functions. The choice of the basis is arbitrary: for illustrative reasons, it was chosen to adopt the linearly independent set of functions $u_j(a) = a^{j/2-1}$, orthonormalised using the usual Gram-Schmidt procedure. However, the basis $\{p_j(a)\}$, which appears in the equations of Section 4.2, can be defined such as to minimise the number of necessary modes and to have them ordered according to their information content. A good choice fulfilling these criteria is represented by the principal components defined in Section 6.2.1, which can be optimised for a specific cosmology or for a set of cosmological models based on different physical assumptions.

The stability of the principal components with respect to the number of models used in the training set has been tested, and as an example, Fig. 6.4 shows the

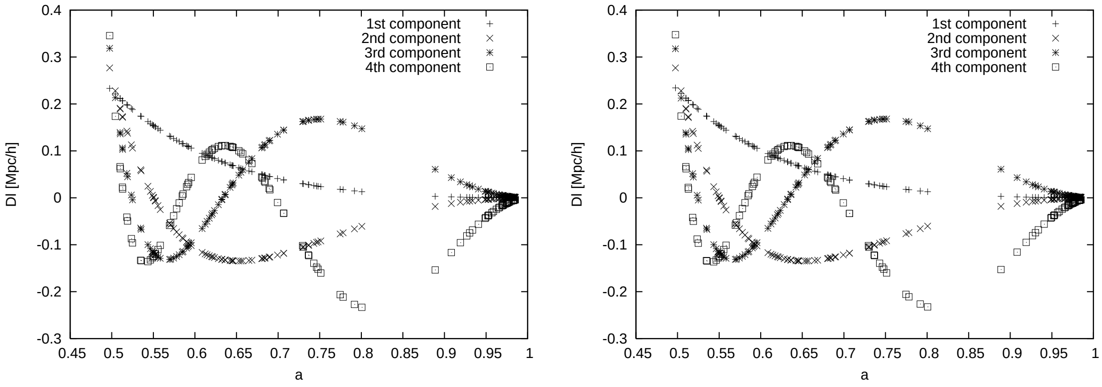

Figure 6.4: Example showing the stability of the principal components against the number of models used in the training set. The first 4 principal components, derived for a luminosity-distance data vector sampled at the redshifts covered by the SNLS, are shown. The training set was produced by sampling the parameter space 100 times in the *left panel* and 5 times in the *right panel*, respectively, in the two intervals $0.1 < \Omega_\mathrm{m} < 0.5$ and $0.5 < \Omega_\Lambda < 0.9$.

first four principal components derived for a luminosity-distance data vector with SNLS-like sampling. The training set is based on non-flat ΛCDM models with $h = 0.7$, $w = -1$ and the matter and dark-energy density parameters sampling the ranges $0.1 < \Omega_\mathrm{m} < 0.5$ and $0.5 < \Omega_\Lambda < 0.9$, respectively; as a reference cosmology, the average of the training set has been used. The $(\Omega_m, \Omega_\Lambda)$ space was regularly sampled by the training set $10,000$ times to produce the functions in the left panel and only 25 times in the right panel. Clearly, the principal components are very stable against the training set size and only depend on the range sampled by the cosmological parameters of the training set.

The information content of each principal component is quantified by the corresponding eigenvalue, which in this case are $\lambda_1 = 1$, $\lambda_2 = 2.0 \times 10^{-4}$, $\lambda_3 = 1.4 \times 10^{-7}$ and $\lambda_4 = 1.2 \times 10^{-10}$. Hence, all the information and discriminatory power is concentrated in the very first components, thus allowing a strong dimensionality reduction, from $n = 117$ (i.e. the number of supernovae in the data set) to 1 or 2 dimensions for this specific case. By increasing the number of the cosmological parameters or by sampling larger ranges in parameter space while constructing the training set, the power is distributed towards higher orders, but is still fairly concentrated in very few components.

The reconstruction of the expansion rate using the principal components applied to the formalism described in Section 4.2 requires less coefficients to be estimated, hence yields smaller error bars with respect to the use of the basis funtions described in Chapter 4. The increased accuracy is particularly evident at lower redshifts, where measurement errors are smaller, since the information in this case is localised on the points where the data are defined. The result of its application to a synthetic sample drawn from a ΛCDM model, with SNLS-like characteristics, and to the real SNLS data are shown in Fig. 6.5, along with the results obtained on the same samples in Chapter 4: the need to fit for one coefficient, rather than three, improves the reconstruction. The successful performance of the method on a simulated sample based on the toy model described in Section 4.5 and with SNAP-like characteristics is also shown.

6.2.5 Searching for Hidden Features in Cosmological Data Sets

As described in Section 6.2.1, the scatter matrix is usually computed with respect to the average training model, $\vec{t}_{\rm ref} = \sum_{i=1}^{m} \vec{t}_i/m$, so that the overall scatter among all cosmologies belonging to the training set is maximised. However, any other model can be chosen for this purpose: by fixing $\vec{t}_{\rm ref}$ to a specific reference cosmological model, the feature space origin is set to coincide with the adopted reference cosmology and the principal components maximise the discrimination power with respect to this model. This provides a straightforward way to verify whether the adopted reference model, for example the concordance ΛCDM model, is successful in describing the observations or if the data contain unforeseen features. If the latter is the case, the projected observations are not consistent with the feature space origin, i.e. the features $\vec{\tau}$ are not compatible with zero. The power of the method consists in the fact that the information from the whole data set is compressed in a very small number of quantities.

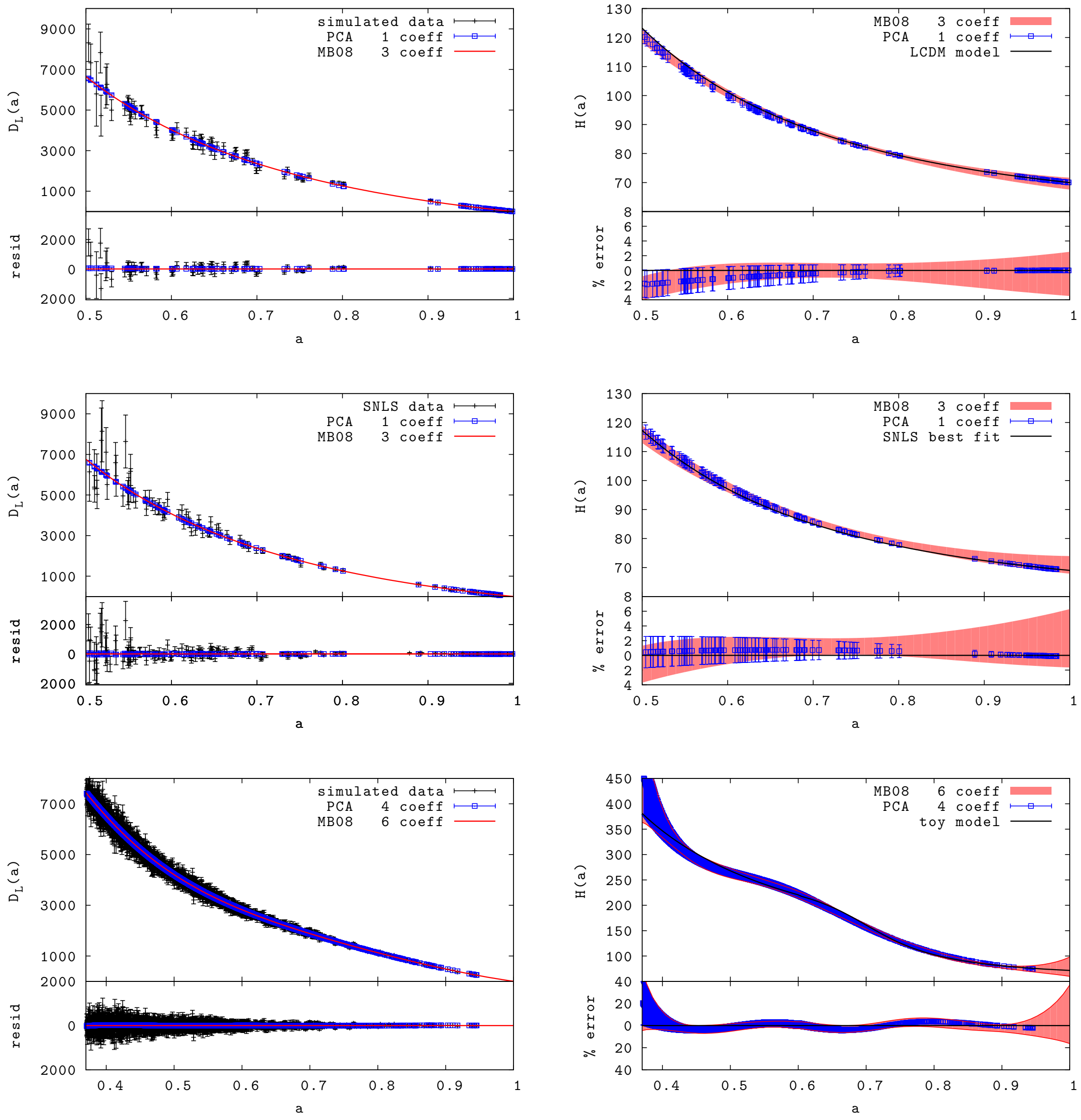

Figure 6.5: *Left panels:* synthetic and real samples of type-Ia supernovae (black points), with the fit obtained in Chapter 4 (red lines) and result achieved using PCA (blue squares). *Right panels:* The recovered expansion rate obtained in Chapter 4 (red shaded area), using the PCA approach (blue squares) and that of the model (or best-fit; black lines). The data sets, from top to bottom, are a synthetic, ΛCDM model sample with SNLS-like characteristics, the SNLS sample (Astier et al., 2006), and a synthetic, toy-model sample with SNAP-like characteristics, respectively.

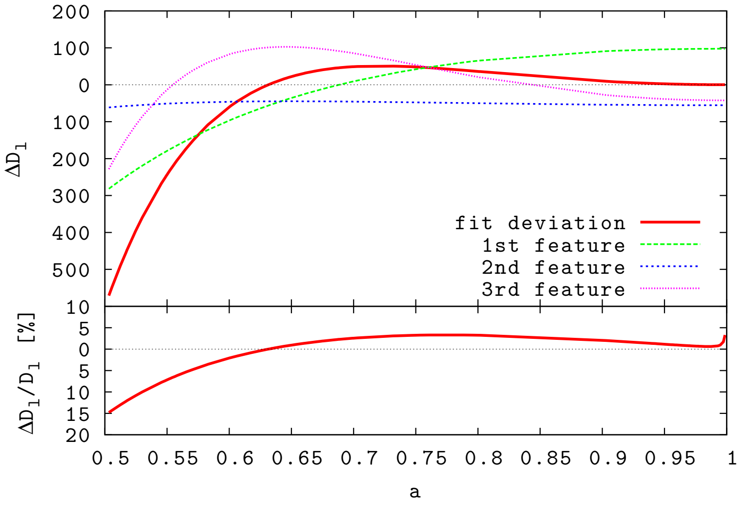

Figure 6.6: Detected missing features in the best-fit Friedmann ΛCDM model, from the analysis of a synthetic sample of type-Ia supernovae with luminosity distances drawn from the toy model with a sudden transition in the expansion rate, described in Section 4.5.

In order to illustrate the method, it is applied to an extreme case, namely the toy-model cosmology described in Section 4.5, characterised by a sudden transition in the expansion rate. The simulated data set, with SNLS-like characteristics, under an ordinary χ^2 analysis, fitting for Ω_m and Ω_Λ and assuming flatness, is compatible with a standard Friedmann ΛCDM cosmology (with $\chi^2 = 1.016$). The result is of course misleading, since the background cosmology has a completely different nature: a standard χ^2 approach is clearly not always capable of revealing unexpected features possibly hidden in the data.

The principal component approach is then used, adopting the best-fit ΛCDM model achieved from the standard χ^2 analysis as the reference cosmology in the definition of the scatter matrix, in order to verify the compatibility of the data with such a model and to search for possible hidden features. In this case, the three components required to successfully fit the data are not compatible with zero at a $3.2 - \sigma$ level, providing substantial evidence for the existence of unforeseen features and showing how the best-fit ΛCDM model might not be sufficient for a full description of such a data set. The detected features are plotted in Fig. 6.6, which shows the deviation of the data from the expected ΛCDM model.

Chapter 7

Conclusions

This thesis work proposes a method to constrain the expansion function of the universe without assuming any specific model for Friedmann-type expansion. If the universe is isotropic, homogeneous and simply connected, it is described by a Robertson-Walker metric. Cosmological measurements can generally only constrain one of two functions of time, the expansion rate and the growth of structures. It is shown here how the expansion function can be observationally constrained without reference to specific assumptions on the time evolution of the terms in Friedmann's equation and their parameterisation in terms of density parameters. The issue may become important in search of constraints for a dynamical dark energy component, whose behaviour is so far only very poorly known. Since it is unclear how its energy density contribution to the cosmic fluid may change in time, any guessed parameterisation may be erroneous, hence a parameter-free recovery of the cosmic expansion rate may turn out advantageous.

The method is first demonstrated using the luminosity-distance measurements obtained from type-Ia supernovae as a model. Since the luminosity distance is a cosmological observable depending on space-time geometry only, the dynamics of structure growth does not enter yet. The method proceeds in two essential steps. First, the integral relation between the expansion function and the luminosity distance is transformed into a Volterra integral equation of the second kind. Under the relevant conditions, its solutions are known to exist and to be uniquely described in terms of a convergent Neumann series. In other words, the method is guaranteed to return *the* unique expansion rate of the universe within the accuracy limits allowed by the data.

The drawback of the transformation to a Volterra integral equation is that the derivative of the luminosity distance with respect to the scale factor is needed to start the Neumann series. Derivatives of data are notoriously noisy and should be avoided. It is here proposed to expand the luminosity distance into an initially arbitrary orthonormal function set, fit its expansion coefficients to the data and then use the derivative of the series expansion instead of the derivative of the data. Suitable orthornormal function sets can be constructed by Gram-Schmidt orthonormalisation from any linearly independent function set. The only condition so far is that the number of coefficients required to fit the data should be minimal.

Once the orthonormal function set is specified, the Neumann series can be constructed beforehand for all its members. The measured coefficients of the series expansion directly translate to the solution for the expansion function. The convergence criterion for the Neumann series is determined by the data quality, as is the number of orthonormal modes in the series expansion of the data.

Applications to synthetic data samples of increasing complexity are very promising. In particular, it has been shown that an expansion function containing a sudden transition can be faithfully recovered by this method provided sufficient quality of the input data, whereas it may well go unnoticed if one of the most popular parameterisations for the dark-energy equation of state is assumed. The method has also been applied to the first-year SNLS data and to the extended ESSENCE sample, and the recovered expansion functions are shown.

Furthermore, the model-independent reconstruction of the expansion rate obtained from luminosity-distance data is employed to estimate the growth factor for linear structure formation, which represents the other fundamental function underlying all cosmological measurements, along with the expansion rate. In the standard scenario for structure formation, the linear growth factor is the solution of a second-order differential equation which only depends on the expansion rate and on the matter density parameter, $\Omega_{\rm m}$.

In this work, it has been shown that the empirical estimate of the expansion rate, along with external information on $\Omega_{\rm m}$, is sufficient to achieve an accurate reconstruction of the linear growth factor in the redshift range where the expansion rate is constrained by the luminosity-distance data, even though the initial conditions imposed while solving the differential equation require to extrapolate the expansion function to much earlier times.

The redshift interval over which supernova data are currently available is roughly the same as the one relevant for cosmic shear. It is thus reasonable to apply the empirical estimate of the expansion function, and consequently of the linear growth factor, to the analysis of cosmic shear data on linear scales, in order to constrain the matter density parameter and the power spectrum normalisation, σ_8. Analogously to what happens with the usual, ΛCDM parameterisation, also in this case the result of such an analysis suffers from a degeneracy in the $(\Omega_{\rm m}, \sigma_8)$ plane. Due to the different way $\Omega_{\rm m}$ enters in the two different parameterisations, however, the two degeneracies identify different tracks in the parameter space. This suggests to combine them, in the assumption that both models, i.e. the ΛCDM and the empirical parameterisation, are a fair representation of the underlying universe.

This procedure, although restricting the range of possible models to flat ΛCDM cosmologies, makes use of the information provided by the model-independent approach to break the aforementioned degeneracy and achieve tight constraints on both the matter density parameter and the power spectrum normalisation. Application to synthetic data sets with technical requirements within the reach of next-generation cosmic shear experiments are remarkably promising, especially when a prescription for the non-linear evolution is also included in the parameterisation of the matter power spectrum.

A generalisation of the model-independent reconstruction technique, in order to include not only luminosity-distance but also angular-diameter distance data has been developed and applied to the results of future-generation galaxy surveys targeting baryon acoustic oscillations. Although an accurate estimate of the expansion rate can be achieved from such data, the precision is much worse than that obtained from the application of the same method to supernova data; furthermore, spectroscopic surveys targeting baryon acoustic oscillations are also able to directly measure the expansion rate as a function of redshift, with precision higher or comparable to that achieved applying the model-independent reconstruction technique to the distance data. Hence, the application of the method to baryon acoustic oscillation data did not prove to be a particularly interesting case.

In the formalism developed to reconstruct the expansion rate, the specification of the orthonormal function set into which the data set is decomposed is arbitrary. The question was still open, though, whether an optimal set of functions for this method exists: the issue has been investigated by means of a principal component analysis, allowing to construct a basis whose very first few components are enough to describe the data sets. Thanks to this dimensionality reduction, a more precise reconstruction of the expansion rate is possible. The principal component approach is also powerful in detecting unexpected features in the data, such as a sudden transition in the expansion rate, which might be overlooked by a standard analysis assuming an erroneous parameterisation for the dark-energy component.

Current and future observational projects aim at collecting extremely large data sets in order to determine the very nature of the dark energy and of the accelerated expansion of the universe. In sight of these challenges, it is advisable to pursue a model-independent approach to interpret the astronomical measurements and the cosmological functions underlying them. With the choice of a suitable function set, the reconstruction technique developed in this work stands out as a novel and advantageous method to analyse cosmological data sets of various nature, introducing as little theoretical prejudice as possible. It can, in principle, be generalised and applied to other measurements carrying information about the expansion rate and the linear growth factor, such as the anisotropies in the cosmic microwave background or the evolution of the galaxy cluster population. The model-independent reconstruction can also be combined to other approaches and contribute, with additional information, to the estimate of cosmological parameters, as shown in the application to cosmic shear.

Bibliography

Akaike, H. 1973, Second International Symposium on Information Theory, edited by B. N. Petrov & F. Csaki, Budapest: Akademiai Kiado, 267

Akaike, H. 1974, IEE Transactions on Automatic Control, 19, 716

Alam, U., Sahni, V., & Starobinsky, A. A. 2008, ArXiv e-prints, 0812.2846

Albrecht, A., Bernstein, G., Cahn, R., et al. 2006, ArXiv Astrophysics e-prints, arXiv:astro-ph/0609591

Aldering, G. & the SNAP collaboration. 2004, ArXiv Astrophysics e-prints, astro-ph/0405232

Allen, S. W., Schmidt, R. W., Ebeling, H., Fabian, A. C., & van Speybroeck, L. 2004, MNRAS, 353, 457

Allen, S. W., Schmidt, R. W., Fabian, A. C., & Ebeling, H. 2003, MNRAS, 342, 287

Alpher, R. A. & Herman, R. C. 1949, Phys. Rev., 75, 1089

Arfken, G. B. & Weber, H. J. 2005, “Mathematical Methods for Physicists” 6th ed. (Elsevier Academic Press)

Astier, P., Guy, J., Regnault, N., et al. 2006, A&A, 447, 31

Bacon, D. J., Refregier, A. R., & Ellis, R. S. 2000, MNRAS, 318, 625

Bartelmann, M. 2009, in preparation

Bartelmann, M. & Schneider, P. 2001, Phys. Rep., 340, 291

Bassett, B. A., Corasaniti, P. S., & Kunz, M. 2004, ApJL, 617, L1

Blake, C. & Glazebrook, K. 2003, ApJ, 594, 665

Blake, C. A., Abdalla, F. B., Bridle, S. L., & Rawlings, S. 2004, New Astronomy Review, 48, 1063

Boerner, G. & Ehlers, J. 1988, A&A, 204, 1

Burles, S., Nollett, K. M., & Turner, M. S. 1999, ArXiv Astrophysics e-prints, astro-ph/9903300

Burnham, K. P. & Anderson, D. R. 2004, Sociological Methods & Research, Vol. 33, No. 2, 261

Carroll, S. M. 1997, ArXiv General Relativity and Quantum Cosmology e-prints, arXiv:gr-qc/9712019

Carroll, S. M., Press, W. H., & Turner, E. L. 1992, ARA&A, 30, 499

Chevallier, M. & Polarski, D. 2001, International Journal of Modern Physics D, 10, 213

Cimatti, A., Robberto, M., Baugh, C., et al. 2008, Experimental Astronomy, 37

Cole, S., Percival, W. J., Peacock, J. A., et al. 2005, MNRAS, 362, 505

Coles, P. & Lucchin, F. 2002, "Cosmology: The Origin and Evolution of Cosmic Structure", Second Edition (John Wiley and Sons)

Colless, M., Dalton, G., Maddox, S., et al. 2001, MNRAS, 328, 1039

Conley, A., Carlberg, R. G., Guy, J., et al. 2007, ApJL, 664, L13

Contaldi, C. R., Hoekstra, H., & Lewis, A. 2003, Phys. Rev. Lett., 90, 221303

Crittenden, R. G. & Pogosian, L. 2005, ArXiv Astrophysics e-prints astro-ph/0510293

Davis, T. M., Mörtsell, E., Sollerman, J., et al. 2007, ApJ, 666, 716

Dodelson, S. 2003, “Modern Cosmology” (Academic Press)

Doré, O., Martig, M., Mellier, Y., et al. 2007, ArXiv e-prints, 0712.1599

Durrer, R. & Maartens, R. 2008, ArXiv e-prints, 0811.4132

Efstathiou, G. 2003, MNRAS, 343, L95

Eisenstein, D. J., Seo, H.-J., & White, M. 2007, ApJ, 664, 660

Eisenstein, D. J., Zehavi, I., Hogg, D. W., et al. 2005, ApJ, 633, 560

Etherington, I. M. H. 1933, Philosophical Magazine, 15, 761

Freedman, W. L., Madore, B. F., Gibson, B. K., et al. 2001, ApJ, 553, 47

Fu, L., Semboloni, E., Hoekstra, H., et al. 2008, A&A, 479, 9

Goobar, A. & Perlmutter, S. 1995, ApJ, 450, 14

Hamilton, A. J. S., Kumar, P., Lu, E., & Matthews, A. 1991, ApJL, 374, L1

Harrison, E. R. 1970, Phys. Rev. D, 1, 2726

Hillebrandt, W. & Niemeyer, J. C. 2000, ARA&A, 38, 191

Hinshaw, G., Nolta, M. R., Bennett, C. L., et al. 2007, ApJS, 170, 288

Hoekstra, H., Mellier, Y., van Waerbeke, L., et al. 2006, ApJ, 647, 116

Huterer, D. & Starkman, G. 2003, Phys. Rev. Lett., 90, 031301

Huterer, D. & Turner, M. S. 1999, Phys. Rev. D, 60, 081301

Huterer, D. & Turner, M. S. 2000, Phys. Rev. D, 62, 063503

Ivezic, Z., Tyson, J. A., Allsman, R., et al. 2008, ArXiv e-prints, 0805.2366

Joachimi, B., Schneider, P., & Eifler, T. 2008, A&A, 477, 43

Kasen, D. & Woosley, S. E. 2007, ApJ, 656, 661

Kellermann, K. I. 1993, Nature, 361, 134

Kneller, J. P. & Steigman, G. 2004, New Journal of Physics, 6, 117

Komatsu, E., Dunkley, J., Nolta, M. R., et al. 2009, ApJS, 180, 330

Kowalski, M., Rubin, D., Aldering, G., et al. 2008, ApJ, 686, 749

Lahav, O., Bridle, S. L., Percival, W. J., et al. 2002, MNRAS, 333, 961

Leibundgut, B. 2001, ARA&A, 39, 67

Linder, E. V. 2003, Phys. Rev. Lett., 90, 091301

Maor, I., Brustein, R., & Steinhardt, P. J. 2001, Phys. Rev. Lett., 86, 6

Mather, J. C., Cheng, E. S., Cottingham, D. A., et al. 1994, ApJ, 420, 439

Maturi, M. & Mignone, C. 2009, ArXiv e-prints, 0905.1590

Mignone, C. & Bartelmann, M. 2008, A&A, 481, 295

Munshi, D., Valageas, P., Van Waerbeke, L., & Heavens, A. 2008, Phys. Rep., 462, 67

Peacock, J. A. & Dodds, S. J. 1996, MNRAS, 280, L19

Peebles, P. J. E. 1982, ApJL, 263, L1

Peebles, P. J. E. & Yu, J. T. 1970, ApJ, 162, 815

Penzias, A. A. & Wilson, R. W. 1965, ApJ, 142, 419

Percival, W. J., Cole, S., Eisenstein, D. J., et al. 2007a, MNRAS, 381, 1053

Percival, W. J., Nichol, R. C., Eisenstein, D. J., et al. 2007b, ApJ, 657, 645

Perlmutter, S., Aldering, G., Goldhaber, G., et al. 1999, ApJ, 517, 565

Perlmutter, S. & Schmidt, B. P. 2003, in Lecture Notes in Physics, Berlin Springer Verlag, Vol. 598, Supernovae and Gamma-Ray Bursters, ed. K. Weiler, 195–217

Phillips, M. M. 1993, ApJL, 413, L105

Phillips, M. M., Lira, P., Suntzeff, N. B., et al. 1999, AJ, 118, 1766

Refregier, A. 2008, Experimental Astronomy, 26

Riess, A. G., Filippenko, A. V., Challis, P., et al. 1998, AJ, 116, 1009

Riess, A. G., Strolger, L. G., Casertano, S., et al. 2007, ApJ, 659, 98

Riess, A. G., Strolger, L.-G., Tonry, J., et al. 2004, ApJ, 607, 665

Sachs, R. K. & Wolfe, A. M. 1967, ApJ, 147, 73

Schilizzi, R. T., Dewdney, P. E. F., & Lazio, T. J. W. 2008, in Society of Photo-Optical Instrumentation Engineers (SPIE) Conference Series, Vol. 7012, Society of Photo-Optical Instrumentation Engineers (SPIE) Conference Series

Semboloni, E., Mellier, Y., van Waerbeke, L., et al. 2006, A&A, 452, 51

Seo, H.-J. & Eisenstein, D. J. 2003, ApJ, 598, 720

Seo, H.-J. & Eisenstein, D. J. 2007, ApJ, 665, 14

Shafieloo, A. 2007, MNRAS, 380, 1573

Shafieloo, A., Alam, U., Sahni, V., & Starobinsky, A. A. 2006, MNRAS, 366, 1081

Silk, J. 1968, ApJ, 151, 459

Simon, P., Hetterscheidt, M., Schirmer, M., et al. 2007, A&A, 461, 861

Simpson, F. & Bridle, S. 2006, Phys. Rev. D, 73, 083001

Smith, R. E., Peacock, J. A., Jenkins, A., et al. 2003, MNRAS, 341, 1311

Smoot, G. F., Bennett, C. L., Kogut, A., et al. 1992, ApJL, 396, L1

Spergel, D. N., Bean, R., Doré, O., et al. 2007, ApJS, 170, 377

Spergel, D. N., Verde, L., Peiris, H. V., et al. 2003, ApJS, 148, 175

Springel, V., White, S. D. M., Jenkins, A., et al. 2005, Nature, 435, 629

Starobinsky, A. A. 1998, Soviet Journal of Experimental and Theoretical Physics Letters, 68, 757

Steigman, G. 2007, Annual Review of Nuclear and Particle Science, 57, 463

Sunyaev, R. A. & Zeldovich, Y. B. 1970, Ap&SS, 7, 3

Sunyaev, R. A. & Zeldovich, Y. B. 1972, Comments on Astrophysics and Space Physics, 4, 173

Tauber, J. A. 2004, Advances in Space Research, 34, 491

Tegmark, M. 2002, Phys. Rev. D, 66, 103507

Tegmark, M., Taylor, A. N., & Heavens, A. F. 1997, ApJ, 480, 22

Valenziano, L., Sandri, M., Morgante, G., et al. 2007, New Astronomy Review, 51, 287

Van Waerbeke, L. & Mellier, Y. 2003, ArXiv Astrophysics e-prints, astro-ph/0305089

Van Waerbeke, L., Mellier, Y., Erben, T., et al. 2000, A&A, 358, 30

Wang, Y. & Tegmark, M. 2005, Phys. Rev. D, 71, 103513

Weinberg, S. 2008, “Cosmology” (Oxford University Press)

Wood-Vasey, W. M., Miknaitis, G., Stubbs, C. W., et al. 2007, ApJ, 666, 694

York, D. G., Adelman, J., Anderson, Jr., J. E., et al. 2000, AJ, 120, 1579

Zeldovich, Y. B. 1972, MNRAS, 160, 1P

Acknowledgements

Here I am, finally at the end of this thesis. It's something a.m., very early, or very late, depends on the point of view... I had absolutely no doubts that I would have ended up writing the last bits of the thesis at this time. It's a shame I'm so tired, though, this part should be one of the funniest...

If I reached this point, even at this time, I mostly owe it to Matthias... You've been an amazing supervisor, actually an amazing person. Thanks for every single time you've answered to all my questions and for all the times you've given me great ideas and suggestions. Thanks for the constant support and respect, for trying to take the best out of me and make me believe in myself (I will, one day...). Thanks for the enthusiasm you put every day in cosmology and science in general, I wish I had a tiny little fraction of it, and also, thanks for not having pressured me when I was (or still am?) confused and needed to process things at my own, very slow speed. Thanks a lot, really!

Another big thanks goes to Lauro, for not having forgotten about me, but instead for having visited Heidelberg often and almost regularly, and for the hospitality at the Department in Bologna whenever I stopped by. Thanks also for agreeing to read and referee my thesis and to take part to the exam, but mostly thanks for always trying to motivate me and (again) for pushing me to believe in myself.

I wish to thank also Prof. Hans-Walter Rix and Prof. Eva Grebel, who agreed to take part to my exam.

Let's see now, all the people I collaborated with: Matteo, thanks for all the times you solved a lot of problems I had, especially with codes and statistics, for the PCA idea which improves my error bars! and for the glorious (although it never became reality) idea of the ignorance club... I'm still not sure if I want to thank

you for putting me in charge of the winter school though! Massimo, although you went back to Italy shortly after I started, thanks for the constant trust in me and also for pushing me when the paper was still not finished.

I also wish to thank Licia Verde for hospitality in Barcelona, and for helping me sorting out the BAO stuff, and Sarah Bridle for having me over at UCL. Thank you both for the enthusiasm!

Collaborators or not, thanks to all the ITA boys! I keep saying I can't stand you, but I'm sure ITA wouldn't be the same without all the mean guys... First, thanks to the poor three guys who had the misfortune of sharing the office with me: Cosimo, Christian and Stefan, thanks for standing my oscillating moods and my noisy typing! and then to the other offices... JC, Julian, Mischa, Peter, Gregor, Martin, Peter-B, Madeleine, and the new arrivals Katja, Luigi, Ana, Björn, Lavinia, Reneè, Gero, thanks for all the coffee breaks and the laughs, the movies, the power of procrastination and well, whatever. A special thanks to Ciccio for always being there with an answer to any question, to Emanuel, my computer guru! to Carlo for the energy and the fun, and to Massimo for being my shoulder in these last months, for the survival tools and for being mean after all! I also wish to thank Ana L. for all the long chats and the funky style, and Anna Z. for all the help sorting out German bureaucracy. Also thanks to Valeria, my official conference roommate, for the enthusiasm about cosmology, and to all the cool people I've met at schools and meetings who make the astro-world a teeny bit funnier.

Surviving in Heidelberg, how could have I done it without my girls? I don't really know how to thank you for being there for me all the time... except now, actually!! Giulia, thanks for all the mails, the chats, the advice and the crazy gags during these years with Tom's soundtrack (damn, it's really closing time!). Giovi, thanks for coming here to take care of me like a guardian angel, and for all the hours (days?) spent chilling out on the couch. Isabel, thanks for the energy and the passion, for all the delirious conversations in the night time. Viviana, thanks for having always listened to my craziness and for being so calm and peaceful (at least with us!)

Ale e Matteo, thanks for all the crazy nights, the rings of fire and the warmer erpel. Brian, Giovanni, Olga, Baybars, Vivi, Sara, and all the insane astrophysicists in Heidelberg, thanks a lot! Thanks to all the IMPRS people of all generations for the fun atmosphere, and by the way thanks to Christian Fendt for making such a thing possible and for all the effort! Another special thanks to my new roommate Gisella, who practically baby-sit me in these last few weeks of writing, and to Marcello, for all the cool, weird projects he pushed me into and for listening to all my paranoid thoughts.

Thanks to the Italians of Heidelberg, Stefano, Lorenza, Anna and all the others. Thanks to Dan, Erwan and the bio people, thanks to Vitor and all the photo-exhibit gang, by the way thanks to the AHA and to all those who believed in it, too bad dreams do not always come true, and since I'm thanking places, thanks also to Karlstor, Villa, Untere, Orange and all the hangouts of these four years...

My Weltladen friends, I thank you all! especially Simon, Susanne, Matthias, Sarah, Andi, Ina, Dagi, if I can speak some German now it's only thanks to you. Working in the store was one of my happiest places in the past few years, and I'm so sorry I'm going to leave, I wish you all the best.

A big, long-distance thanks to all my "astronze"... Lauretta, thanks for always being there to listen to my madness and to tell me about yours, and for sharing the Heidelberg experience with us for a while. Nico, thanks for being so lovely and for having visited so often. Giorgia, Anna, Sara (e Matteo!) thanks for the long emails and for your share of nuts!

And even if they don't really deserve it (!) I thank also my sisters back from home... Enrica, Faffola, Eleonora, Ilaria, Porzia, thanks for making me have a great time whenever I came to see you or back home, thanks for still being able to understand me and for still be so crystal clear to me, even though time goes by (and we're getting old! but at least now you know how to use technology to communicate!) and also thanks to Eugenio for still being a believer.

Last but clearly not least, mum and dad, thanks for everything! for being there, for coming, for listening, for waiting, for standing my terrible moods, especially these past few weeks, I'm so sorry I know I was awful on the phone! let's blame the thesis... thanks for believing in me and supporting me no matter what, even though I don't really know where I'm going to, thanks for always making it so smooth. And now, let's see what happens...